LASER METALLIZATION AND DOPING FOR SILICON CARBIDE DIODE FABRICATION AND ENDOTAXY

by

ZHAOXU TIAN
B.S. Northwestern Polytechnical University, 1996
M.S. University of Science and Technology Beijing, 2003

A dissertation submitted in partial fulfillment of the requirements
for the degree of Doctor of Philosophy
in the Department of Mechanical, Materials and Aerospace Engineering
in the College of Engineering and Computer Science
at the University of Central Florida
Orlando, Florida

Spring Term
2006

Major Professor: Aravinda Kar

© 2006 Zhaoxu Tian

ABSTRACT

Silicon carbide is a promising semiconductor material for high voltage, high frequency and high temperature devices due to its wide bandgap, high breakdown electric field strength, highly saturated drift velocity of electrons and outstanding thermal conductivity. With the aim of overcoming some challenges in metallization and doping during the fabrication of silicon carbide devices, a novel laser-based process is provided to direct metallize the surface of silicon carbide without metal deposition and dope in silicon carbide without high temperature annealing, as an alternative to the conventional ion implantation, and find applications of this laser direct write metallization and doping technique on the fabrication of diodes, endotaxial layer and embedded optical structures on silicon carbide wafers.

Mathematical models have been presented for the temperature distributions in the wafer during laser irradiation to optimize laser process parameters and understand the doping and metallization mechanisms in laser irradiation process.

Laser irradiation of silicon carbide in a dopant-containing ambient allows to simultaneously heating the silicon carbide surface without melting and incorporating dopant atoms into the silicon carbide lattice. The process that dopant atoms diffuse into the bulk silicon carbide by laser-induced solid phase diffusion (LISPD) can be explained by considering the laser enhanced substitutional and interstitial diffusion mechanisms. Nitrogen and Trimethyaluminum (TMA) are used as dopants to produce n-type and p-

type doped silicon carbide, respectively. Two laser doping methods, i.e., internal heating doping and surface heating doping are presented in this dissertation. Deep (800 nm doped junction for internal heating doping) and shallow (200 nm and 450 nm doped junction for surface heating doping) can be fabricated by different doping methods. Two distinct diffusion regions, near-surface and far-surface regions, were identified in the dopant concentration profiles, indicating different diffusion mechanisms in these two regions. The effective diffusion coefficients of nitrogen and aluminum were determined for both regions by fitting the diffusion equation to the measured concentration profiles. The calculated diffusivities are at least 6 orders of magnitude higher than the typical values for nitrogen and aluminum, which indicate that laser doping process enhances the diffusion of dopants in silicon carbide significantly. No amorphization was observed in laser-doped samples eliminating the need for high temperature annealing.

Laser direct metallization can be realized on the surface of silicon carbide by generating metal-like conductive phases due to the decomposition of silicon carbide. The ohmic property of the laser direct metallized electrodes can be dramatically improved by fabricating such electrodes on laser heavily doped SiC substrate.

This laser-induced solid phase diffusion technique has been utilized to fabricate endolayers in n-type 6H-SiC substrates by carbon incorporation. X-ray energy dispersive spectroscopic analysis shows that the thickness of endolayer is about 100 nm. High resolution transmission electron microscopic images indicate that the laser endotaxy process maintains the crystalline integrity of the substrate without any amorphization.

Rutherford backscattering studies also show no amorphization and evident lattice disorder occur during this laser solid phase diffusion process. The resistivity of the endolayer formed in a 1.55 Ω·cm silicon carbide wafer segment was found to be 1.1×10^5 Ω ·cm which is sufficient for device fabrication and isolation. Annealing at 1000°C for 10 min to remove hydrogen resulted in a resistivity of 9.4×10^4 Ω ·cm.

Prototype silicon carbide PIN diodes have been fabricated by doping the endolayer and parent silicon carbide epilayer with aluminum using this laser-induced solid phase diffusion technique to create p-regions on the top surfaces of the substrates. Laser direct metallized contacts were also fabricated on selected PIN diodes to show the effectiveness of these contacts. The results show that the PIN diode fabricated on a 30 nm thick endolayer can block 18 V, and the breakdown voltages and the forward voltages drop at 100 A/cm^2 of the diodes fabricated on 4H-SiC with homoepilayer are 420 ~ 500 V and 12.5 ~ 20 V, respectively.

The laser direct metallization and doping technique can also be used to synthesize embedded optical structures, which can increase 40% reflectivity compared to the parent wafer, showing potential for the creation of optical, electro-optical, opto-electrical, sensor devices and other integrated structures that are stable in high temperature, high-pressure, corrosive environments and deep space applications.

To my parents, Songlin Tian and Shuilian Yin, and wife Qianqian Hu.

Thank you

ACKNOWLEDGMENTS

I would like to thank for those who contributed and supported throughout my graduate studies at the College of Optics & Photonics/CREOL and Department of Mechanical, Materials and Aerospace Engineering. First of all I would like to express my heartfelt gratitude to my advisor, Dr. Aravinda Kar, for his guidance, advice and support. His advisement, discussion, encouragement and suggestions have given me the confidence and success in my daily practice and made this work possible. Thanks to him, I learned not only how to manage difficulties and accomplish challenging research projects but also how to think independently and creatively. I am also grateful to Dr. N. Quick, president of AppliCote Associates, for his support and encouragement. Dr. Quick's experience had contributed generously to the success of my research work.

I would like to thank my committee members: Dr. G. Braunstein, Dr. D. Malocha, Dr. W. Schoenfeld, Dr. C. Suryanaryana and Dr. R. Vaidyanathan for their time reviewing my dissertation and for their valuable comments and discussions. Thanks are also due to the technical staff at MCF for their help in the materials characterization work. I would like to express my appreciations to all colleagues in the LAMP group. Finally I would like to thank my family and friends for their love, understanding and support through the years.

TABLE OF CONTENTS

LIST OF FIGURES xii

LIST OF TABLES xix

LIST OF ACRONYMS/ABBREVIATIONS xxi

LIST OF PUBLICATIONS xxvi

CHAPTER 1: INTRODUCTION AND LITERATURE REVIEW 1

1.1 Motivation 1

1.2 Literature Reviews 3

1.2.1 Silicon Carbide 3

1.2.2 Current Technology Barriers in Silicon Carbide Device Fabrication 5

1.2.3 Fabrication of Silicon Carbide PIN Diodes 14

1.2.4 Epitaxial Growth of Silicon Carbide 16

1.2.5 Laser Interaction with Semiconductors 19

1.2.6 Temperature Distribution during Laser Irradiation Process 21

1.3 Objectives 22

CHAPTER 2: TEMPERATURE DISTRIBUTION ANALYSIS DURING LASER METALLIZATION AND DOPING PROCESS OF SILICON CARBIDE 24

2.1 Introduction 24

2.2 Mathematical model and analysis of laser internal heating 26

2.2.1 Mathematical model and solution 26

2.2.2 Results and Discussion 29

2.3 Mathematical model and analysis of surface heating 46

2.3.1 Mathematical Model and Solution 46

2.3.2 Results and discussion 47

CHAPTER 3: EXPERIMENTAL METHODS AND CHARACTERIZATION TECHNIQUES 53

3.1 Samples Preparation 53

3.2 Laser Irradiation Experimental Set-up 54

3.3 Materials Characterization 58

3.3.1 Secondary Ion Mass Spectroscopy (SIMS) 58

3.3.2 Focused Ion Beam Instrument (FIB) 58

3.3.3 Transmission Electron Microscopy (TEM) 59

3.3.4 X-ray Energy Dispersive Spectrometry (XEDS) 59

3.3.5 Rutherford Backscattering Spectroscopy (RBS) 59

3.4 Electrical Characterization 60

3.4.1 Current-Voltage (I-V) Characteristics of the Laser Direct Metallized Electrodes 60

3.4.2 Resistivity of the Endolayer 60

3.4.3 Current-Voltage (I-V) Characteristics of the PIN Diodes 61

3.5 Optical Characterization 61

3.5.1 Laser Beam Characteristics 61

3.5.2 Reflectivity and Transmitivity of Optical Structure at Particular Wavelength 61

CHAPTER 4: LASER DOPING AND DIRECT METALLIZATION OF SILICON CARBIDE 62

4.1 Introduction 62

4.2 Laser Doping Process of Silicon Carbide 63

4.3 Doping profiles 71

4.3.1 Doping Profiles Obtained by Laser Internal Heating 71

4.3.2 Doping profiles obtained by Laser Surface Heating 76

4.4 Mechanisms of Laser Doping Process 78

4.5 Effective Diffusivity Analysis 80

4.6 Laser Metallization Process of Silicon Carbide 93

4.7 Realization of Laser Direct Metallization on the Surface of Silicon Carbide .. 96

CHAPTER 5: FABRICATION OF ENDOLAYER AND PIN DIODES OF SILICON CARBIDE 102

5.1 Introduction 102

5.2 Fabrication of Endolayers in N-Type 6H-SiC Substrates 103

5.2.1 Experimental Procedures 103

5.2.2 Carbon Source 104

5.2.3 Hydrogen removal from the endolayer 107

5.2.4 Determination of the Thickness and Crystalline Order of the Endolayer 109

5.2.5 Determination of the Resistivity of the Endolayer 119

5.3 Fabrication of PIN Diodes on Substrates with an Endolayer 123

5.4 Fabrication of PIN Diodes on Substrates with Epilayer 129

CHAPTER 6: LASER SYNTHESIS OF OPTICAL STRUCTURE IN SILICON CARBIDE 139

6.1 Introduction 139

6.2 Laser Synthesis of Embedded Optical Phases 139

6.3 Optical Property Modification 144

CHAPTER 7: SUMMARY 150

7.1 Conclusions 150

7.2 Future Work 153

REFERENCES 155

LIST OF FIGURES

Figure 1.1 A schematic of doping by ion implantation [Singh (2001)]. 9

Figure 1.2 Illustration of GILD process [Jones et al. (1998)]. 13

Figure 1.3 Cross-sectional structure of 4H-SiC UHV diode with shallow mesa JTE [Sugawara et al. (2001)]. 15

Figure 2.1 Different heating mechanisms for laser irradiation: (a) Volumetric heating during Nd:YAG laser irradiation and (b) Surface heating during excimer laser irradiation. 25

Figure 2.2 Transient temperature distribution along the depth of the substrate (d = 270 μm) at t = 48 ns during Nd:YAG laser irradiation. The laser irradiance = 80.6 MW/cm^2, beam radius = 150 μm, pulse length = 72 ns and pulse repetition rate = 3 kHz. 31

Figure 2.3 Temperature distribution of 6H-SiC wafer (d = 430 μm) irradiated at different laser intensity (I=50, 100 and 150 MW/cm^2) and same pulse repetition rate (f=3 kHz) and accordingly pulse on time (τ_{on}=72 ns). 33

Figure 2.4 Temperature distribution of 6H-SiC wafer (d = 430 μm) irradiated at different pulse repetition rate (f=3, 10, 20 and 35 kHz) and pulse on time (τ_{on} =72, 126, 200 and 290 ns) and same laser intensity (I=50 MW/cm^2). 34

Figure 2.5 Variation of peak temperature with laser intensity at different pulse repetition rate (f=3, 10, 20, 35 kHz) on the 6H-SiC substrate (d = 430 μm). 35

Figure 2.6 Variation of peak temperature for 4H- and 6H-SiC at the combination of laser intensity and pulse repetition rate. The curves indicating the decomposition temperature of SiC, 3100 K. 36

Figure 2.7 Temperature distribution of one single pulse with same peak temperature (3100 K) irradiated at different pulse repetition rate (f=3, 17.5 and 35 kHz) and laser intensity (I=88.7, 56.4 and 44.2 MW/cm^2) on 6H-SiC substrate (d = 430 μm). 39

Figure 2.8 Variation of temperature at the end of one single pulse with pulse repetition rate for 4H- and 6H- SiC wafers (d = 430 μm).. 40

Figure 2.9 Temperature profiles of three pulses of 6H-SiC wafer (d = 430 μm) irradiated at pulse repetition rate of 3 kHz and laser intensity of 88.7 MW/cm^2...................... 41

Figure 2.10 Temperature profiles of three pulses of 6H-SiC wafer (d = 430 μm) irradiated at pulse repetition rate of 17.5 kHz and laser intensity of 56.4 MW/cm^2................. 42

Figure 2.11 Temperature profiles of three pulses of 6H-SiC wafer (d = 430 μm) irradiated at pulse repetition rate of 35 kHz and laser intensity of 44.2 MW/cm^2.................... 43

Figure 2.12 Time evolution of temperature along the thickness of the 6H-SiC wafer (d = 430 μm) near the bottom surface region. (Laser intensity: 91 MW/cm^2; Pulse repetition rate: 3 kHz). 44

Figure 2.13 Temperature profiles of 6H-SiC (d = 430 μm) at particular position during the laser irradiation. (Laser intensity: 91 MW/cm^2; Pulse repetition rate: 3 kHz). .. 45

Figure 2.14 Temperature profiles of 6H-SiC irradiated by different excimer laser sources (λ=351, 248 and 193 nm) and same laser intensity (60 MW/cm^2)........................... 50

Figure 2.15 Temperature profiles of 4H-SiC irradiated by different excimer laser sources (λ=351, 248 and 193 nm) and same laser intensity (60 MW/cm^2). 51

Figure 2.16 Time evolution of temperature along the thickness of the 6H-SiC wafer near the top surface region. (Laser intensity: 73 MW/cm^2; wavelength: 248 nm). 52

Figure 3.1 Intensity profile of the incident Nd:YAG laser beam. (a) Front view. (b) Top view. 55

Figure 3.2 Experimental set-up for laser doping, direct metallization and growing endolayer system. 57

Figure 4.1 Temperature distribution of 6H-SiC during n-type doping using the parameters of method A listed in Table 4.1.(a) Bottom surface temperature distribution with the time; (b) Transient temperature distribution along the thickness of the wafer from the bottom surface at the peak temperature (t=48ns). 66

Figure 4.2 Temperature distribution of 6H-SiC during p-type doping using the parameters of method A listed in Table 4.1.(a) Bottom surface temperature distribution with the time; (b) Transient temperature distribution along the thickness of the wafer from the bottom surface at the peak temperature (t=48ns). 68

Figure 4.3 Temperature distribution of 4H-SiC during p-type doping using the parameters of method C listed in Table 4.1.(a) Top surface temperature distribution with the time; (b) Transient temperature distribution along the thickness of the wafer from the top surface at the peak temperature (t=25ns). 70

Figure 4.4 Nitrogen dopant profiles obtained with a Nd:YAG laser. C_a: Concentration of nitrogen in the as-received wafer; C_d: Concentration of nitrogen in the doped wafer. 73

Figure 4.5 Concentration depth profiles of aluminum doped by LISPD method measured with SIMS. 74

Figure 4.6 Comparison of concentration of Al and N_2 dopants along the depth of 6H-SiC wafer using similar laser doping parameters. 75

Figure 4.7 Aluminum dopant profiles obtained with an excimer laser. C_a: Concentration of aluminum in the as-received wafer; C_{d1}: Concentration of aluminum in the 1000 laser pulses doped wafer; C_{d2}: Concentration of aluminum in the 3000 laser pulses doped wafer. 77

Figure 4.8 Comparison between the diffusion theory and experimental data for a selected diffusion coefficient in the case of Nd:YAG laser doping of nitrogen in 6H-SiC. .. 89

Figure 4.9 Comparison between the diffusion theory and experimental data for a selected diffusion coefficient in the case of KrF excimer laser doping of aluminum in 4H-SiC. 90

Figure 4.10 Temperature distribution of 6H-SiC during laser direct metallization using the parameters listed in Table 4.4.(a) Bottom surface temperature distribution with the time; (b) Transient temperature distribution along the thickness of the wafer from the bottom surface at the peak temperature (t=48ns). 95

Figure 4.11 Electrode structures in n-type 6H-SiC substrates by different processing: (a) laser direct metallized contacts fabricated on laser heavily doped n^+ substrate (specimen A); (b) laser direct metallized contacts fabricated on original substrate (specimen B); (c) Ni contacts deposited on original substrate (specimen C). 97

Figure 4.12 Current- voltage characteristics between two electrodes on the SiC substrates formed by different methods at room temperature. 100

Figure 4.13 Current- voltage characteristics between two electrodes on the SiC substrates formed by different methods at elevated temperatures: (a) 150 °C; (b) 250 °C..... 101

Figure 5.1 Comparison of the hydrogen content in a 6H-SiC sample of three different qualities. 108

Figure 5.2 XEDS analysis for the carbon contents along the depth of both annealed endolayer specimen and parent wafer: (a) XEDS scanning line showing four locations a, b, c and d along the depth of the endolayer specimen; (b) XEDS scanning line showing four locations a, b, c and d along the depth of the parent specimen; (c) XEDS data for carbon counts along the depth of the specimens. The four locations a, b, c and d are marked on these data to show higher carbon content in the endolayer than in the parent specimen, indicating carbon incorporation into the wafer during the endotaxy experiment........ 111

Figure 5.3 TEM images of cross-sections of an annealed endolayer and parent wafer: (a) Observed amorphous layer in the endolayer specimen; (b) Observed amorphous layer in the parent wafer. 113

Figure 5.4 High-resolution TEM images of cross-sections of an annealed endolayer and parent wafer: (a) The interface between damaged amorphous and crystalline SiC of the endolayer specimen; (b) The interface between damaged amorphous and crystalline SiC of the parent wafer........ 114

Figure 5.5 The aligned and random RBS channeling spectra of parent 6H-SiC sample.116

Figure 5.6 The aligned and random RBS channeling spectra of endolayer specimen. .. 117

Figure 5.7 The aligned and random RBS channeling spectra of annealed endolayer specimen. 118

Figure 5.8 Typical range of resistivities for insulators, semiconductors and conductors. 122

Figure 5.9 Device designs on SiC substrates with and without an endolayer: (a) PIN diode on laser-formed endolayer and (b) reference p-n junction. 125

Figure 5.10 Depth profiles of aluminum concentration in the top laser-doped p region in the endolayer measured by SIMS. 127

Figure 5.11 I-V characteristics of PIN diodes fabricated on an endolayer and a parent 6H-SiC. 128

Figure 5.12 Cross-sectional views of the laser fabricated PIN diodes and referenced Schottky diode. (a) Diode A, with just top laser doped p region; (b) Diode B, with both top laser doped p region (200 nm junction depth) and bottom n+ region; (c) Diode C, with both top laser doped p^+/p region (450 nm junction depth) and bottom n^+ region; and (d) Diode D, reference Schottky diode. 130

Figure 5.13 Temperature distribution of 4H-SiC during laser direct metallization using the parameters listed in Table 5.4.(a) Bottom surface temperature distribution with the time; (b) Transient temperature distribution along the thickness of the wafer from the bottom surface at the peak temperature (t=48ns). 133

Figure 5.14 Measured Schottky diode and PIN diodes I-V curves at room temperature. (a) Schottky diode. (b) Laser fabricated PIN diodes. 137

Figure 6.1 Fabrication of an embedded optical structure. 142

Figure 6.2 Silicon carbide substrate showing an embedded optical structure. 143

Figure 6.3 Experimental set-up for measuring the reflectivity and transmission of laser synthesized optical structures at particular wavelength. 145

Figure 6.4 Reflectivity of parent wafer, C rich phase, C rich phase containing N_2 and C rich phase containing Al measured at 1064 nm. 148

Figure 6.5 Transmission of parent wafer, C rich phase, C rich phase containing N_2 and C rich phase containing Al measured at 1064 nm. 149

LIST OF TABLES

Table 1.1 Comparison of electrical properties of SiC, Si and GaAs [Heft et al. (1995), Zetterling, et al. (2002) and Goldberg et al. (2001)].. 7

Table 1.2 Overview of epitaxy techniques [Stringfellow, (1999)] 18

Table 2.1 The properties and parameters of the SiC wafer used in this study................. 30

Table 2.2 Absorption and heat transfer coefficients of 4H- and 6H-SiC [Levinshtein et al. (2001)].. 48

Table 3.1 Silicon carbide samples used in this study.. 53

Table 4.1 Processing parameters for different laser doping methods............................. 65

Table 4.2 Fitting parameters used in Eqs. 4.32 and 4.33 to compare the theory with experimental dopant profiles in Figs. 4.8 and 4.9 for determining the effective diffusivity.. 91

Table 4.3 Comparison of diffusion coefficients in conventional and laser doping processes for different impurities in SiC and Si. 92

Table 4.4 Processing parameters for laser direct metallization. 94

Table 5.1 Laser processing parameters for endotaxy experiments................................ 105

Table 5.2 Resistances and resistivities of parent sample, endolayer and annealed endolayer... 121

Table 5.3 Laser processing parameters for p-type doping on the endolayer and parent substrate. 124

Table 5.4 Laser processing parameters for p-type doping and laser direct metallization on the Diodes shown in Fig. 5.12. 131

Table 5.5 Comparison of the performance of the PIN diodes fabricated in the literatures and our group. 138

Table 6.1 Laser processing parameters for the synthesis of embedded optical phases. . 140

Table 6.2 Reflectivity and transmission calculation of laser synthesized optical structure 147

LIST OF ACRONYMS/ABBREVIATIONS

A	Absorbance of the SiC substrate
Al_i	Aluminum atoms at the interstitial sites
A_{Ni}	Area of the top Ni contact on the endolayer
Al_{Si}	Aluminum occupying the lattice site of silicon
BOE	Buffered oxide etch
C_a	Concentration of dopants in the as-received wafer
C_0	Dopant concentration at the wafer surface
C_1	Characteristic concentration representing the diffusion process in the far-surface region
C_d	Concentration of nitrogen in the doped wafer
C_{d1}	Concentration of aluminum in the 1000 laser pulses doped wafer
C_{d2}	Concentration of aluminum in the 3000 laser pulses doped wafer
CIVPE	Chloride Vapor-phase Epitaxy
C_p	Specific heat capacity at constant pressure
CVD	Chemical Vapor Deposition
CW	Continuous wave
D	Diffusion coefficient
D. I.	Deionized
D_0	Mass diffusivity
D_0^*	Pre-exponential factor
D_{fs}	Average diffusion coefficient in the far-surface region

DPBs	Double positioning boundaries
d	Wafer thickness
d_e	Thickness of the endolayer
d'	Distance the laser beam travels in the wafer
d*	Distance that the laser beam travels from the beam incident side of the wafer to the top of the embedded structure
E_C	Critical electric field
E_p	Pulse energy
f	Pulse repetition rate
FIB	Focused Ion Beam Instrument
g	Heat source
GILD	Gas immersion laser doping
HVPE	Hydride Vapor-phase Epitaxy
I	Current
I_l	Laser irradiance
I_p	Pulse intensity
JTE	Junction termination extension
k	Thermal conductivity
k_B	Boltzmann constant
LCVD	Laser Chemical Vapor Deposition
LISPD	Laser-induced solid-phase doping
L_m	Mass diffusion length
LPE	Liquid phase epitaxy

LTP	Laser thermal processing
MBE	Molecular beam epitaxy
MJTE	Multistep junction termination extension.
N_c	Nitrogen occupying the lattice site of carbon
N_i	Nitrogen atoms at the interstitial sites
N_v	Vacancy concentration
OMVPE	Organometallic Vapor-Phase Epitaxy
P_0	Incident laser power
PLA	Pulsed laser annealing
PLD	Pulsed laser doping
PLIE	Pulsed laser induced epitaxy
PMOS	Positive Channel Metal Oxide Semiconductor
P_R	Reflected laser power
P_r	Pulse repetition rate
P_T	Transmitted laser power
Q	Activation energy
q	Electronic charge
r_c	Contact resistance
r_0	Laser beam radius
R	Reflectance (Reflectivity) of the SiC substrate
R_{total}	Resistances of the endolayer samples
R_c	Resistances of the contacts
R_e	Resistances of the endolayer

R_s	Resistances of the substrate
RBS	Rutherford Backscattering Spectroscopy
r_c	Specific contact resistance
R_L	Reflectivity of the laser synthesized structures
RTA	Rapid thermally annealing
SBH-ϕ_B	Schottky Barrier Height
SIMS	Secondary Ion Mass Spectroscopy
SPE	Solid phase epitaxy
T	Temperature
T_0	Initial temperature of the substrate
T_A	Activation temperature for the diffusion process
TEM	Transmission Electron Microscopy
t_{irr}	Total laser irradiation time (pulse-on plus pulse-off times)
T_L	Transmission of the laser synthesized structures
TMA	Trimethyaluminum
t_{on}	Pulse length (pulse-on time)
t'	Diffusion time in the far-surface region
v	Laser scanning speed
V	Voltage
V_B	Breakdown voltage
V_c	Carbon vacancies
V_{Si}	Silicon vacancies
VPE	Vapor phase epitaxy

N_D	Dopant concentration
UHV	Ultrahigh-vacuum
W	Drift layer thickness
XEDS	X-ray Energy Dispersive Spectrometry

Greek Symbols

α	Thermal diffusivity
σ	Electric conductivity
ρ	Density
ρ_e	Resistivities of the endolayers
λ	Wavelength
η	Absorption coefficient of the original wafer
ϕ_B	Schottky Barrier Height
ϕ_p	Pulse fluence
ϕ_{th}	Threshold ion dose
τ_{on}	Pulse-on time
ε	Dielectric constant
ε_0	Permittivity of vacuum,
ε_r	Relative dielectric constant of SiC

LIST OF PUBLICATIONS

Journal Papers

1. Z. Tian, N.R. Quick and A. Kar, Laser Enhanced Diffusion of Nitrogen and Aluminum Dopants in Silicon Carbide, submitted to Acta Materialia.
2. Z. Tian, N.R. Quick and A. Kar, Laser Endotaxy and PIN Diode Fabrication of Silicon Carbide, submitted to Journal of Electronic Materials.
3. Z. Tian, I.A. Salama, N.R. Quick and A. Kar, Effect of Different Laser Sources and Doping Methods Used to Dope Silicon Carbide, Acta Materialia, Vol. 53, 2005, pp. 2835- 2844.
4. Z. Tian, N.R. Quick and A. Kar, Characteristics of 6H-Silicon Carbide PIN Diodes Prototyping by Laser Doping, Journal of Electronic Materials, Vol. 34, 2005, pp. 430-438.

Conference Papers

1. Z. Tian, N.R. Quick and A. Kar, Laser Endotaxy and PIN Diode Fabrication of Silicon Carbide, Symposium B: Silicon Carbide — Materials, Processing and Devices, edited by M. A. Capano, M. Dudley, T. Kimoto, A. R. Powell and S. Wang, (San Francisco, California, 2006), B10.7.
2. Z. Tian, N.R. Quick and A. Kar, Laser Direct Write Doping and Metallization Fabrication of Silicon Carbide PIN Diodes, in International Conference on Silicon Carbide Related Metarials Proc., Pittsburgh, PA, 2005.

3. Z. Tian and A. Kar, Nd:YAG Laser Surface Treatment of Coating on Polyimide Substrate, ICALEO (International Congress on Applications of Lasers and Electro-Optics), Miami, Florida, 2005.
4. Z. Tian, N.R. Quick and A. Kar, Fabrication of Silicon Carbide PIN Diodes by Laser Doping and Planar Edge Termination by Laser Metallization, Symposium E: Semiconductor Defect Engineering — Materials, Synthetic Structures and Devices, edited by S. Ashok, J. Chevallier, B.L. Sopori, M. Tabe and P. Kiesel, (Mater. Res. Soc. Symp. Proc. 864, San Francisco, California, 2005), E9.3.
5. Z. Tian, N.R. Quick and A. Kar, Laser-Synthesis of Optical Structures in Silicon Carbide, in Symposium "State-of-the-Art Program on Compound Semiconductors SLII", 207th Meeting of the Electrochemical Society, (Quebec City, Canada, May 15-20, 2005).
6. Z. Tian, N.R. Quick and A. Kar, Laser Doping of Silicon Carbide and PIN Diode Fabrication, in Proceeding of the 23rd International Congress on Application of Laser & Electro-Optics, (San Fransicso, California, October 4-7, 2004), M306.
7. Z. Tian, N.R. Quick and A. Kar; Laser Direct Write and Gas Immersion Laser Doping Fabrication of SiC diodes, in Silicon Carbide 2004-Materials Processing and Devices, edited by Michael Dudley, Perena Gouma, Tsunenobu Kimoto, Philip G. Neudeck, and Stephen E. Saddow (Mater. Res. Soc. Symp. Proc. 815, Warrendale, PA, 2004), J3.4
8. Z. Tian, N.R. Quick and A. Kar, Laser Direct Metallization and Doping of 6H-SiC, Session III: Electronic Materials, Annual Joint Symp. Florida Society for Microscopy and Florida Chapter of the American Vacuum Society, Orlando, Florida, March 8-9, 2004 (invited presentation).

CHAPTER 1: INTRODUCTION AND LITERATURE REVIEW

1.1 Motivation

Silicon carbide (SiC) is a promising semiconductor material for high-voltage, high-frequency and high-temperature devices due to its wide bandgap (2.36-3.5 eV), high breakdown electric field strength (3-5 MV/cm), high saturated drift velocity of electrons (2×10^7 cm/s) and high thermal conductivity (350-490 $Wm^{-1}K^{-1}$) [Heft et. al (1995) and Levinshtein et. al (2001)].

However, there are still technology barriers for silicon carbide device fabrication including micropipe defects in the substrate and processing limitations (e.g., dielectric deposition, etching, oxidation, metallization, and doping). One of these challenges is metallization for source, drain and gate contacts on devices. Metal conductors generate strains due to thermal expansion coefficient mismatch resulting in debonding, or can create charge carrier traps, particularly dislocations, which decrease the device efficiency. Also, metal conductors can oxidize and react with chemical species in hostile environments degrading their conductive properties and further creating chemical products that can eventually affect the device [Sengupta et. al (2001)].

Doping is another challenge for SiC device fabrication due to its hardness, chemical inertness and the low diffusion coefficient of most impurities [Edwards et al. (1997)].

Current doping techniques for SiC device fabrication include epilayer doping and ion implantation. Epilayer doping is in situ doping during chemical vapor deposition (CVD) epitaxial growth; Nitrogen (N) or phosphorous (P) for n-type, aluminum (Al) or boron (B) for p-type and vanadium (V) for semi-insulating type are introduced. Ion implantation is the most common doping technique used for fabricating SiC devices currently. However, it generates implantation-induced defect centers in the wafer and therefore, high annealing temperatures are required to remove these defects and to electrically activate the dopants. Some defects remain in SiC for up to 1700°C annealing temperatures [Troffer et. al (1997)]. Annealing at these high temperatures can cause severe surface damage due to Si sublimation and redistribution [Handy et. al (2000)].

With the aim of overcoming some challenges in metallization and doping during the fabrication of silicon carbide devices, a novel laser direct write technique is provided to direct metallize the surface of silicon carbide without metal deposition and dope in silicon carbide instead of conventional ion implantation.

Laser irradiation of SiC in an inert ambient at appropriate processing parameters induces a conversion in the electric properties by changing the surface stoichiometry at the laser-irradiated spot. This process forms electrically conductive phases with a metal-like behavior that can act as either Ohmic or rectifying contact without any metal deposition with respect to the untreated SiC. It can also serve as interconnects for devices built on SiC substrate [Salama (2003)].

Laser irradiation of SiC in a dopant-containing ambient allows to simultaneously heating the SiC surface and incorporating dopant atoms into the SiC lattice. This laser doping process can enhance the dopant diffusivity compared to conventional high temperature furnace diffusion process and reduce defect generation compared to ion implantation method. It can also realize selective area doping and dopant and conductivity level control [Salama (2003)].

1.2 Literature Reviews

1.2.1 Silicon Carbide

As a wide bandgap (2.0 eV $\leq E_g \leq$ 7.0 eV) [Casady and Johnson (1996)] semiconductor material, silicon carbide (SiC) has attracted increasing attention for high-power, high-frequency, high-temperature and radiation-resistant devices due to its unique structure and attractive properties.

Silicon carbide is the only chemically stable form of silicon and carbon. The crystalline structure of SiC can be considered to consist of the close-packed stacking of double layers of Si and C atoms [Harris (1995)]. The stacking of the double layers follows one of three possible relative positions, which are arbitrarily labeled A, B and C, each letter representing a bilayer of individual Si and C atoms. Different stacking sequences of these three double layers result in SiC's large number of polytypes. Polytypism is a one-

dimensional polymorphism that is a result of the stacking sequence [Harris (1995)]. There are more than 200 different polytypes of SiC crystallizing mainly in three lattice structures, i.e., cubic, hexagonal and rhombohedral [Pensel and Choyke (1993)]. The most common polytypes of SiC, which are developed for electronics currently, are 3C-SiC, 4H-SiC, and 6H-SiC. 3C-SiC with stacking sequence of ABCABC, or known as β-SiC, is the only polytype of SiC in a cubic lattice structure. Correspondingly, the non-cubic polytypes of SiC are referred to as α-SiC [Pearton (2000)]. 4H- and 6H-SiC, with stacking sequences of ABCBABCB and ABCACBABCACB, respectively, are only two of many possible SiC polytypes with hexagonal crystal structure [Neudeck (2000)].

Different polytypes of SiC have different physical and electronic properties. Among these three polytypes of SiC presently being developed for electronics, the bandgap energy at room temperature varies from 2.36 eV for 3C-SiC and 3.0 eV for 6H-SiC to 3.23 eV for 4H-SiC [Goldberg et al. (2001)]. The wide bandgap is the key to almost all advantages of using SiC in devices. Other important parameters that affect device performance include electron and hole mobility. 4H-SiC has the highest electron mobility ($\leq 900\ cm^2/Vs$) and 3C-SiC has the highest hole mobility ($\leq 320\ cm^2/Vs$) and high electron mobility second to 4H-SiC ($\leq 800\ cm^2/Vs$); while 6H-SiC has the lowest electron mobility ($\leq 400\ cm^2/Vs$) and hole mobility ($\leq 90\ cm^2/Vs$). Also, the anisotropy of electron mobility in 6H-SiC is much more than that in 4H-SiC. The ratio of the electron mobility along the normal to the basal plane ($\mu_\perp$) to that in the basal plane ($\mu_{//}$) is about 0.7-0.83 at 300 K in 4H-SiC, while the same ratio is about 6 in 6H-SiC [Pearton (2000)]. However, the minority carrier

lifetime is usually longer in 6H-SiC than in 4H-SiC, which can compensate the low electron mobility in 6H-SiC for bipolar-type power device applications [Fujihira et al. (2002)]. Furthermore, the quality and size of 6H-SiC are more advanced than that for 4H-SiC.

Compared to other semiconductor materials such as silicon and gallium arsenic (GaAs), SiC has superior properties in many aspects that are crucial for integrated device fabrication. The comparison of electrical properties of SiC, Si and GaAs is listed in Table 1. SiC's wide bandgap (2.36-3.23 eV), high breakdown electric field strength (3-5 MV/cm), high saturated drift velocity of electrons (2×10^{7} cm/s) and high thermal conductivity (350-490 $Wm^{-1}K^{-1}$) make it an very attractive semiconductor material for high-power, high- frequency, high-temperature device applications [Heft et al. (1995) and Goldberg et al. (2001)].

1.2.2 Current Technology Barriers in Silicon Carbide Device Fabrication

There are still some technology barriers for silicon carbide device fabrication such as dielectric deposition, etching, oxidation, metallization and doping. One of these challenges is metallization for source, drain and gate contacts on devices.

Metallization Contact in SiC

When a metal and a semiconductor are brought into contact, a rectifying or ohmic contact can be formed. The critical parameter that determines whether a contact is of ohmic or

rectifying nature is the Schottky barrier height (SBH-ϕ_B). An ohmic contact requires low ϕ_B while high value of ϕ_B is needed for a rectifying contact. An ohmic contact is defined as having a linear and symmetric current-voltages and an extremely small resistance in comparison to the bulk of the device. The main purpose of an ohmic contact is to allow the outside communication of a device. A contact is of rectifying type when it allows current flow under only one voltage bias regime (positive or negative) and thus becomes an important factor of the active region of a device [Constantinidis et al. (1997)].

For SiC, most metals can easily form a rectifying contact on SiC, such as Au, Al, Pd, Ni on n-type SiC and Al, Ni, NiAl, Au on p-type SiC, with low leakage current, low ideality factor, high breakdown voltage and Schottky barrier height (SBH-ϕ_B) in excess of 1 eV depending on the polytype, doping type and dopant concentration. It is more difficult to form an ohmic contact on SiC with low contact resistance which may be overcome by heavy doping of the SiC and using an insulator interlayer to reduce the barrier height and up to now ohmic contact has been realized on SiC such as Ni, Ti, Mo, Ni-Cr, TiW on n-type SiC and Al, Ti, Mo, Al-Ti on p-type SiC [Porter et al. (1995)].

However, metal conductors generate strains due to thermal expansion coefficient mismatch resulting in debonding, or can create charge carrier traps, particularly dislocations, which decrease the device efficiency. Also, metal conductors can oxidize and react with chemical species in hostile environments degrading their conductive properties and further creating chemical products that can eventually affect the device [Sengupta et al. (2001)].

Table 1.1 Comparison of electrical properties of SiC, Si and GaAs [Heft et al. (1995), Zetterling, et al. (2002) and Goldberg et al. (2001)].

	Silicon Carbide			Si	GaAs
	3C-SiC	4H-SiC	6H-SiC		
Energy gap (eV)	2.36	3.23	3.0	1.12	1.43
Breakdown field (Mv/cm)	2.0	2.2	2.5	0.25	0.3
Electron saturation velocity (10^7 cm/sec)	2.5	2.0	2.0	1.0	1.0
Electron mobility (cm^2/Vs)	≤ 800	≤ 900	≤ 400	1400	8500
Hole mobility (cm^2/Vs)	≤ 300	≤ 120	≤ 90	500	4500
Thermal conductivity (W/cm K)	3.6	3.7	4.9	1.5	0.46
Thermal diffusivity (cm^2/s)	1.6	1.7	2.2	0.9	0.24

Doping in SiC

Doping is another challenge for SiC device fabrication due to its hardness, chemical inertness and the low diffusion coefficient of most impurities [Edwards et al. (1997)]. Current doping techniques for SiC device fabrication include epilayer doping and ion implantation. Epilayer doping is in situ doping during chemical vapor deposition (CVD) epitaxial growth; Nitrogen (N) or phosphorous (P) for n-type, aluminum (Al) or boron (B) for p-type and vanadium (V) for semi-insulating type are introduced.

Ion implantation is the most common doping technique used for fabricating SiC devices currently. This processing is done in ion implanter, one of the most complex semiconductor processing tools (Fig. 1.1). The basic process of ion implantation is that a beam of the desired dopant ions, which are created from a source material, extracted and separated in a mass analyzer, is accelerated in a voltage field to attain a high velocity to implant the dopants into the semiconductor crystal lattice structure of the target wafer [Quirk and Serda (2001)]. Implantation is followed by a thermal anneal step to activate the dopant ions in the crystal structure. In ion implantation, doping concentrations and doping profiles can be adjusted reproducibly and varied over a wide range; doping selected areas through masking techniques is possible, which avoids lateral structuring with wet and dry etching techniques; and basically all stable elements of the periodic table can be implanted [Zetterling et al. (2002)].

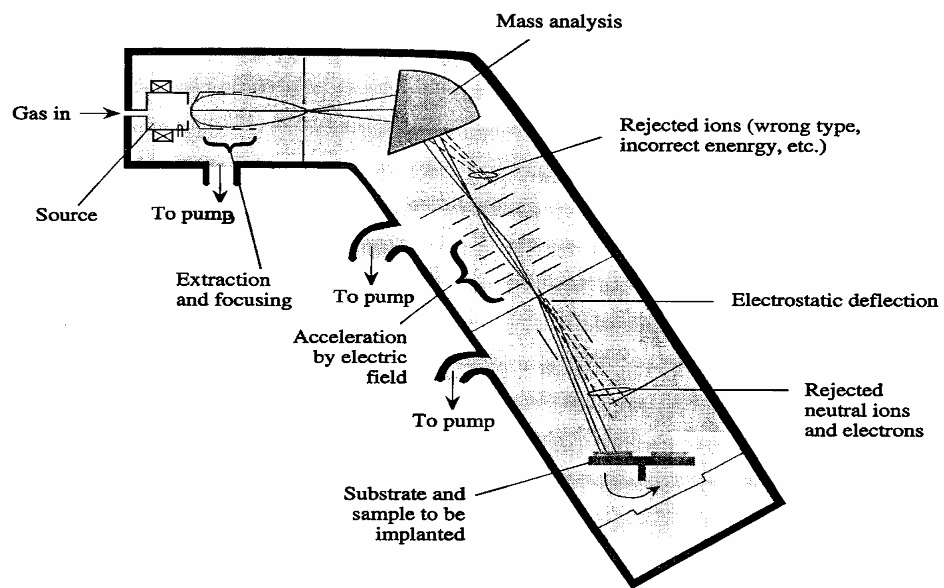

Figure 1.1 A schematic of doping by ion implantation [Singh (2001)].

However, ion implantation generates implantation-induced defect centers in the wafer and therefore, high annealing temperatures are required to remove these defects and to electrically activate the dopants. Some defects remain in SiC for up to 1700°C annealing temperatures [Troffer et al. (1997)]. Moreover, annealing at these high temperatures can cause severe surface damage due to Si sublimation and redistribution [Handy et al. (2000)].

To avoid high temperature annealing after ion implantation, pulsed laser annealing (PLA) has been used to suppress the ion-implanted defects and electrically activate ion-implanted dopants. The use of high powerful pulsed laser beams in the nanosecond duration regime deposits a large amount of energy in very short time into the near-surface region without evidently affecting the substrate temperature [Dutto et al. (2001)]. Under different laser processing conditions, irradiation can lead to surface melting of SiC to a depth of a few hundred nanometers or just annealing in solid phase without surface melting. The highly non-equilibrium nature of the melt/regrowth process is able to achieve complete electrical activation of the dopants; while surface degradation and change in the material stoichiometry are difficult to avoid [Dutto et al. (2003)]. Chou et al. [Chou et al. (1990)] demonstrated the removal of implantation damage in 6H-SiC using a pulsed excimer laser. They reported that molten SiC regrows epitaxially on the underlying substrate after the surface melting and the implanted Ga atoms significantly redistributed, which can only be explained by liquid phase diffusion of the Ga atoms. Ahmed et al. [Ahmed et al. (1995)] demonstrated the electrical activation of N^+ and Al^+ ion-implanted layer in 6H-SiC using XeCl excimer laser irradiation; however, the

problem of a significant redistribution of the dopanted dopants due to surface melting or ablation still exist. Eryu et al. [Eryu et al. (2001)] reported the electrically activation of ion-implanted impurities without melting the surface region by repeated laser irradiation at low energy density. The process induced little redistribution of implanted impurities after laser irradiation. Tanaka et al. [Tanaka et al. (2003)] drastically improved the electrically activation efficiency of the dopants by using a "multiple energy irradiation method" without ablation of the surface atoms and redistribution of the dopants while the substrate temperature was kept in the range of 500-700 °C.

Lasers have also been used to incorporate dopants into semiconductor wafers and such techniques have been classified as laser thermal processing (LTP), gas immersion laser doping (GILD) and laser-induced solid-phase doping (LISPD). The LTP method is a two-step process in which ion-implantation is used at first and then a pulsed laser beam is employed to induce a melting and solidification cycle over a given depth of the wafer. Highly doped layers (up to $\approx 3\times 10^{21}$ cm^{-3} of B atoms) with thickness of the order of 10 nm in Si wafers have been achieved by using this technique [Kerrien et al. (2003)]. The GILD method involves direct incorporation of dopants into the molten layer created by a laser beam, as shown in Fig. 1.2. In this method a dopant-containing gas, which is adsorbed at the wafer surface, is pyrolyzed with a laser beam to produce the dopant species. The dopant atoms diffuse into the molten silicon layer and then occupy electrically active sites during epitaxial recrystallization of the melt [Jones et al. (1998)]. This process was used to fabricate a variety of junctions by doping Si wafers using an excimer laser: ultra-shallow (junction depths ranging from 14 to 65 nm) and highly doped

junctions (up to ≈ 3× 10^{21} cm^{-3} of B atoms) [Kerrien et al. (2004)], source-drain junctions of submicrometer PMOS (junction depths ranging from 25 to 150 nm and peak concentrations up to 10^{21} cm^{-3} of B atoms) [Carey et al. (1988)], p^+/n and n^+/p diodes (junction depths ranging from 30 to 200 nm and peak concentrations approaching 10^{21} cm^{-3} of B and P atoms for p-type and n-type regions respectively) [Weiner et al. (1993)], and source and drain regions of self-aligned aluminum top-gate polysilicon thin-film transistors [Giust et al. (1997)]. The wafer is not melted in the LISPD method, which is based on the solid-state diffusion for dopant incorporation through one of the following two techniques: (i) the dopant film method and (ii) the dopant gas method. In the dopant film method, a thin film of the dopant material is deposited on the wafer surface and then the film is heated with a laser beam to diffuse the dopant atoms from the film to the wafer. In the dopant gas method, the wafer is placed in a chamber to which a dopant-containing vapor, such as an organometallic compound, is supplied with an inert gas (e.g., Ar) and the wafer is heated with a laser beam. The dopant atoms are produced at the laser-heated wafer surface upon pyrolysis of the vapor and the diffusion of such atoms into the wafer occurs at fairly high temperatures. A suitable liquid medium can also be utilized to accomplish doping by the LISPD method instead of using the vapor medium. P-n junctions were fabricated in different semiconductors such as GaAs, GaP, InP and Si (junction depth ~350 nm and peak concentration approaching 10^{20} cm^{-3} of B atoms in Si) by the LISPD method using a CO_2 laser [Bonchik et al. (2001) and Pokhmurska et al. (2000)].

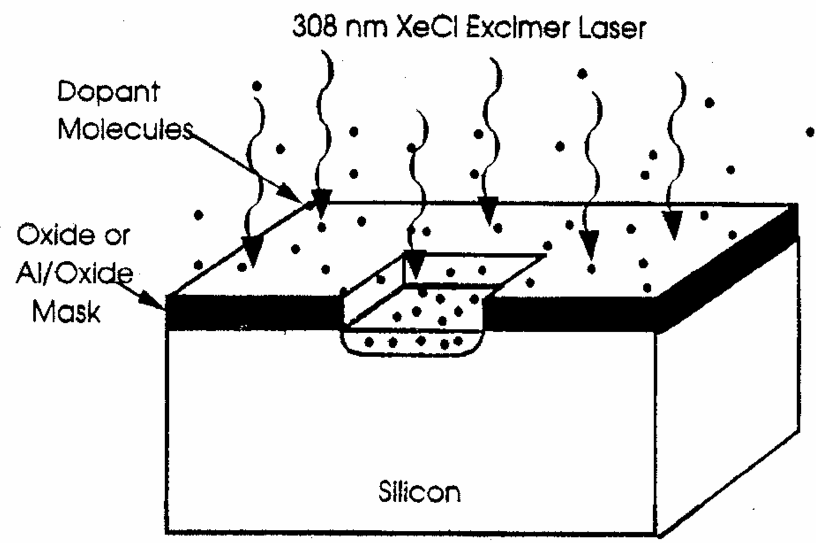

Figure 1.2 Illustration of GILD process [Jones et al. (1998)].

1.2.3 Fabrication of Silicon Carbide PIN Diodes

SiC PIN diodes have a strong potential for use in high speed and high power electronics applications, especially operating for high temperature operating conditions. SiC PIN diodes are typically fabricated by choosing a $p^+/n^-/n^+$ SiC structure, i.e., growing a p^+ homoepitaxial layer on n^- SiC epitaxial layer that is grown on n^+ SiC substrate. In some cases edge termination such as Junction Termination Extension (JTE), field plates, floating guard rings and junction beveling is designed to increase breakdown voltage of the diodes by reducing electric field crowding at the device edge. A typical PIN diode structure with a shallow mesa JTE is shown in Fig. 1.3. The performance of the diodes depend on several factors such as the growth of pure, low defect density epitaxial layers, doping concentrations of p^+ and n^- layers, thickness of n^- layer and the design of edge termination, etc. Fujihira et al. [Fujihira et al. (2002)] fabricated 6H-SiC PIN diodes using $p^+/p/n^-/n$ homoepitexial layers grown on highly doped (5×10^{18}cm^{-3}) n-type substrates, exhibiting a high breakdown voltage of 4.2 kV with a low on-resistance of 4.6 m$\Omega\cdot$cm^2 and fast switching with a turn-off time of 0.18 μs at 300 K. A 5.5 kV 4H-SiC PiN rectifier was fabricated by Singh et al. [Singh et al. (2002)] using a $p^+/n^-/n$ structure and a p-type junction termination extension (JTE) as the planar edge termination method to gradually reduce the electric field from the edge of the SiC diode to the outer periphery of the device structure. Their reverse bias measurement up to 5 kV showed that the leakage current increases by only one order of magnitude for the temperature rise from the room temperature to 573 K. A 4H-SiC ultra high voltage PIN diode fabricated by

Sugawara et al. [Sugawara et al. (2001)] using a $p^+/n^-/n$ structure and a shallow mesa JTE exhibits the breakdown voltage of 19 kV.

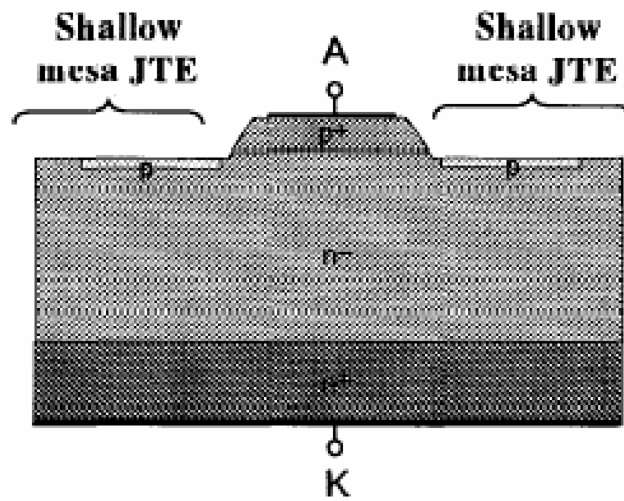

Figure 1.3 Cross-sectional structure of 4H-SiC UHV diode with shallow mesa JTE [Sugawara et al. (2001)].

1.2.4 Epitaxial Growth of Silicon Carbide

The driving force for growing epitaxial layer on substrates is that certain devices such as detectors and light-emitting diodes require multilayer structures for optimal performance. Epitaxy can be broadly classified into two categories, i.e., homoepitaxy and heteroepitaxy. In homoepitaxy the composition of the layer is essentially the same as that of the underlying substrate while epitaxy is termed hetoroepitaxy when the composition of the layer differs from that of the substrate [Mahajan and Sree Harsha (1998)]. Compared with hetoroepitaxy, homoepitaxy growth can result in higher quality layers [Kern et al. (1997)]. Techniques available for depositing layers can be broadly classified into four groups: (1) vapor phase epitaxy (VPE), (2) liquid phase epitaxy (LPE), (3) molecular beam epitaxy (MBE), and (4) solid phase epitaxy (SPE). The strengths and weaknesses of various epitaxy methods are listed in Table 1.2.

For epitaxy SiC growth, polytype control, doping control and defect reduction are basic consideration. The dominate methods for epitaxy SiC growth are vapor phase epitaxy and molecular beam epitaxy. The basic principle for VPE is to feed precursor gases diluted in a carrier gas into a reaction chamber, where growth takes place on a heated seed crystal [Nordell (2002)]. For MBE, elemental sources are evaporated at a controlled rate onto a heated substrate under ultrahigh-vacuum (UHV) conditions [Stringfellow (1999)]. Compared with VPE, MBE can offer cleaner ambient and lower deposition temperatures [Kern et al. (1997)].

Kaneda et al. [Kaneda et al. (1987)] reported that p-type epitaxial 3C-SiC (111) was grown on n-type 6H-SiC (0001) substrate by solid source MBE using electron beam heated solid sources of C and mixed Si/B. The breakdown field of resulting p-n junction, 6.7×10^5 Vcm^{-1}, is comparable with values of p-n junction formed by other growth methods. Fissel et al. [Fissel et al. (1995)] grown 3C-SiC on vicinal 6H-SiC (0001) substrates at modest growth rates (1 nm min^{-1}) below 1000 °C using their "Si-stabilized" growth method. However, the quality of the deposited film displayed many stacking faults, double positioning boundaries (DPBs), rough surfaces and non-uniform surface coverage. Kern et al. [Kern et al., (1997)] grown 3C-SiC(111) films with DPBs and stacking faults on both vicinal and on-axis 6H-SiC (0001) substrates at temperatures between 1000 and 1500 °C; the same group also grown 6H-SiC (0001) films with low defect densities on vicinal 6H-SiC (0001) substrates by adding H_2 to the reactant mixture at temperatures between 1350 and 1500 °C.

Table 1.2 Overview of epitaxy techniques [Stringfellow, (1999)]

Techniques	Strengths	Weaknesses
Liquid-Phase Epitaxy (LPE)	Simple, High purity, low impurity and point defect levels	Poor thickness uniformity, difficulty in growing Al and In
Chloride Vapor-phase Epitaxy (CIVPE)	Simple High purity	No Al alloys, Sb alloys difficult, >20-Å interface widths
Hydride Vapor-phase Epitaxy (HVPE)	Well developed Large scale	No Al alloys, Sb alloys difficult, complex process/reactor, control difficult, hazardous precursors
Organometallic Vapor-Phase Epitaxy (OMVPE)	Most flexible, abrupt interfaces, high purity, simple reactor, robust process, uniform, large scale, high growth rates, selective growth, In situ monitoring	Expensive reactants, most parameters to control accurately, Hazardous precursors
Molecular-Beam Epitaxy (MBE)	Simple process, Uniform, Abrupt interfaces, In situ monitoring, A cleaner ambient, Lower deposition temperatures	As/P alloys difficult, Sb alloys difficult, N materials difficult, "Oval" defects, Low throughput, expensive (capital)
Solid-Phase Epitaxy (SPE)	Applicable to a variety of material systems, for which epitaxial thin film growth is difficult.	
Laser Chemical Vapor Deposition (LCVD)	Maskless selective epitaxial growth, low substrate temperature, high deposition rate, in-situ multicomponent device integration on the same wafer, clean epilayer	Special cases

Vapor phase epitaxy has advantages in the precise control and uniformity of epilayer thickness and impurity doping. However, there had been a serious problem of polytype mixing in VPE growth of α-SiC [Yoshida et al. (1987)]. A new technique named "step-controlled epitaxy" solved this problem successfully. In this technique the polytype of epilayers can be controlled by surface steps existing on the off-substrates. The breakthrough of this technique lies in that growth temperature can be reduced more than 300 °C and epilayers deposited have very high quality enough for device applications [Kimoto et al. (1997)]. Using this technique high quality single crystalline α-SiC homoepitaxial layers have been successfully produced [Karmann et al. (1992) and Rupp et al. (1995)].

1.2.5 Laser Interaction with Semiconductors

The interaction mechanisms between laser beam and matter depend on the parameters of the laser beam and the physical and chemical properties of the material. Laser parameters include the wavelength, intensity, spatial and temporal coherence, polarization, angle of incidence, and dwell time (illumination time at a particular site). While the material is characterized by its chemical composition and microstructure, i.e., the arrangement of atoms or molecules within a solid, which determine the type of elementary excitations and the interaction between the laser and matter [Bäuerle (2000)].

As far as laser processing of semiconductor is concerned, this process depends upon how laser energy is introduced into the material and this starts with excitation of electrons that

the photons of a laser can couple [Brown (1983)]. The strength of the coupling is heavily dependent on the laser wavelength and the material. The excitation mechanisms involved can be divided into two major types: hole-electron pair generation and free carrier absorption [Brown (1983)]. In the hole-electron pair generation mechanism, a photon with high enough energy is capable of breaking an electronic bond, promoting an electron from the valence to the conduction band of the semiconductor and thus providing a free electron and a corresponding free hole. Electronic band structure of semiconductors can be altered by doping and correspondingly hole-electron pair generation takes place for relatively lower energy photons. In the second excitation mechanism, photons are absorbed by free electrons or holes and are promoted to higher energy states within the conduction or valence bands. Such absorption depends directly on the density of free carriers present in the semiconductors.

Laser processing of semiconductors can be viewed as dominantly thermal because the material gets heated by energy rapidly flowing from the laser beam to the electrons and then to the vibrating lattice. The time of energy transfer from electrons to the lattice by generation of phonons (elementary lattice vibrations) was estimated $>10^{-11}$ s but $<10^{-8}$ s [Gamo et al. (1981)]. So the laser can be considered as an intense source of localized heat. However, the thermal behaviors of the semiconductors under different laser irradiation mode of operation, continuous wave (CW) and pulsed, are quite different. A CW laser beam provides a continuous heating to the material during a certain time and the material cools when the laser radiation is switched off. While in the pulsed mode, the energy is supplied at regular intervals with cooling periods.

1.2.6 Temperature Distribution during Laser Irradiation Process

Temperature rise induced by the absorbed laser irradiation on a material surface or within its bulk is a basic quantity in laser processing and knowing the temperature distribution is a prerequisite for both fundamental investigations and technical applications. The physical phenomena involved in the material heating by laser irradiation, such as surface heat treatment, melting and evaporation can be described by the well-known heat conduction differential equation. This partial differential equation can be solved by numerical methods or analytical methods. The main disadvantages of the numerical methods include the development and implementation of algorithms and the high acquisition cost of the commercial software; while the limitation of analytical methods lie in such methods are not suitable when the mathematical description of the physical phenomena leads to a non-linear equation, where the material properties are temperature dependent [Conde et al. (2002)].

Temperature profiles of various physical phenomena such as surface heat treatment, surface melting and evaporation in different materials (metals, semiconductors, polymers, etc.) under certain laser processing conditions (CW or pulsed, stationary or scanning laser beam, circular or rectangular beam, etc.) has been determined by many researchers. Cline and Anthony [Cline and Anthony (1977)] derived a temperature field for laser heating and melting materials for a Gaussian beam moving at a constant velocity. Chen and Lee [Chen and Lee (1983)] obtained the temperature profiles of a semi-infinite slab heated with a scanning laser beam and considered the effects of the scanning velocity, the beam

radius and the beam shape on the temperature. Tokarev and Kaplan [Tokarev and Kaplan (1999)] solved the one-dimensional time dependent heat conduction equation for surface heating with a solid-melt phase boundary for a rectangular pulse laser beam. Kar et al. [Kar et al (1996)] presented an expression for the temperature distribution during laser heating with single or multiple rectangular chemical oxygen-iodine laser beams. Mazhukin et al. [Mazhukin et al. (1995)] presented a mathematical model including the processes of heating, melting-solidification and evaporation of superconducting ceramics in pulsed laser action by numerical simulation. Conde et al. [Conde et al. (2002)] calculated the spatial and temporal temperature distribution in a material by the Green function for both CW and pulsed laser radiation.

1.3 Objectives

The purpose of this project is to provide a laser-based process for metallization and doping to laser direct metallize without metal deposition and laser dope in SiC without high temperature annealing, as an alternative to the conventional ion implantation, and find applications of this laser direct write metallization and doping technique on the fabrication of PIN diodes, endotaxial layer and optical structure on SiC substrate.

The research includes the following studies:

- Temperature distribution of silicon carbide substrate during laser metallization and doping process.
- Realization of laser direct metallization on silicon carbide substrate.

- N-type and p-type doping on silicon carbide wafer by different laser sources and concentration profile characterization of n-type and p-type dopants.
- Diffusion model of dopants during laser doping process.
- Laser fabrication of endotaxial layer on SiC substrate.
- Laser fabrication and electrical characterization of SiC PIN diodes on different mediums.
- Laser fabrication and characterization of embedded optical structure.

CHAPTER 2: TEMPERATURE DISTRIBUTION ANALYSIS DURING LASER METALLIZATION AND DOPING PROCESS OF SILICON CARBIDE

2.1 Introduction

The aim of this chapter is to present the analysis results on mathematical modeling of the temperature distribution of the wafers irradiated by the lasers to optimize the laser processing parameters and help understanding the mechanisms of laser metallization and doping process.

Depending on the laser energy absorption characteristics of the substrate at different wavelengths, two distinct heating mechanisms can be envisaged during laser irradiation. One of the mechanisms is laser internal heating while the other one is surface heating as illustrated in Fig. 2.1. The internal heating mechanism (Fig. 2.1a) can be achieved with a Nd:YAG laser (λ=1064 nm) because of its low absorption coefficient in SiC. When the laser beam is incident on the top polished surface of the SiC wafer, a fraction of its energy is reflected and the rest of the energy propagates through the wafer towards the bottom surface. Since the bottom surface is unpolished in this study, most of the energy is absorbed by this surface. To achieve the surface heating (Fig. 2.2b) mechanism, A excimer laser (λ=193, 248, 351 nm for ArF, KrF and XeF lasing media respectively) is used because of its high absorption coefficient in SiC. When the excimer laser beam is incident on the top surface of the wafer, the laser energy is directly absorbed by this

surface. Since the heating is localized at the top surface, the wafer can be doped to a very small depth in this case.

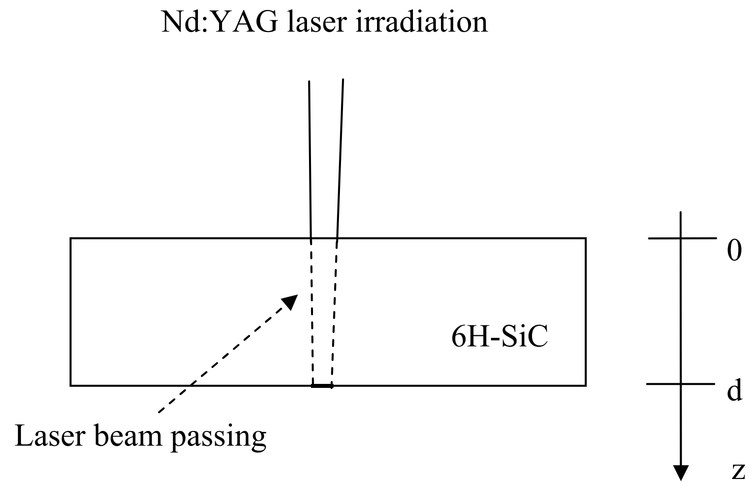

(a)

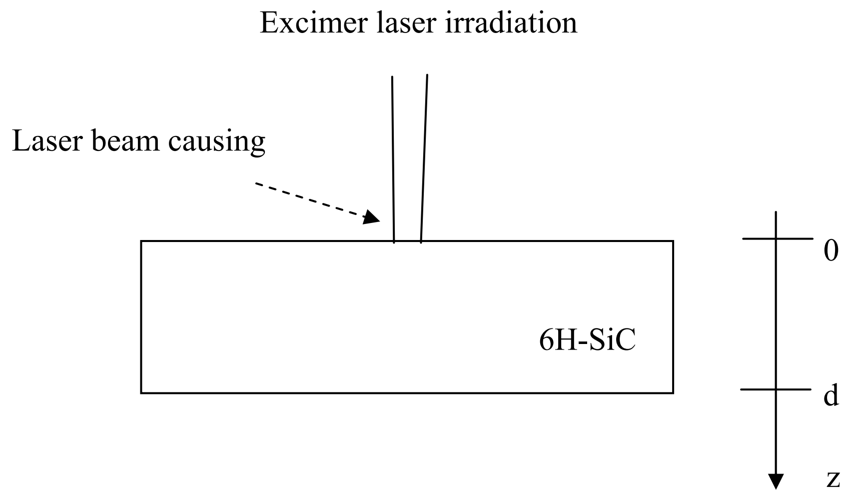

(b)

Figure 2.1 Different heating mechanisms for laser irradiation: (a) Volumetric heating during Nd:YAG laser irradiation and (b) Surface heating during excimer laser irradiation.

2.2 Mathematical model and analysis of laser internal heating

2.2.1 Mathematical model and solution

The determination of the temperature distribution due to a scanning Gaussian laser beam would require solving a three-dimensional heat conduction equation. However, a one-dimensional model is considered in this study for a stationary Gaussian beam to simplify the analysis. Such a model is a very good approximation because the heat flux is very large in the z direction, i.e, in the direction of laser beam propagation. The heat flux in the other two orthogonal directions would be comparatively low because of high thermal conductivity of SiC. Additionally the dopant atoms diffuse predominantly in the z direction for which a one-dimensional diffusion model would be adequate. However, the temperature will decrease radically for a beam of finite diameter. This trend in the temperature distribution is approximated through the Gaussian irradiance profile of the beam. Also the model is based on constant optical and thermo physical properties of the substrate.

The governing equation can be expressed by:

$$k\frac{\partial^2 T}{\partial x^2} + g = \rho C_P \frac{\partial T}{\partial t} \tag{2.1}$$

Where g is heat source and $g = \dfrac{-\partial[(1-R)I_0 e^{-2r^2/r_0^2} e^{-\mu x}\phi(t)]}{\partial x}$ (2.2)

in which $\phi(t)$ defines the triangular shape of the laser pulse.

$$\phi(t)=\begin{cases}\dfrac{t-nt_p}{t_{pk}} & nt_p \le t \le nt_p+t_{pk} \\ -\dfrac{(t-t_{on}-nt_p)}{t_{on}-t_{pk}} & nt_p+t_{pk}<t\le nt_p+t_{on} \\ 0 & nt_p+t_{on}\le t\le (n+1)t_p \end{cases} \qquad n=0,1,2,\Lambda \tag{2.3}$$

Boundary conditions are described by:

$$\frac{\partial T}{\partial x}=0 \qquad \text{at x = 0} \tag{2.4a}$$

$$k\frac{\partial T}{\partial x}=AI_d \qquad \text{at x = d} \tag{2.4b}$$

In which the heat losses caused by the ambient are neglected.

Take Laplace transform of Eq. (2.1) to obtain

$$\frac{d^2\overline{T}_s(x)}{dx^2}-\frac{s}{\alpha}\overline{T}_s(x)+\frac{1}{k}\overline{g}_s(x)+\frac{T_0}{\alpha}=0 \tag{2.5}$$

and $\overline{g}_s(x)=\int_0^\infty ge^{-st}dt=\mu I_p\overline{\phi}_s e^{-\mu x}$, where $I_p=(1-R)I_0e^{-2r^2/r_0^2}$ (2.6)

So equation (2.5) can be rewritten as

$$\frac{d^2\overline{T}_s(x)}{dx^2}-\frac{s}{\alpha}\overline{T}_s(x)+\frac{\mu}{k}I_p\overline{\phi}_s e^{-\mu x}+\frac{T_0}{\alpha}=0 \tag{2.7}$$

$$\overline{T}_s(x)=C_1Sinh(\sqrt{s/\alpha}\,x)+C_2Cosh(\sqrt{s/\alpha}\,x)+\frac{\mu I_p\overline{\phi}_s e^{-\mu x}}{k(s/\alpha-\mu^2)}+\frac{T_0}{s} \tag{2.8}$$

Laplace transforms of boundary conditions and replace into Eq. (2.8) yield

$$C_1=\frac{\mu^2 I_p\overline{\phi}_s}{k\sqrt{s/\alpha}\,(s/\alpha-\mu^2)} \tag{2.9}$$

$$C_2 = \frac{I_p \bar{\phi}_s \{[A(s/\alpha) + (1-A)\mu^2]e^{-\mu d} - \mu^2 Cosh(\sqrt{s/\alpha} d)\}}{k\sqrt{s/\alpha}(s/\alpha - \mu^2) Sinh(\sqrt{s/\alpha} d)} \quad (2.10)$$

Using inverse Laplace transform,

$$L^{-1}[\frac{T_0}{s}] = T_0 \quad (2.11)$$

$$L^{-1}[\frac{\mu^2 I_p Sinh(\sqrt{s/\alpha} x)}{k\sqrt{s/\alpha}(s/\alpha - \mu^2)}] = \frac{\alpha\mu I_p}{k} Sinh(\mu x) e^{\alpha\mu^2 t} \quad (2.12)$$

$$L^{-1}[\frac{\mu I_p e^{-\mu x}}{k(s/\alpha - \mu^2)}] = \frac{\alpha\mu I_p}{k} e^{-\mu x} e^{\alpha\mu^2 t} \quad (2.13)$$

$$L^{-1}[\frac{\alpha A I_p e^{-\mu d}(s/\alpha) Cosh(\sqrt{s/\alpha} x)}{k\sqrt{s/\alpha}(s - \alpha\mu^2) Sinh(\sqrt{s/\alpha} d)}] = \frac{\alpha A I_p e^{-\mu d}}{k}[\frac{\mu Cosh(\mu x) e^{\alpha\mu^2 t}}{Sinh(\mu d)} + \sum_{-\infty}^{\infty}(-1)^n \frac{2\lambda_n^2}{d(\lambda_n^2 + \mu^2)} Cos(\lambda_n x) e^{-\alpha\lambda_n^2 t}] \quad (2.14)$$

Where $\lambda_n = \frac{n\pi}{d}$ $\qquad n = 0, \pm 1, \pm 2 \Lambda$

$$L^{-1}[\frac{(1-A)\mu^2 I_p e^{-\mu d} Cosh(\sqrt{s/\alpha} x)}{k\sqrt{s/\alpha}(s/\alpha - \mu^2) Sinh(\sqrt{s/\alpha} d)}] = \frac{\alpha(1-A)\mu^2 I_p e^{-\mu d}}{k} \times [-\frac{1}{\mu^2 d} + \frac{Cosh(\mu x) e^{\alpha\mu^2 t}}{\mu Sinh(\mu d)} + \sum_{n=-\infty}^{\infty}(-1)^{n+1} \frac{2Cos(\lambda_n x) e^{-\alpha\lambda_n^2 t}}{d(\lambda_n^2 + \mu^2)}] \quad (2.15)$$

$$L^{-1}[-\frac{\alpha\mu^2 I_p Cosh(\sqrt{s/\alpha} d) Cosh(\sqrt{s/\alpha} x)}{k\sqrt{s/\alpha}(s - \alpha\mu^2) Sinh(\sqrt{s/\alpha} d)}] = -\frac{\alpha\mu^2 I_p}{k} \times [-\frac{1}{\mu^2 d} + \frac{Cosh(\mu d) Cosh(\mu x) e^{\alpha\mu^2 t}}{\mu Sinh(\mu d)} + \sum_{n=-\infty}^{\infty}(-1)^{n+1} \frac{2Cos(\lambda_n d) Cos(\lambda_n x) e^{-\alpha\lambda_n^2 t}}{d(\lambda_n^2 + \mu^2)}] \quad (2.16)$$

$$L^{-1}[\bar{\phi}_s] = \phi(t) \quad (2.17)$$

Using convolution theorem, T(x,t) can be expressed by:

$$T(x,t) = T_0 - \frac{\alpha I_p[1+(1-A)e^{-\mu d}]}{kd}\int_0^t \phi(\tau)d\tau + \frac{\alpha\mu I_p}{k}[Sinh(\mu x) + e^{-\mu x} + \frac{e^{-\mu d} + Cosh(\mu d)}{Sinh(\mu d)}Cosh(\mu x)]$$
$$\times\int_0^t \phi(\tau)e^{\alpha\mu^2(t-\tau)}d\tau + \sum_{n=-\infty}^{\infty}(-1)^n \frac{2\alpha\mu I_p}{kd(\lambda_n{}^2+\mu^2)}[\frac{A}{\mu}e^{-\mu d}\lambda_n{}^2 - (1-A)\mu e^{-\mu d} - \mu Cos(\lambda_n x)]Cos(\lambda_n x)\times$$
$$\int_0^t \phi(\tau)e^{-\alpha\lambda_n{}^2(t-\tau)}d\tau \qquad (2.18)$$

2.2.2 Results and Discussion

Temperature distribution calculated by Eq. (2.18) can be utilized to analysis the effect of different laser parameters such as laser intensity and pulse repetition rate on the laser process, to help understanding the energy transfer process and laser metallization and doping mechanisms.

The properties and parameters of the SiC wafer used in this study are listed in Table 2.1, which are substituted into Eq. (2.18) to calculate the temperature profiles.

Fig. 2.2 shows a transient temperature distribution along the thickness of the wafer for the case of internal heating. The highest temperature is at the bottom surface since most of the laser energy passes through the bulk and is absorbed at the bottom surface. After the optical energy of the laser beam transforms into heat, the thermal energy conducts upward into the bulk. So the temperature decreases continuously from the bottom to the top surface of the wafer as indicated by the right hand side portion of the curve in Fig. 2.2.

Table 2.1 The properties and parameters of the SiC wafer used in this study.

	4H-SiC	6H-SiC
Thermal conductivity k (W/cmK)	3.7	4.9
Thermal diffusivity α (cm^2/s)	1.7	2.2
Absorption coefficient μ (cm^{-1})	6.07	6.07
Reflectance of the top polished surface R (%)	20	20
Absorbance of unpolished surface A (%)	52	51.5
Thickness d (μm)	270	270, 430

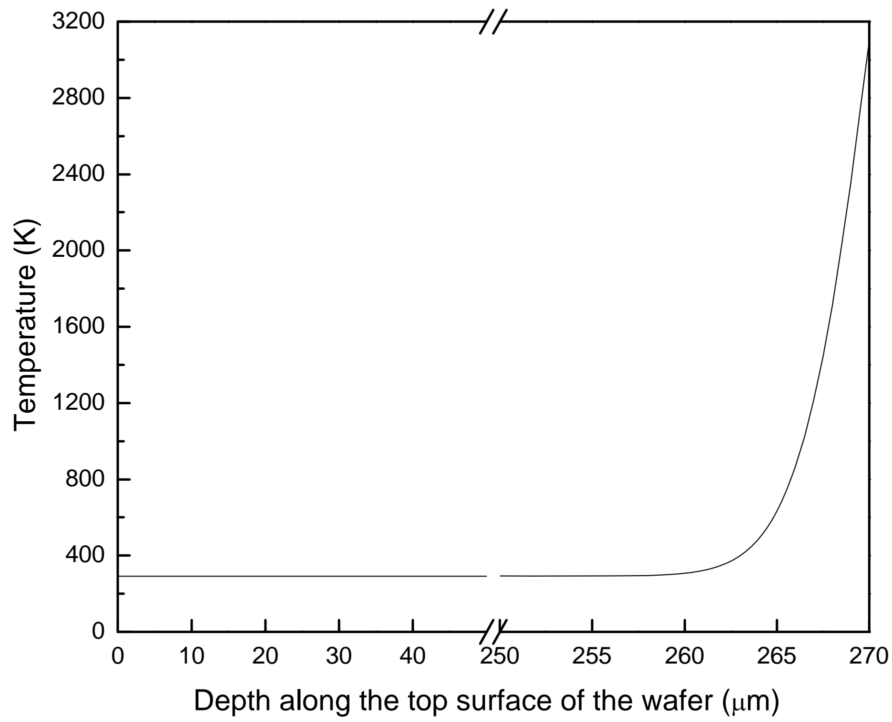

Figure 2.2 Transient temperature distribution along the depth of the substrate (d = 270 μm) at t = 48 ns during Nd:YAG laser irradiation. The laser irradiance = 80.6 MW/cm^2, beam radius = 150 μm, pulse length = 72 ns and pulse repetition rate = 3 kHz.

To realize the laser metallization of the bottom surface, we need to modify the composition of the surface to a carbon-rich phase without affecting the composition of the bulk evidently hence a temperature slightly above the decomposition of silicon carbide (~ 3100 K) is desired.

The temperature rise during the laser irradiation is determined by the laser pulse intensity (I_p) and pulse on time (τ_{on}) of different pulse repetition rate based on Eq. (2.18). The highest bottom surface temperature increases with the intensity of the laser at the same laser pulse on time (Fig. 2.3) and with the pulse on time at the same laser intensity (Fig. 2.4). While the laser intensity and laser pulse on time are related each other by the equation:

$$I_p = \frac{P_0}{f \tau_{on} \pi r_0^{\,2}} \tag{2.19}$$

in which pulse on time increases with the pulse repetition rate for the laser source used in this study. So the laser intensity at particular pulse repetition rate (pulse on time) is determined by the different combination of average power and laser diameter. With the increase of pulse repetition rate (pulse on time), the intensity needed to rise the temperature of the wafer to the decomposition temperature of silicon carbide is decreased, shown in Fig. 2.5. To summarize, the curves shown in Fig. 2.6 indicate the decomposition temperature of SiC that can be reached by the combination of laser intensity and pulse repetition rate (in the range of 2 kHz ~ 35 kHz) for 6H- and 4H- SiC respectively (thickness of the substrate d, 430 μm, is chosen for the calculation).

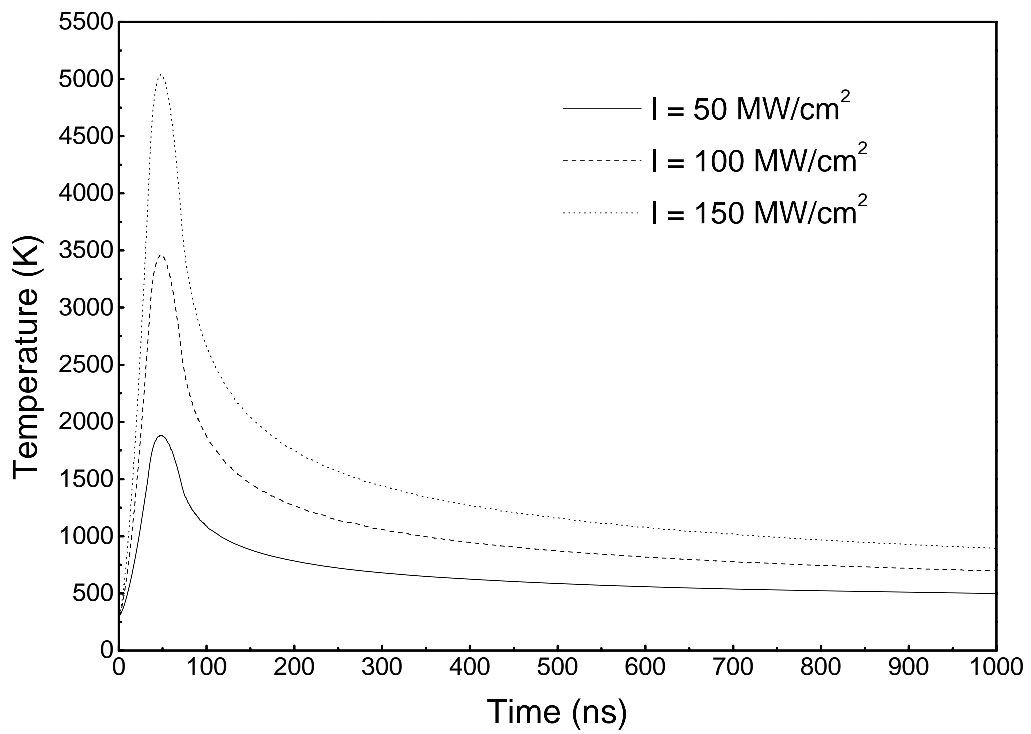

Figure 2.3 Temperature distribution of 6H-SiC wafer (d = 430 μm) irradiated at different laser intensity (I=50, 100 and 150 MW/cm^2) and same pulse repetition rate (f=3 kHz) and accordingly pulse on time (τ_{on}=72 ns).

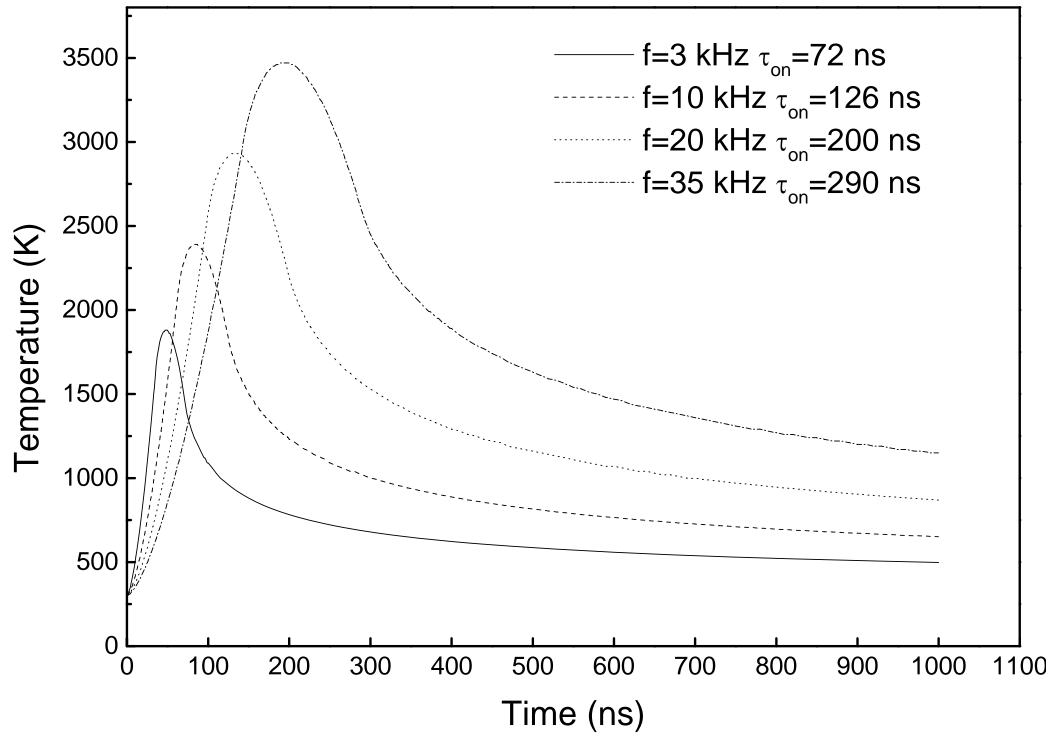

Figure 2.4 Temperature distribution of 6H-SiC wafer (d = 430 μm) irradiated at different pulse repetition rate (f=3, 10, 20 and 35 kHz) and pulse on time (τ_{on} =72, 126, 200 and 290 ns) and same laser intensity (I=50 MW/cm^2).

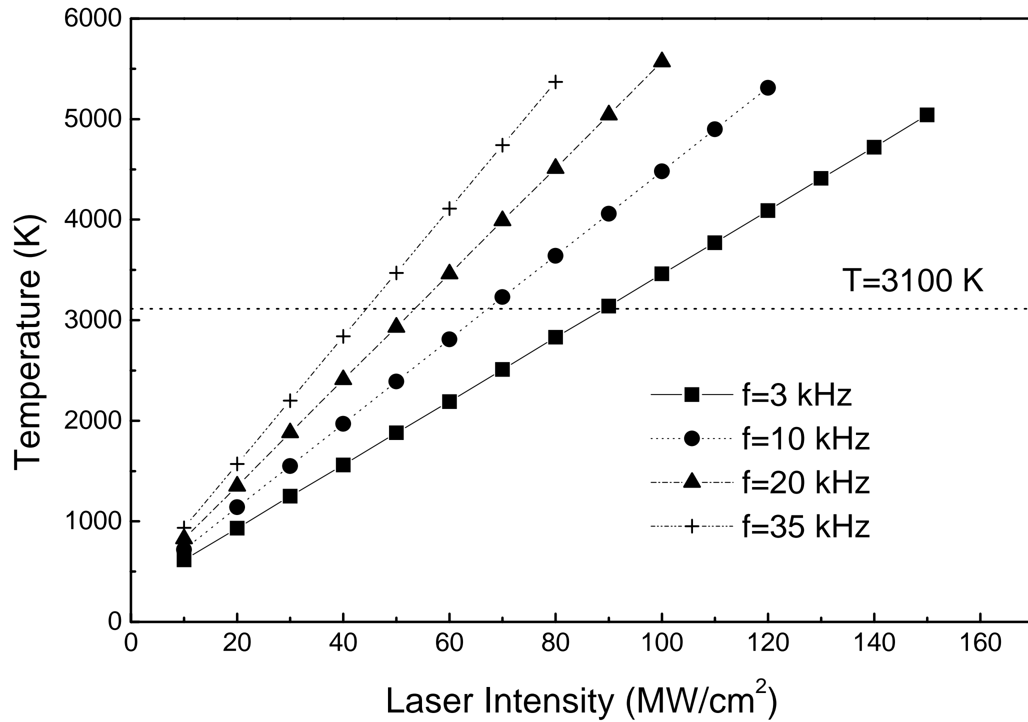

Figure 2.5 Variation of peak temperature with laser intensity at different pulse repetition rate (f=3, 10, 20, 35 kHz) on the 6H-SiC substrate (d = 430 μm).

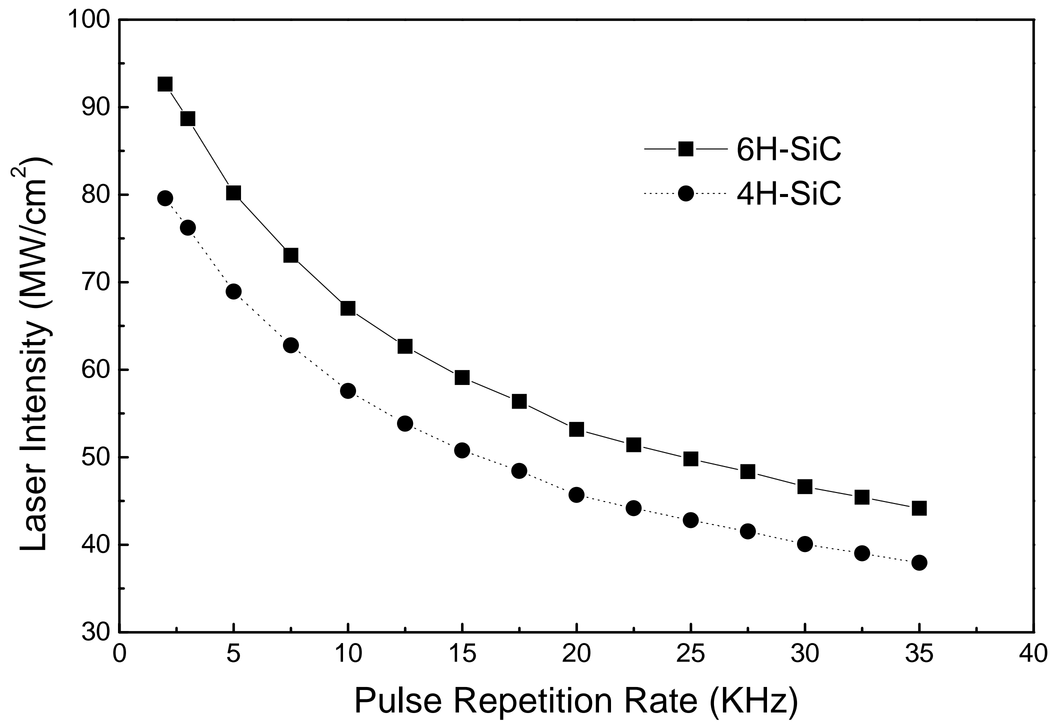

Figure 2.6 Variation of peak temperature for 4H- and 6H-SiC at the combination of laser intensity and pulse repetition rate. The curves indicating the decomposition temperature of SiC, 3100 K.

The same temperature rise can be achieved by all of the pulse repetition rates and higher pulse repetition rate (hence longer pulse on time) induces longer time at high temperatures (shown in Fig. 2.7), which is preferred for the laser doping process since dopant atoms have longer time at high temperatures to diffuse into the deeper bulk lattices. However, another concern is the temperature rise during the multiple laser pulse irradiation. Since the higher pulse repetition rate the shorter pulse off time for the wafer to cool down, the temperature at the end of one single pulse increase with the pulse repetition rate, which can be seen in Fig. 2.7. The temperature at the end of one single pulse, 322 K at 2 kHz of pulse repetition rate, increases to 370 K using the pulse repetition rate 17.5 kHz and to 427 K at 35 kHz of pulse repetition rate. Considering the neglect of heat conduction in the directions perpendicular to the x axis in the model, this temperature can be a little lower and reaches almost room temperature for the repetition rate of 2 kHz. But for higher repetition rates, this temperature rise is still evident even we consider the heat conduction along the directions except the x axis direction. Fig. 2.8 gives the temperature at the end of one single pulse in the whole range of pulse repetition rate (2 kHz ~ 35 kHz) for both 4H- and 6H- SiC, indicating clearly this temperature rises with the pulse repetition rate.

This elevated temperature will increase the whole temperature profile of the following pulse, which is indicated in Figs. (2.9-2.11) where the temperature profiles of three laser pulses at different repetition rate, 3 kHz, (Fig. 2.9), 17.5 kHz, (Fig. 2.10) and 35 kHz (Fig. 2.11) are shown. The peak temperature increases from 3100 K to 3144 K after two more pulses at the repetition rate of 3 kHz. But if we consider the heat conduction along

the directions perpendicular to the x axis, as mentioned above, the temperature at the end of the first pulse is able to reach almost room temperature, which will not affect the peak temperature much. At the repetition rate of 17.5 kHz, the peak temperature increases from 3100 K to 3182 K after two more pulses and this peak temperature rise is more evident, from 3100 K to 3288 K, if 35 kHz of repetition rate is used. Such rapid peak temperature rise will finally damage the wafer during the multiple pulse laser irradiations so low pulse repetition rate is preferred combining all these considerations.

Fig. 2.12 gives the temperature distribution near the bottom region along the thickness of the 6H-SiC at different transient time during one single pulse. After the bottom surface reaches the peak temperature (curve1), heat transferred by the laser energy conducts up in the bulk and increase the bulk temperature accompanying the decrease of surface temperature (curves 2, 3 and 4) with the time. With the increase of distance from the bottom surface the time that temperature reaches its peak value at that particular position extend, shown in Fig. 2.13, such times at positions of bottom surface, 1 μm from the surface, 2 μm from the surface and 3 μm from the surface are 48 ns, 56ns, 64 ns and 72 ns respectively.

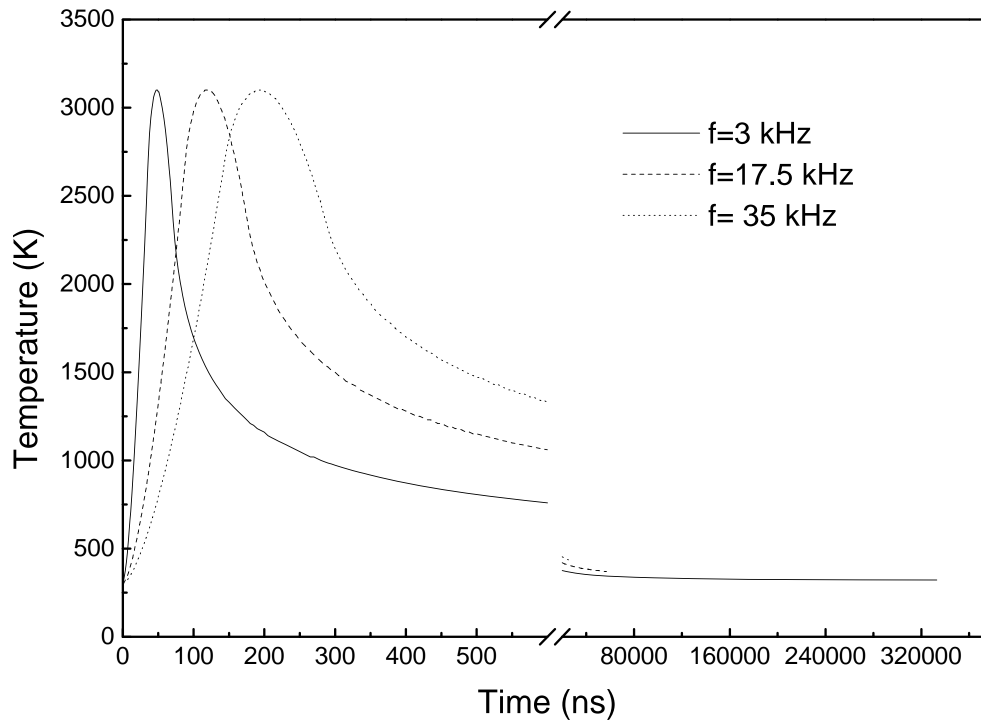

Figure 2.7 Temperature distribution of one single pulse with same peak temperature (3100 K) irradiated at different pulse repetition rate (f=3, 17.5 and 35 kHz) and laser intensity (I=88.7, 56.4 and 44.2 MW/cm^2) on 6H-SiC substrate (d = 430 μm).

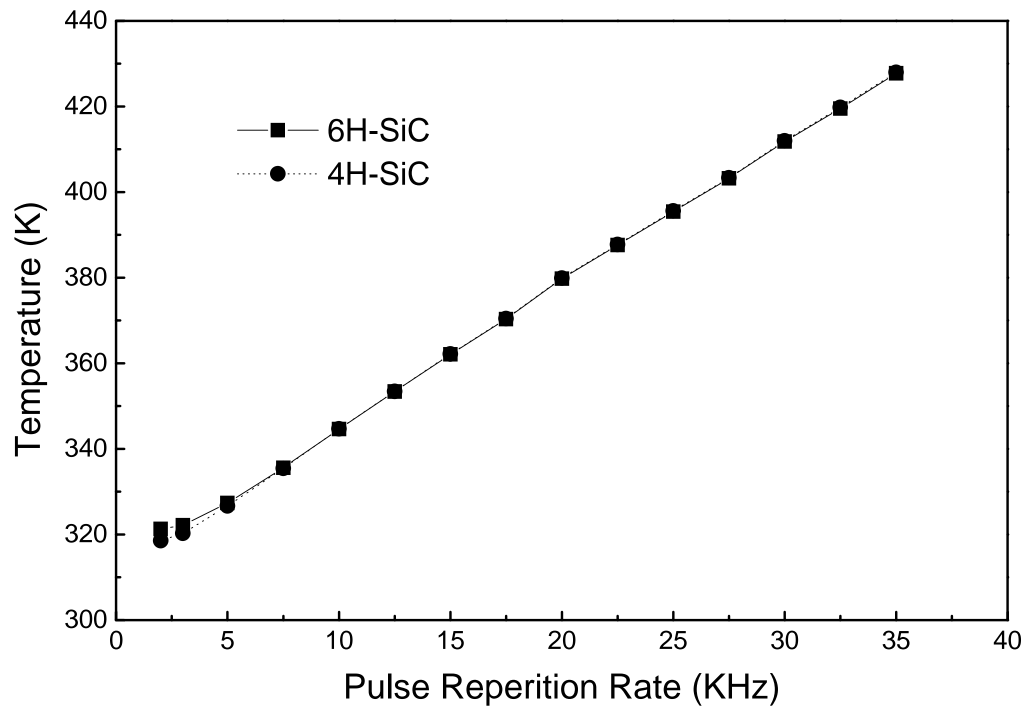

Figure 2.8 Variation of temperature at the end of one single pulse with pulse repetition rate for 4H- and 6H- SiC wafers (d = 430 μm).

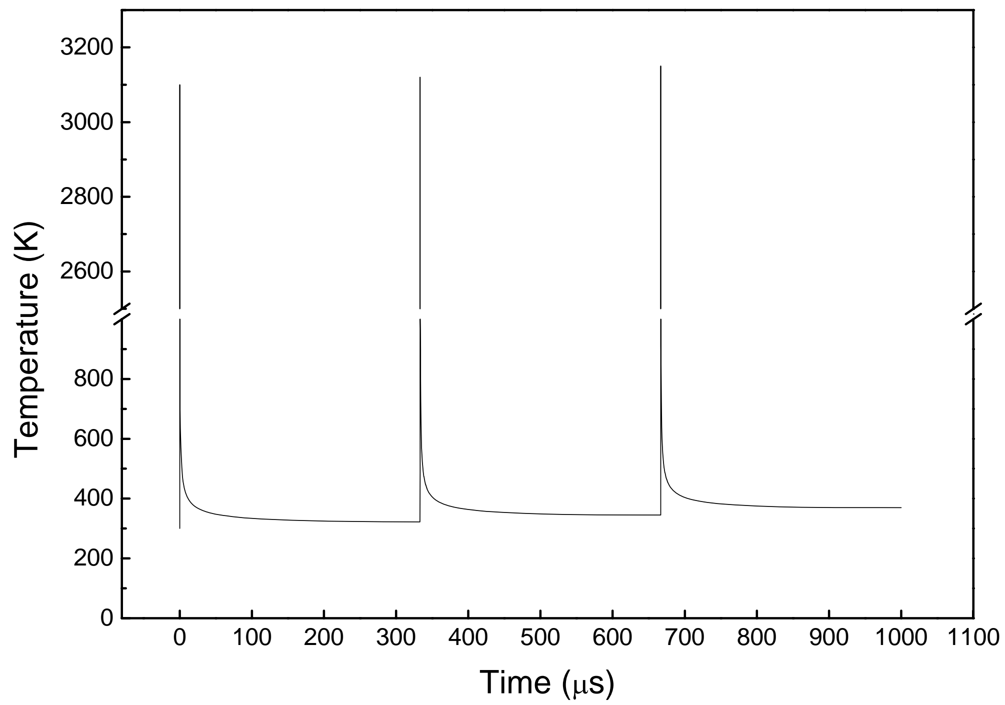

Figure 2.9 Temperature profiles of three pulses of 6H-SiC wafer (d = 430 μm) irradiated at pulse repetition rate of 3 kHz and laser intensity of 88.7 MW/cm^2.

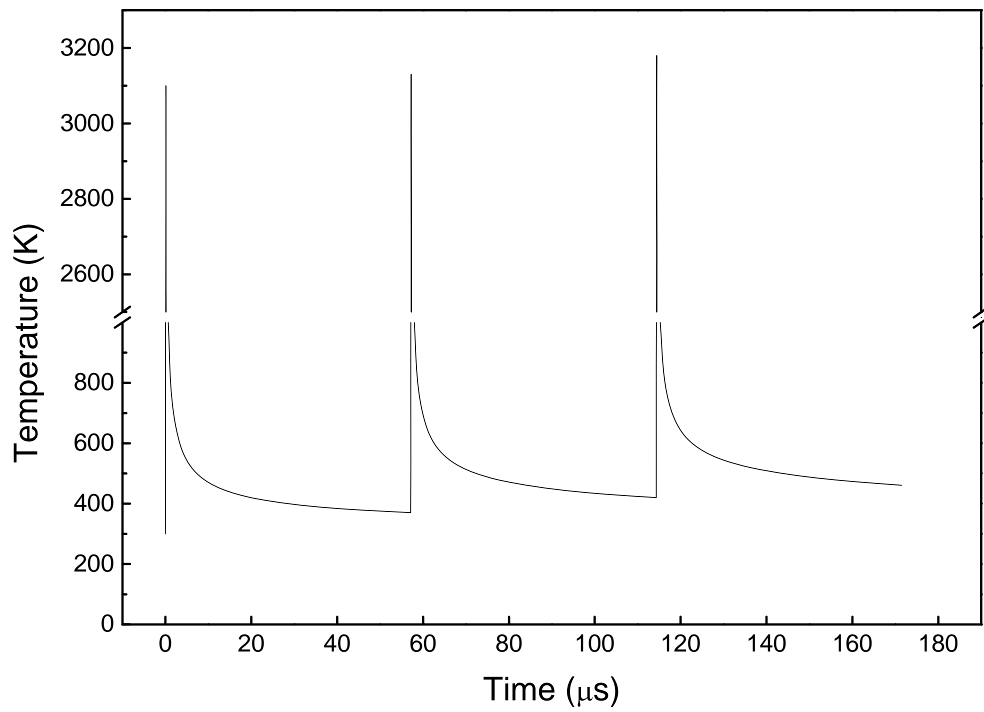

Figure 2.10 Temperature profiles of three pulses of 6H-SiC wafer (d = 430 μm) irradiated at pulse repetition rate of 17.5 kHz and laser intensity of 56.4 MW/cm^2.

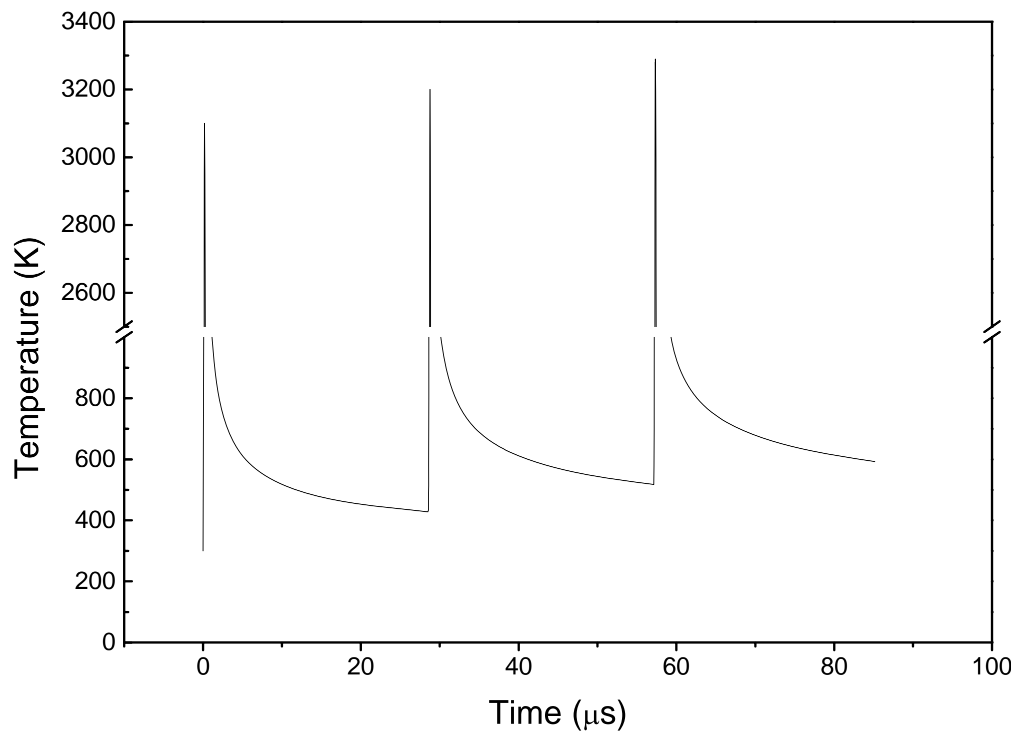

Figure 2.11 Temperature profiles of three pulses of 6H-SiC wafer (d = 430 μm) irradiated at pulse repetition rate of 35 kHz and laser intensity of 44.2 MW/cm^2.

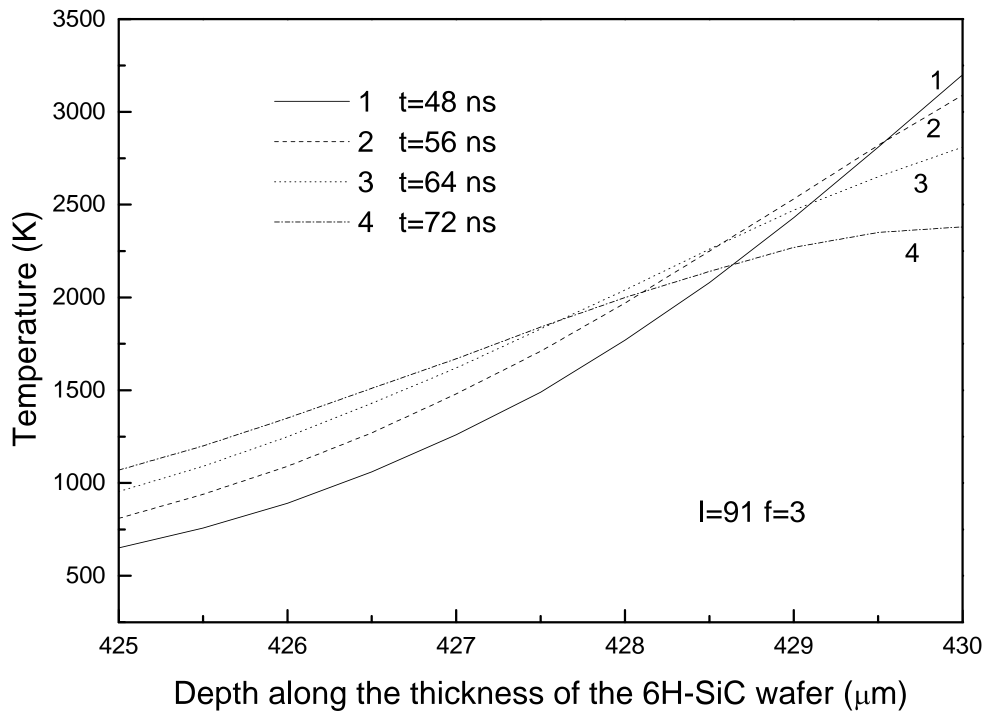

Figure 2.12 Time evolution of temperature along the thickness of the 6H-SiC wafer (d = 430 μm) near the bottom surface region. (Laser intensity: 91 MW/cm^2; Pulse repetition rate: 3 kHz).

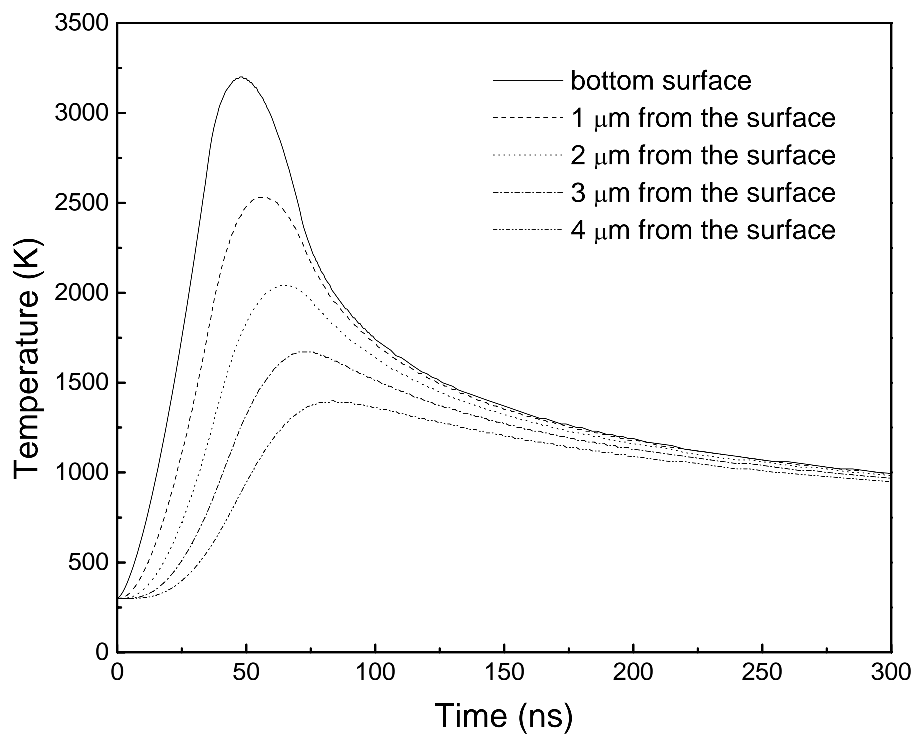

Figure 2.13 Temperature profiles of 6H-SiC (d = 430 μm) at particular position during the laser irradiation. (Laser intensity: 91 MW/cm^2; Pulse repetition rate: 3 kHz).

2.3 Mathematical model and analysis of surface heating

2.3.1 Mathematical Model and Solution

The one-dimensional laser irradiation of surface heating can be described by the following heat conduction equations, boundary conditions and initial condition.

$$\frac{\partial T}{\partial t} = \alpha \frac{\partial T^2}{\alpha x^2} \quad (2.20)$$

$$-k\frac{\partial T}{\partial x} = AI\phi(t) - H(T - T_0) \quad (2.21)$$

$$T(\infty, t) = T_0 \quad (2.22)$$

$$T(x,0) = T_0 \quad (2.23)$$

In this model $\phi(t)$ defines a rectangular shape of laser pulse for excimer laser.

$$\phi(t) = \begin{cases} 1 & nt_p \le t \le nt_p + t_{on} \\ 0 & nt_p < t \le (n+1)t_p \qquad n = 0,1,2\Lambda \end{cases} \quad (2.24)$$

Take Laplace transform of Eq. (2.20) to obtain

$$\overline{T}_s(x,s) = \frac{T_0}{s} + C_1 e^{-\sqrt{s/\alpha x}} + C_2 e^{\sqrt{s/\alpha x}} \quad (2.25)$$

Laplace transform of Eqs. (2.21) and (2.22) and replace into Eq. (2.23) yield

$$C_1 = \frac{AI\overline{\phi}_s}{k\sqrt{s/\alpha} + H} \quad (2.26)$$

$$C_2 = 0 \quad (2.27)$$

By using inverse Laplace transform, we obtain

$$L^{-1}[\frac{e^{-\sqrt{s/\alpha}x}}{k\sqrt{s/\alpha}+H}]=\frac{\sqrt{\alpha}}{k\sqrt{\pi t}}\exp(-\frac{x^2}{4\alpha t})-\frac{\alpha H}{k^2}e^{\frac{Hx}{k}}e^{\frac{\alpha H^2 t}{k^2}}erfc(\frac{H\sqrt{\alpha t}}{k}+\frac{x}{2\sqrt{\alpha t}}) \qquad (2.28)$$

$$L^{-1}[\overline{\phi}_s]=\phi(t) \qquad (2.29)$$

So T(x,t) can be expressed by using convolution theorem,

$$T(x,t)=T_0+\frac{\sqrt{\alpha}AI}{k\sqrt{\pi}}\int_0^t\phi(\tau)\frac{1}{\sqrt{t-\tau}}\exp[-\frac{x^2}{4\alpha(t-\tau)}]d\tau-\frac{\alpha HAI}{k^2}e^{\frac{Hx}{k}}\int_0^t\phi(\tau)e^{\frac{\alpha H^2(t-\tau)}{k^2}}\times$$
$$erfc[\frac{H\sqrt{\alpha(t-\tau)}}{k}+\frac{x}{2\sqrt{\alpha(t-\tau)}}]d\tau \qquad (2.30)$$

2.3.2 Results and discussion

In this case, three different lasing media of excimer laser, XeF with wavelength of 351nm, KrF with wavelength of 248 nm and ArF with wavelength of 193 nm are considered. The absorption of the 4H- and 6H- SiC wafer used in this study at the different wavelengths of excimer laser and their heat transfer coefficients are given in Table 2.2.

Table 2.2 Absorption and heat transfer coefficients of 4H- and 6H-SiC [Levinshtein et al. (2001)].

		4H-SiC	6H-SiC
Absorption (%)	193	62	58
	248	73	71
	351	77	77
Heat transfer coefficient (W/cm^2K)		5	5

The temperature profiles of 6H- and 4H-SiC in a single pulse at three different wavelengths and particular laser pulse intensity are shown in Figs. 2. 14 and 15, respectively. Higher peak temperature can be reached for 4H-SiC than 6H-SiC at same laser intensity for all the three wavelengths because of the lower thermal conductivity and diffusivity of 4H-SiC. For both cases the wafer reaches the highest peak temperature irradiated by the XeF with the wavelength of 351 nm and lowest peak temperature by the ArF with the wavelength of 193 nm. However, high temperature is not the only consideration for the laser doping process. With the decrease of the laser wavelength, the photon energy increases. The higher photon energy the higher energy input efficiency, which is not considered in the temperature distribution modeling. Considering both of the temperature profile and photon energy, KrF excimer laser (λ=248 nm) is preferred because of its much higher photon energy (5 eV) than XeF with wavelength of 351 nm (3.53 eV) and much higher peak temperature (shown in Figs. 2.14 and 2.15) than ArF with wavelength of 193 nm. The time evolution of temperature distribution along the thickness of the 6H-SiC wafer irradiated by KrF laser is shown in Fig. 2.16.

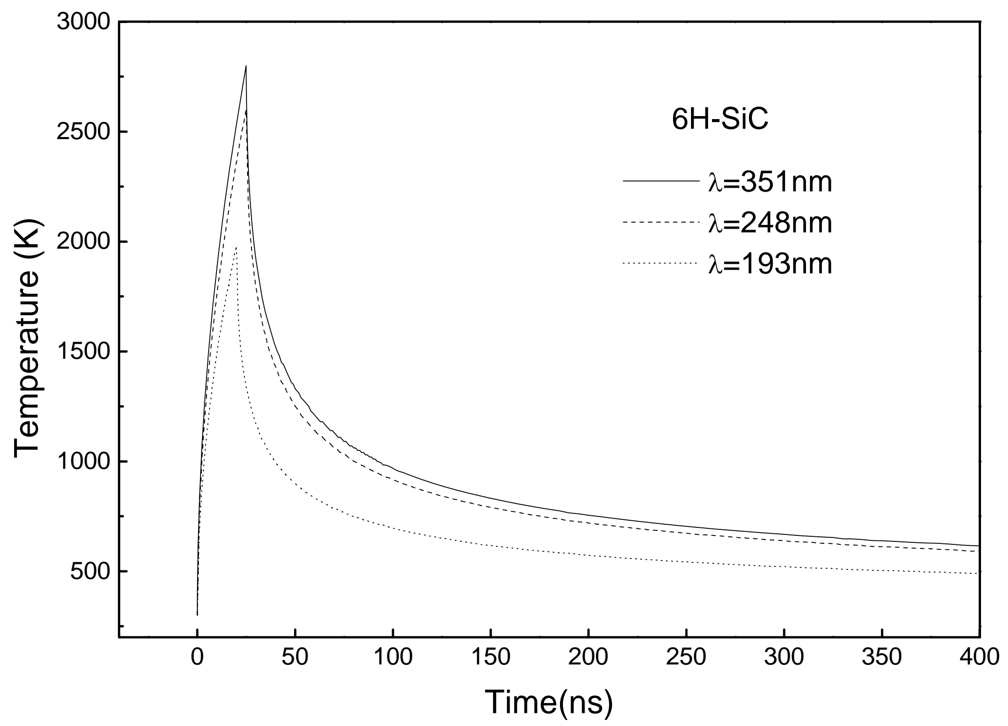

Figure 2.14 Temperature profiles of 6H-SiC irradiated by different excimer laser sources (λ=351, 248 and 193 nm) and same laser intensity (60 MW/cm^2).

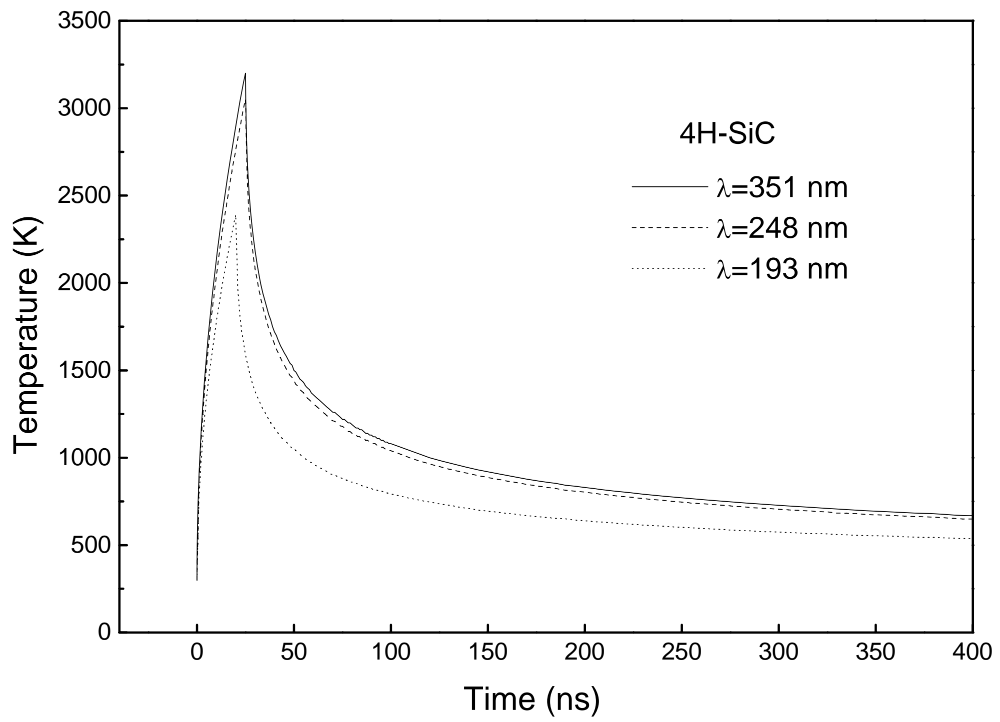

Figure 2.15 Temperature profiles of 4H-SiC irradiated by different excimer laser sources (λ=351, 248 and 193 nm) and same laser intensity (60 MW/cm^2).

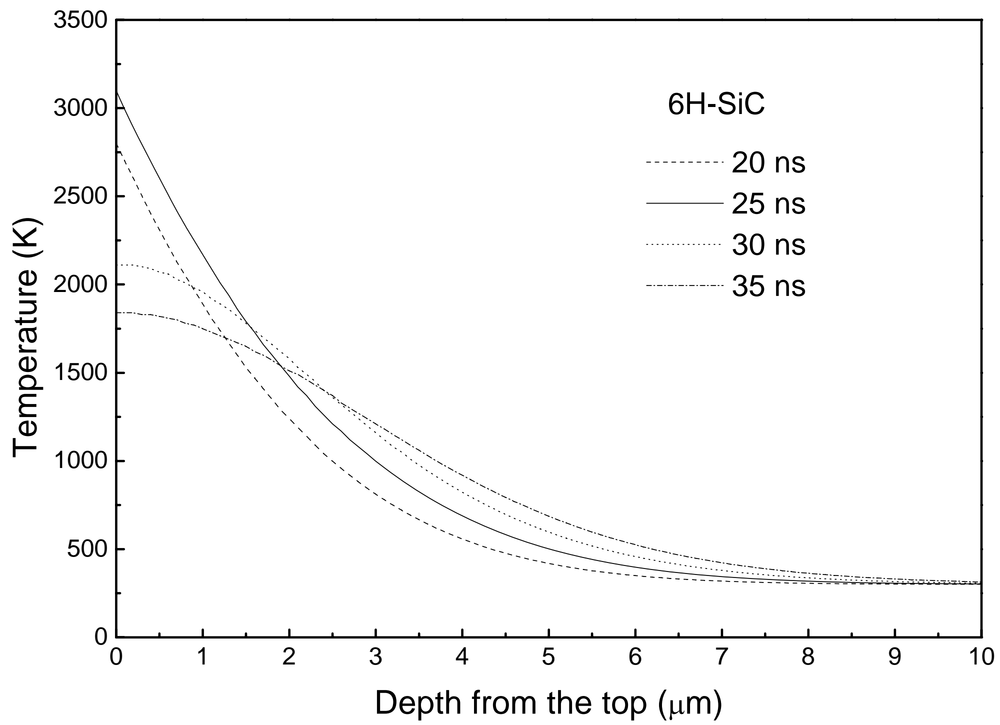

Figure 2.16 Time evolution of temperature along the thickness of the 6H-SiC wafer near the top surface region. (Laser intensity: 73 MW/cm^2; wavelength: 248 nm).

CHAPTER 3: EXPERIMENTAL METHODS AND CHARACTERIZATION TECHNIQUES

3.1 Samples Preparation

Three different silicon carbide samples purchased from II-VI incorporation were used in this study. The corresponding characteristics of the samples are listed in Table 3.1. The average micropipe densities of these wafers are below 12 cm^{-2} and the dislocation densities are about 5.8×10^4 cm^{-2} [Emorhokpor et al. (2004)].

Table 3.1 Silicon carbide samples used in this study.

Sample	Specifications
6H-SiC	Single crystal, n-type doped with the dopant concentration of 5×10^{18} cm^{-3}, 270 μm thick, one side polished
6H-SiC	Single crystal, (0001) Si-face semi-insulating, 430 μm thick, one side polished
4H-SiC	Single crystal, n-type doped with 10 μm epitaxial layer with the dopant concentration of ~10^{16} cm^{-3}, 270 μm thick, epilayer side polished

Prior to laser irradiation experiments, all samples were first washed with soap and deionized (D.I.) water, blow dry nitrogen gas for drying and then cleaned by soaking in H_2O_2:H_2SO_4 solution (1:1 by volume) for 15 minutes. This was followed by rinsing with D.I. water, dipping in buffered oxide etch (BOE), cleaning with actone, methanol and D.I. water, and blowing dry nitrogen gas for final drying.

3.2 Laser Irradiation Experimental Set-up

Experiments can be conducted using two different laser sources: (1) A lamp-pumped Nd:YAG laser (LEE-8150MQ) of wavelength 1064 nm that can be operated in both continuous wave (CW) and Q-switched modes. In the CW mode, the output power of the laser varies from 8 to 200 W. In the Q-switched mode, the pulse repetition rate and pulse on-time can be turned in the range of 2 kHz to 35 kHz and 60 to 300 ns, respectively. The beam profile of the Nd:YAG laser used in this study is shown in Fig. 3.1, in which the laser beam intensity is almost uniform, and that is why we assume uniform laser beam in the calculation of temperature distribution during laser irradiation. (2) A multigas excimer laser (LPX 210i) with three lasing media (ArF for 193 nm wavelength, KrF for 248 nm wavelength and XeF for 351 nm wavelength). The repetition rate is in the range of 1 to 100 Hz and the nominal pulse duration is 20 ns for wavelength of 193nm and 25 ns for wavelengths of 248nm and 351 nm.

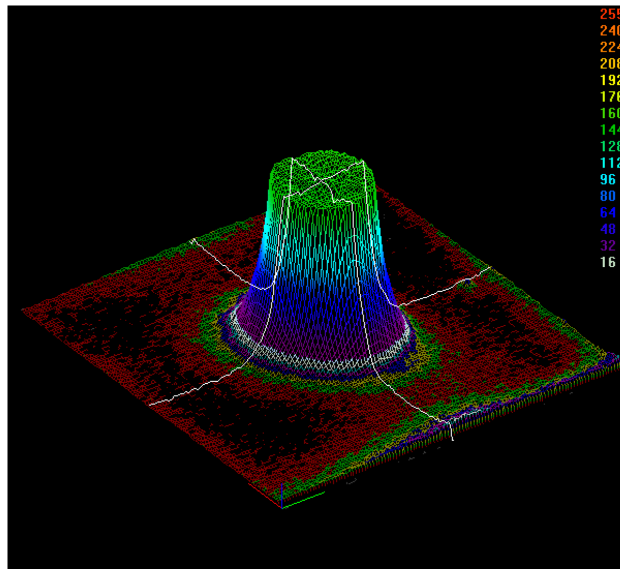

(a)

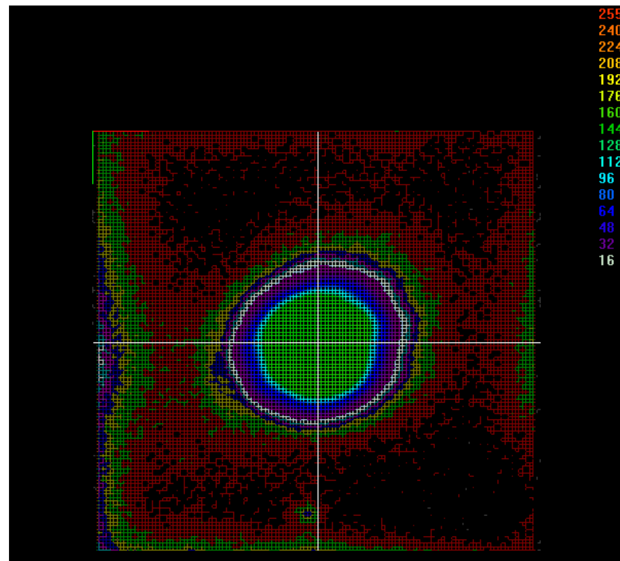

(b)

Figure 3.1 Intensity profile of the incident Nd:YAG laser beam. (a) Front view. (b) Top view.

A schematic of the laser doping, direct metallization and growing endolayer experimental set-up is shown in Fig. 3.2. The sample was placed inside a vacuum chamber where it was simultaneously irradiated with the laser beam and exposed to an appropriate gas, i.e., different gases for different irradiation purposes. The laser beam can focus on the top or bottom surface of the substrate according to different heating mechanisms. The height of the chamber can be controlled through an intermediate stage to obtain different laser spot sizes on the SiC substrate surface. The chamber can be either stationary or moving on a stepper motor-controlled translation stage depending on different experiment requirements. The substrate was kept at room temperature before laser irradiation in all the experiments.

There are three types of ambient gases used in this study:

(i) Dopant containing gas: Highly pure nitrogen gas was used as an n-type dopant source during laser irradiation. Trimethylaluminum [$(CH_3)_3Al$ (TMA)] was used as the p-type precursor for the aluminum doping. TMA was separately heated in a bubbler until it evaporated and then a carrier gas Ar was passed through the bubbler to deliver the TMA vapor to the laser doping chamber through a gas-tight tube. TMA decomposes at the laser-heated substrate surface producing Al atoms, which subsequently diffuse into the substrate.

(ii) Inert gas such as Ar or He serving as the protecting gas during the laser direct metallization process.

(iii) Methane (CH_4): It was used as the carbon source for growing endolayer. Both the pyrolytic and photolytic reactions during excimer laser irradiation process will contribute

to the formation of carbon atoms from methane for the formation of endolayers, which will be illuminated in Chapter 6.

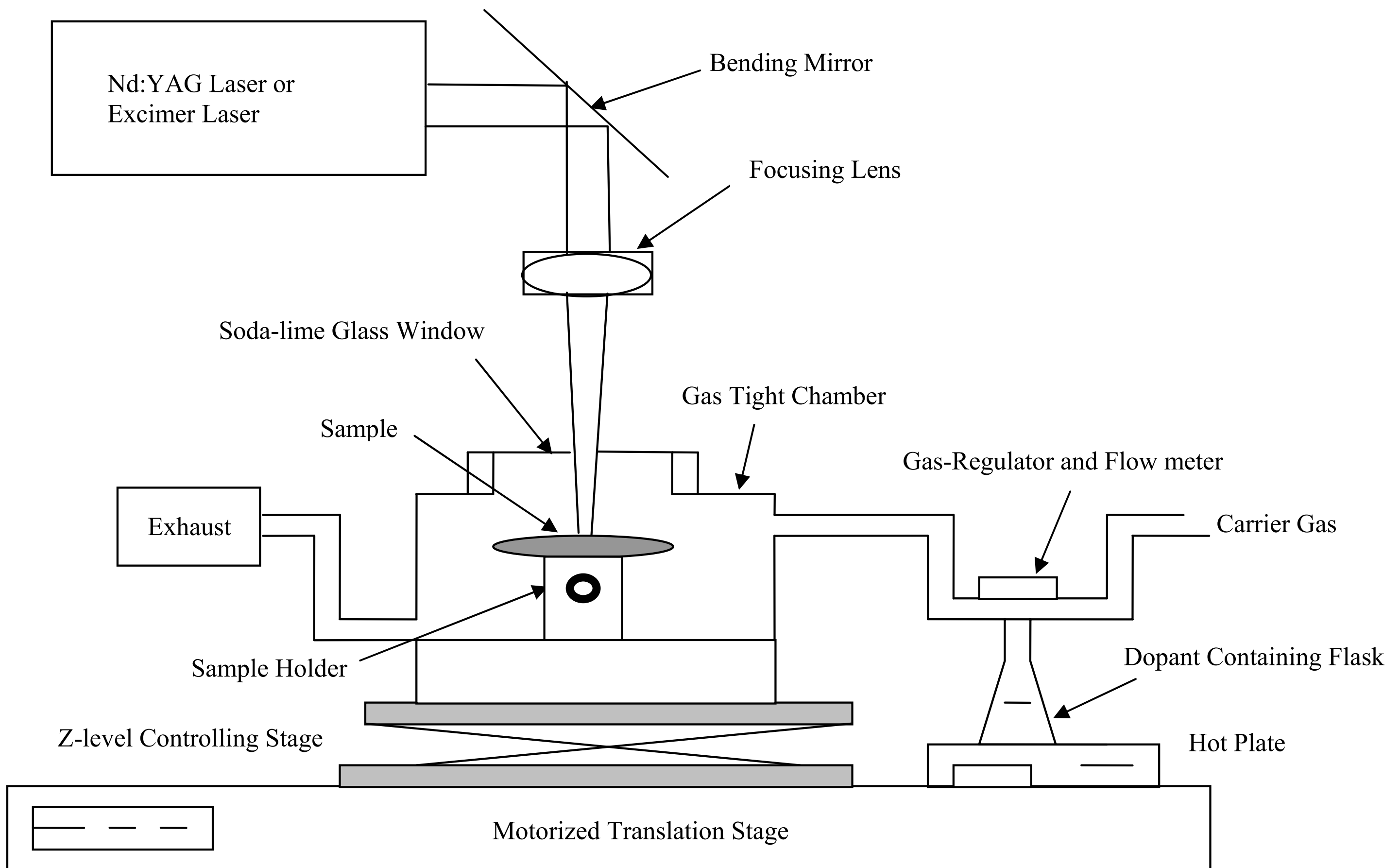

Figure 3.2 Experimental set-up for laser doping, direct metallization and growing endolayer system.

3.3 Materials Characterization

Different analytical techniques were used to quantitatively determine the dopant profiles of both n-type and p-type doped samples, study the crystal structure of the laser irradiated samples and analysis carbon contents in the endolayer.

3.3.1 Secondary Ion Mass Spectroscopy (SIMS)

Cameca IMS-3F SIMS Ion Microscope (Second ion mass spectroscopy) was used to determine the n-type dopant (nitrogen) and p-type dopant (aluminum) depth profiles in the surface region of the substrates after laser doping experiments. The SIMS measurements were performed using Cs and O_2^+ sources with a primary beam of ~ 8 keV. The primary beam current is 1 μA and it was rastered over an area of ~ 200×200 μm of the laser treated wafer. The depth scale was calculated from the sputtering rate and time.

3.3.2 Focused Ion Beam Instrument (FIB)

A FEI 200 TEM Focused Ion Beam (FIB) instrument was used to obtain 10 μm × 5 μm × 150 nm cross-sections of the endolayer sample and parent sample in order to prepare TEM specimens. Platinum film was deposited by Ga^+ ion beam-assisted chemical vapor deposition operating at 30 kV as a protective layer for subsequent FIB milling operation.

3.3.3 Transmission Electron Microscopy (TEM)

To examine the effect of laser processing on the crystalline order of the endolayer, a high resolution transmission electron microscope, FEI Tecnai F30 TEM, operating at 200 keV was used to study the crystal structure along the cross section of the annealed endolayer specimen. The crystal structure along the cross section of the parent wafer was also analyzed for comparison.

3.3.4 X-ray Energy Dispersive Spectrometry (XEDS)

To determine the thickness of the endolayer, carbon contents along the depth of both annealed endolayer specimen and parent wafer were analyzed by line scanning on the cross sections of both annealed endolayer specimen and parent wafer using X-ray energy dispersive spectrometry (XEDS), equipped with FEI Tecnai F30 TEM.

3.3.5 Rutherford Backscattering Spectroscopy (RBS)

Geneal IONIX 1.7MU Tandetron RBS system, involving the channeling of a 1.4 MeV He beam, was used to analyze the lattice disorder of laser induced solid phase diffusion processed specimens by comparing their aligned RBS channeling spectra with that of the parent wafer.

3.4 Electrical Characterization

3.4.1 Current-Voltage (I-V) Characteristics of the Laser Direct Metallized Electrodes

The contact between the substrate and the electrode has a rectifying or ohmic property that can be indicated by different I-V characteristics of the electrodes on the substrate. Current-Voltage measurements between two separated laser direct metallized electrodes on the SiC substrate were performed using a Tektronix 576 curve tracer by contacting the electrodes directly with microprobes.

3.4.2 Resistivity of the Endolayer

The resistivity of the endolayer is calculated using the expression [Edwards, et al. (1997)], $\rho = RA/d$, where A is the area of the top Ni contact, d is the thickness and R is the resistance of the endolayer. To obtain the resistance of the endolayer, I-V characteristics of the endolayer sample and the parent wafer were analyzed. The resistance of the endolayer sample (R) obtained from I-V measurements are the sum of the resistances of the endolayer (R_e), contacts (R_c) and substrate (R_s) [Nadella and Capano (1997)]. Knowing R and the sum of the resistances of the contact and substrate obtained from the parent sample, the resistance of endolayer is obtained. The resistivities of both the as-formed endolayer and annealed endolayer are obtained using this method.

3.4.3 Current-Voltage (I-V) Characteristics of the PIN Diodes

Forward and reverse Current-Voltage (I-V) measurements of laser fabricated PIN diodes on different mediums, including laser fabricated endolayer and as-received homoepilayer, were performed by using a Tektronix 576 curve tracer by contacting the metal deposits or laser direct metallized electrode with microprobes. Breakdown voltage and Forward Voltage drop at 100A/cm^2 of the diodes are indicated from their I-V characteristics.

3.5 Optical Characterization

3.5.1 Laser Beam Characteristics

A laser beam analyzer, Spiricon LBA 300 PC, connected to a pyroelectric camera (Pyrocam I) was utilized to measure the Nd YAG laser beam profile. A highly reflective mirror was put in the optical path between the output laser beam and the camera to avoid the damage of camera detector, whose damage threshold is 4 W/cm^2.

3.5.2 Reflectivity and Transmitivity of Optical Structure at Particular Wavelength

The optical properties (reflectivity and transmission) of the parent 6H-SiC wafer and the laser synthesized embedded structures were calculated based on the transmitted (P_T) and reflected (P_R) powers measured at a laser wavelength of 1064 nm, whose set-up will be illuminated in Chapter 6.

CHAPTER 4: LASER DOPING AND DIRECT METALLIZATION OF SILICON CARBIDE

4.1 Introduction

Lasers have been used to incorporate dopants into semiconductor wafers and such techniques have been classified as laser thermal processing (LTP), gas immersion laser doping (GILD) and laser-induced solid-phase doping (LISPD) as we reviewed in Chapter 1. Lasers also have been utilized in several methods to form ohmic contacts or improve the performance of ohmic contacts to SiC in the literatures. Pulsed laser deposition (PLD) of Ni_2Si on 4H n-type SiC was conducted by excimer laser at room temperature and followed by rapid thermally annealing (RTA) for 30s at 950°C, which resulted in very good ohmic behavior [Cole, M. W. et al. (2001). Pulsed laser doping (PLD) method was used to in-situ dope Ni impurities to form ohmic electrodes in SiC, in which Ni impurities were provided by Ni vapor that continuously evaporated to the SiC substrate using the thermal evaporation source within the vacuum chamber [Eryu et al. (1997)].

Laser dopant incorporations on different semiconductors (SiC and GaN) have been conducted in our group using different doping techniques [Salama (2003)]. However, more work need to be done in this section such as doping mechanisms and effective diffusivity analysis of dopants. This chapter presents experimental results on n-type and p-type laser doping of different SiC polytypes using different laser sources and laser

doping methods and the discussion of the laser doping mechanisms and effective diffusivity of the dopants.

Laser direct metallization on n-type SiC based on the laser direct write technique in our group has been illuminated in the previous work, in which laser induced conversion of electric resistivity, surface analysis of the laser metallized SiC, Schottky barrier height calculation of laser fabricated rectifying contacts and specific contact resistance calculation of laser fabricated ohmic contacts were discussed [Salama (2003)]. This method relies on the ability of laser to locally change the stoichiometry of the SiC in the laser-treated region through the photonic and thermal energy coupling between the beam and the material by transforming SiC surface into either Si-rich (excimer laser irradiation) or C-rich phases (Nd:YAG laser irradiation) [Salama (2003)]. In this chapter this method was extended by combining the laser direct metallization with the laser doping to improve the performance of the contact, i.e., fabrication of laser direct metallized contact on heavily laser doped SiC substrate.

4.2 Laser Doping Process of Silicon Carbide

Two different methods, illuminated in section 2.1, are used to dope silicon carbide. The laser irradiation parameters are listed in Table 4.1. For internal heating method, in which Nd:YAG laser with the wavelength of 1064 nm is used, low pulse repetition rates (3 kHz) are chosen because of the consideration of temperature rise during the multiple pulse

laser irradiation. For surface heating method, KrF excimer laser with the wavelength of 248 nm rather than ArF excimer laser (λ = 193 nm) and XeF excimer laser (λ= 351 nm) is chosen because of the high absorption of silicon carbide with respect of the wavelength of 248 nm and the high photo energy of the laser light with 248 nm wavelength.

Fig. 4.1 shows the temperature distribution of 6H-SiC during n-type doping using the parameters of laser internal heating listed in Table 4.1. The peak temperature of the bottom surface, where is the location of highest temperature during the laser irradiation shown in Fig. 2.2, is below the decomposition temperature of silicon carbide (Fig. 4.1a). That means the wafer does not melt during the laser doping process. This will allow fabrication of electronic devices using the doped sample. The transient temperature distribution along the thickness of the wafer from the bottom surface at the peak temperature (t=48ns) (Fig. 4.1b) shows the non-uniformly temperature distribution decreasing along the substrate thickness from the bottom surface.

Table 4.1 Processing parameters for different laser doping methods.

Methods	Internal Heating		Surface Heating
Sample	n-type 6H-SiC	n-type 6H-SiC	n-type 4H-SiC with epilayer
Doped region	n-type	p-type	p-type
Laser source	Nd:YAG	Nd:YAG	KrF excimer
Wavelength (nm)	1064	1064	248
Pulse repetition rate (Hz)	3000	3000	1
Beam area (cm^2)	$\pi(0.03)^2/4$	$\pi(0.03)^2/4$	0.2×0.4
Pulse energy (mJ)	4	4.33	120
Laser fluence (J/cm^2)	5.65	6.1	1.5
Pulse intensity (MW/cm^2)	78.6	85.1	60
Scanning speed (mm/s)	1	1	-
Irradiation passes	1	1	-
Laser shots	-	-	1000, 3000
Ambient gas	N_2 at 30 psi	TMA delivered by Ar at 30 psi	TMA delivered by Ar at 30 psi

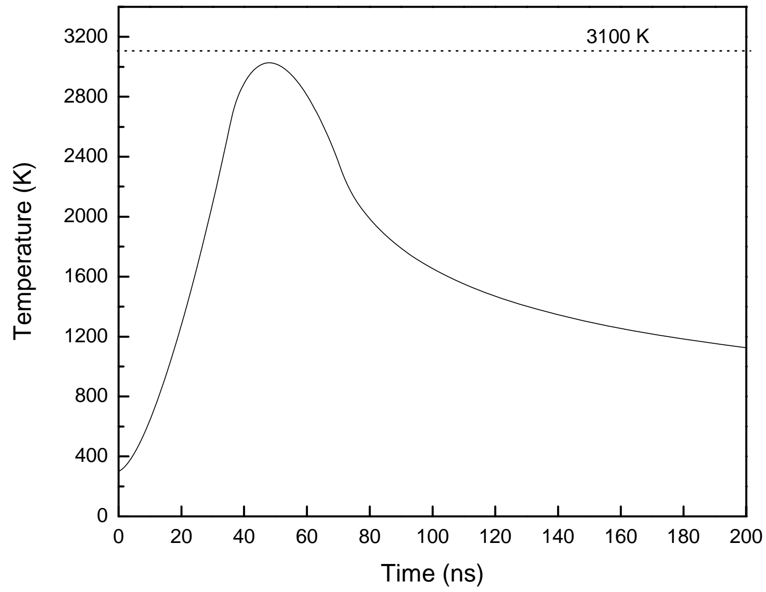

(a)

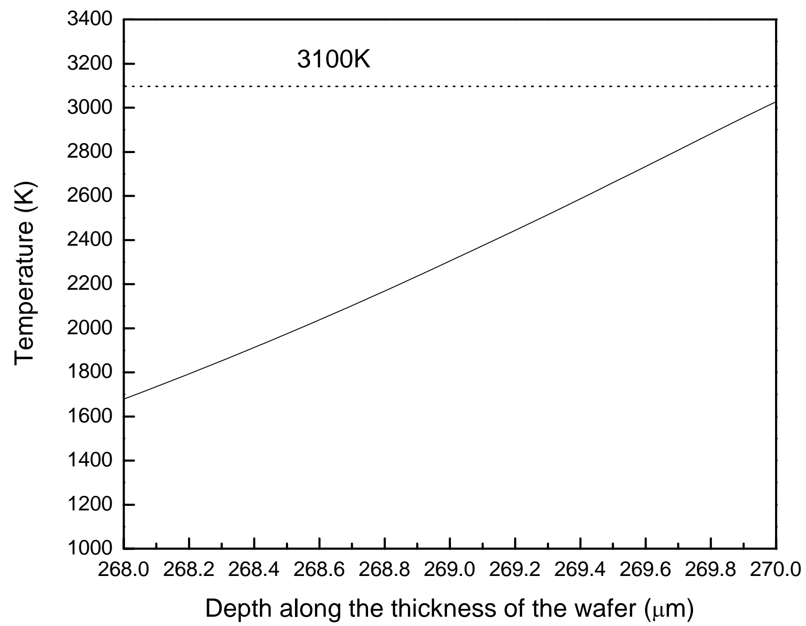

(b)

Figure 4.1 Temperature distribution of 6H-SiC during n-type doping using the parameters of method A listed in Table 4.1.(a) Bottom surface temperature distribution with the time; (b) Transient temperature distribution along the thickness of the wafer from the bottom surface at the peak temperature (t=48ns).

Fig. 4.2 shows the temperature distribution of 6H-SiC during p-type doping using the internal heating method listed in Table 4.1. Different from n-type doping in which the absorption of laser energy by the dopant, nitrogen gas, is negligible, during p-type doping, certain amount of laser energy will be absorbed by the chamber window because of the deposition of aluminum on it and the high concentration dopant, trimethyaluminum (TMA) itself. The amount of laser energy absorbed by the window and dopant depends on the dopant concentration, wavelength of the laser, laser beam area, and the distance laser light passing through in the dopant ambient. In this case the loss of laser energy about 10% is estimated and hence the peak temperature is around 3000 K. Such estimation is based on the experiment phenomenon that decomposition of silicon carbide is observed if the pulse energy is increased from 4.33 mJ to 4.6 mJ, which corresponds to peak temperature slightly above peritectic temperature (3125 K) when considering 10% loss of laser energy by the medium. The transient temperature distribution along the thickness of the wafer from the bottom surface at the peak temperature (t=48ns) (Fig. 4.2b) also shows the non-uniformly temperature distribution decreasing along the substrate thickness from the bottom surface.

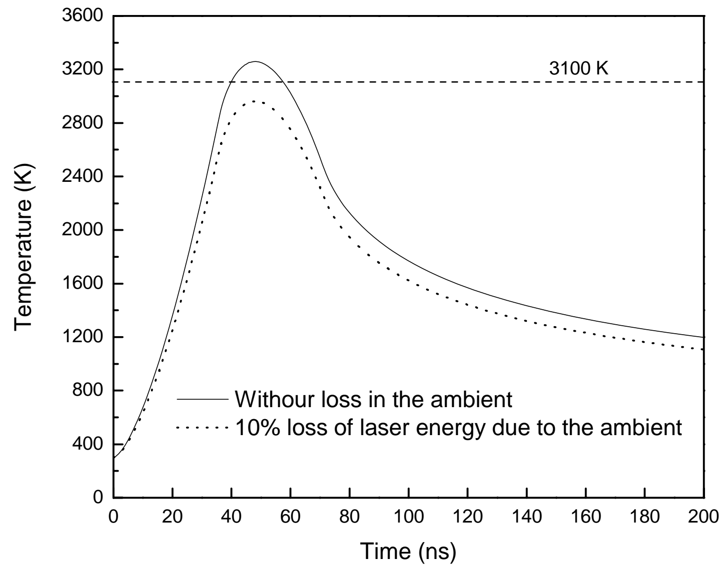

(a)

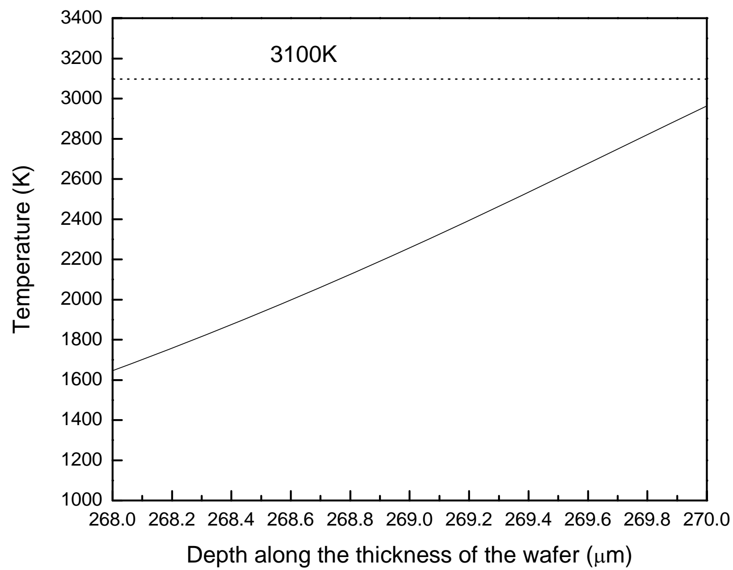

(b)

Figure 4.2 Temperature distribution of 6H-SiC during p-type doping using the parameters of method A listed in Table 4.1.(a) Bottom surface temperature distribution with the time; (b) Transient temperature distribution along the thickness of the wafer from the bottom surface at the peak temperature (t=48ns).

The temperature distribution of 4H-SiC during p-type doping using the parameters of surface heating listed in Table 4.1 is shown in Fig.4.3. The loss of laser energy is estimated as about 5% considering the lower Trimethylaluminum concentration filled in the chamber compared to the former case and the experimental observation that the wafer was decomposed by increasing the pulse energy from 120 mJ to 130 mJ, which corresponds to peak temperature slightly above peritectic temperature (3130K) when considering 5% loss of laser energy by the medium. The transient temperature distribution along the thickness of the wafer from the top surface at the peak temperature (t=25ns) (Fig. 4.3b) shows the non-uniformly temperature distribution decreasing along the substrate thickness from the top surface.

The temperature profile in Fig. 4.3a is much narrower than in Figs. 4.1a and 4.2a. This indicates that the sample remains at high temperature for much shorter time during excimer laser irradiation than during Nd:YAG laser irradiation at similar peak temperature. Therefore the dopant atoms will have much shorter time to diffuse into the substrate during excimer laser doping than during Nd:YAG laser doping.

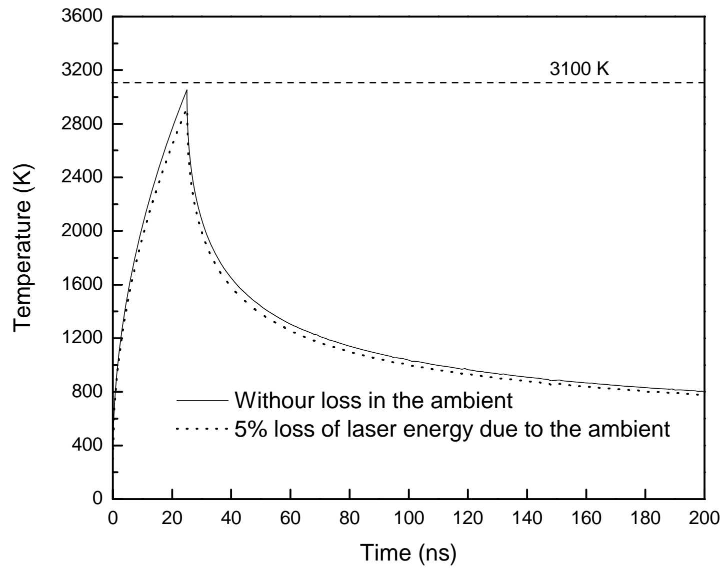

(a)

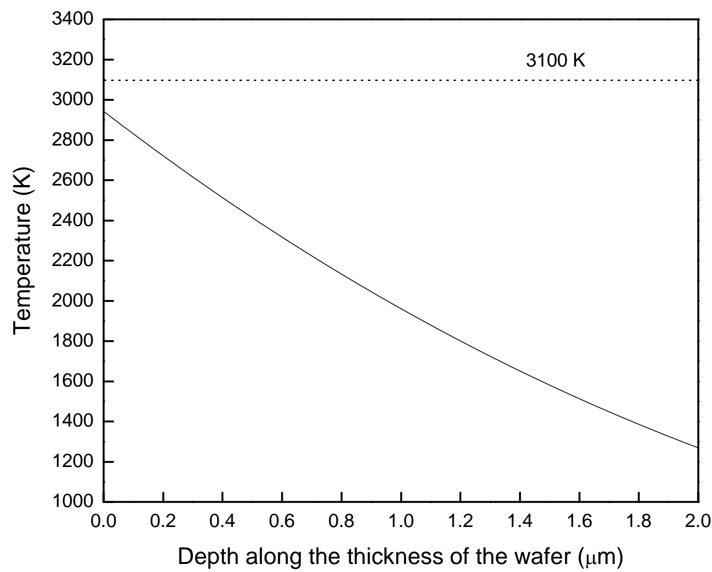

(b)

Figure 4.3 Temperature distribution of 4H-SiC during p-type doping using the parameters of method C listed in Table 4.1.(a) Top surface temperature distribution with the time; (b) Transient temperature distribution along the thickness of the wafer from the top surface at the peak temperature (t=25ns).

4.3 Doping profiles

Dopant depth profiles of laser doped wafers were obtained using secondary ion mass spectroscopy (SIMS). Before the SIMS measurements aluminum surface residue was removed by immersing the sample in a KOH solution for several minutes. KOH attacks aluminum aggressively but etches SiC very slowly. Then the sample was rinsed with D. I. water and blown nitrogen gas for drying.

4.3.1 Doping Profiles Obtained by Laser Internal Heating

Fig. 4.4 shows n-type nitrogen dopant concentration along the depth of 6H-SiC wafer, which was obtained by the Nd:YAG laser doping process. The results indicate that the nitrogen concentration at the wafer surface, approximately 1×10^{21} cm^{-3}, drops to the background nitrogen concentration of about 1.5×10^{19} cm^{-3} within a depth of approximately 800 nm. It should be noted that the surface concentration of nitrogen (1×10^{21} cm^{-3}) exceeds its maximum solubility limit in 6H-SiC (6×10^{20} cm^{-3} [Schöner (2002)]), which can be explained by the non-equilibrium process of laser doping in silicon carbide because of high cooling rate due to the excellent thermal conductivity of silicon carbide. Fig. 4.5 shows the p-type aluminum dopant concentration along the depth of 6H-SiC wafer, obtained using the same Nd:YAG laser doping process as for nitrogen doping. The aluminum concentration at the wafer surface is approximately 5×10^{20} cm^{-3}, which drops to about 1.5×10^{18} cm^{-3}, the background of aluminum in the near surface region, at a depth of about 800 nm.

The neat dopant concentration profiles of nitrogen and aluminum after removing the background concentration are compared in Fig. 4.6. The two profiles show similar decreasing curves, indicating their similar diffusion mechanisms. In both of the profiles there are two diffusion regions can be identified according to the evident change of the profile slopes. The first region is located near the surface, within the depth of approximately 200 nm for nitrogen and about 100 nm for aluminum, corresponding to the fast decrease of the dopant concentration (large curve slope) in the whole profiles. In this region the slope of the aluminum dopant profile is larger than that of nitrogen, indicating that aluminum atoms diffuse slower than that of nitrogen. The rest part of the profiles can be considered as the second diffusion region, with the characteristic of relatively smaller curve slope compared with the first region. The change of the curve slope indicates the change of the diffusion mechanisms.

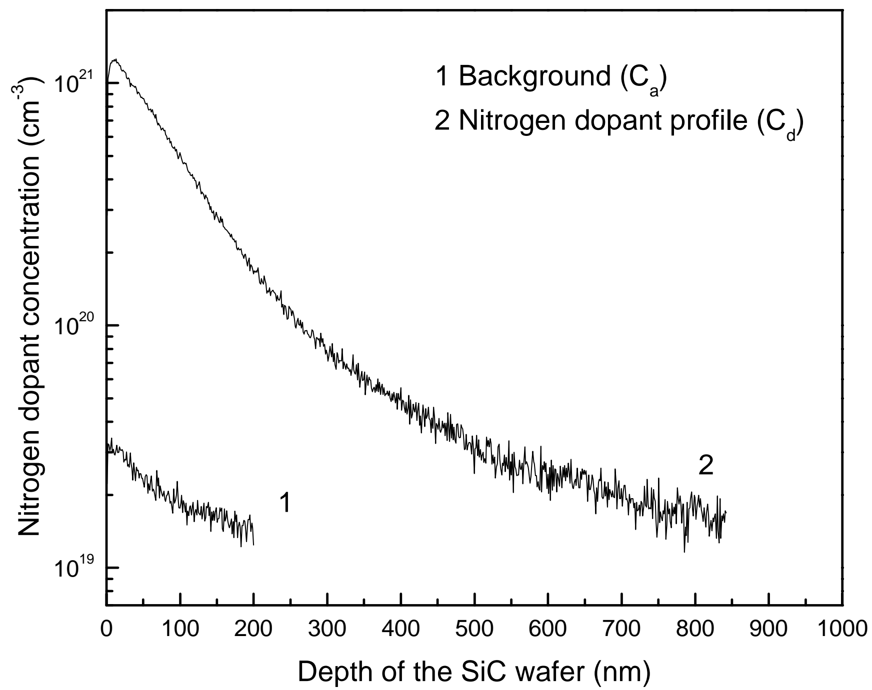

Figure 4.4 Nitrogen dopant profiles obtained with a Nd:YAG laser. C_a: Concentration of nitrogen in the as-received wafer; C_d: Concentration of nitrogen in the doped wafer.

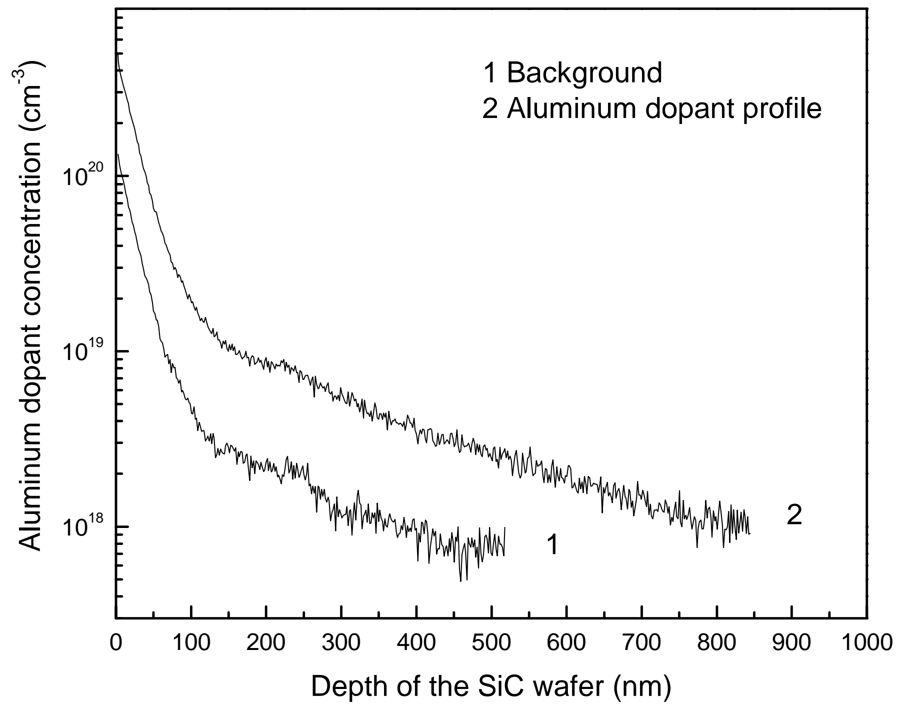

Figure 4.5 Concentration depth profiles of aluminum doped by LISPD method measured with SIMS.

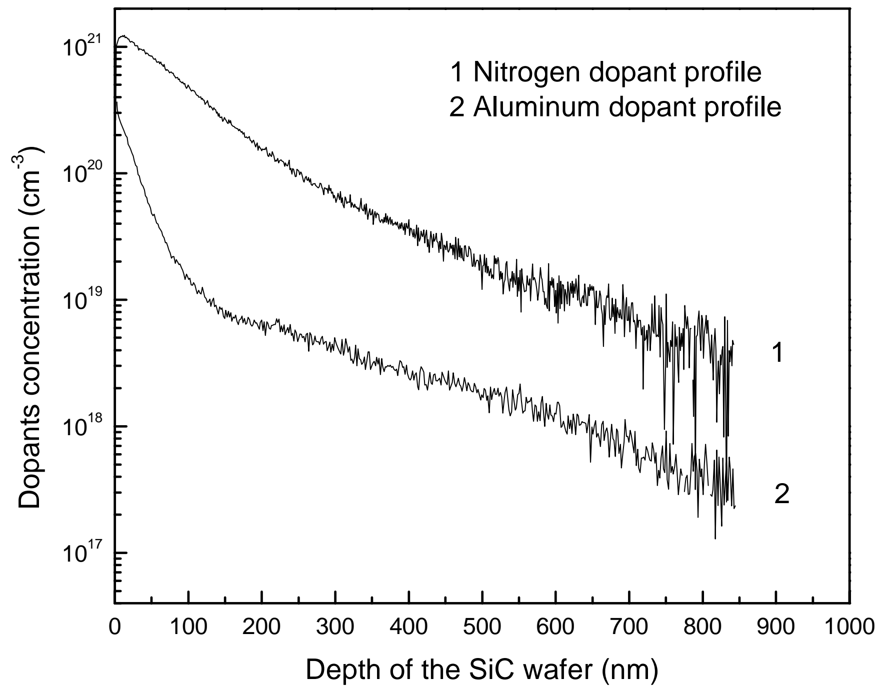

Figure 4.6 Comparison of concentration of Al and N_2 dopants along the depth of 6H-SiC wafer using similar laser doping parameters.

4.3.2 Doping profiles obtained by Laser Surface Heating

Fig. 4.7 shows aluminum dopant concentration distribution, which was obtained with the KrF excimer laser doping process. The substrate was doped to a depth of 200 nm with maximum dopant concentration 2×10^{22} atoms/cm^3 using 1000 laser pulses in the doping experiment. 3000 laser pulses drove the dopant to a depth of about 450 nm. The junction depth of 200 nm obtained here is much higher than that in the ref [Eryu et. Al (1995)] where 50 nm junction depth was obtained on 6H-SiC using same parameters by KrF excimer laser with the wavelength of 248 nm. The changes in the slopes of the concentration profiles at the depth of about 120 -150 nm indicate fast and slow diffusion processes in the near-surface and far-surface regions respectively.

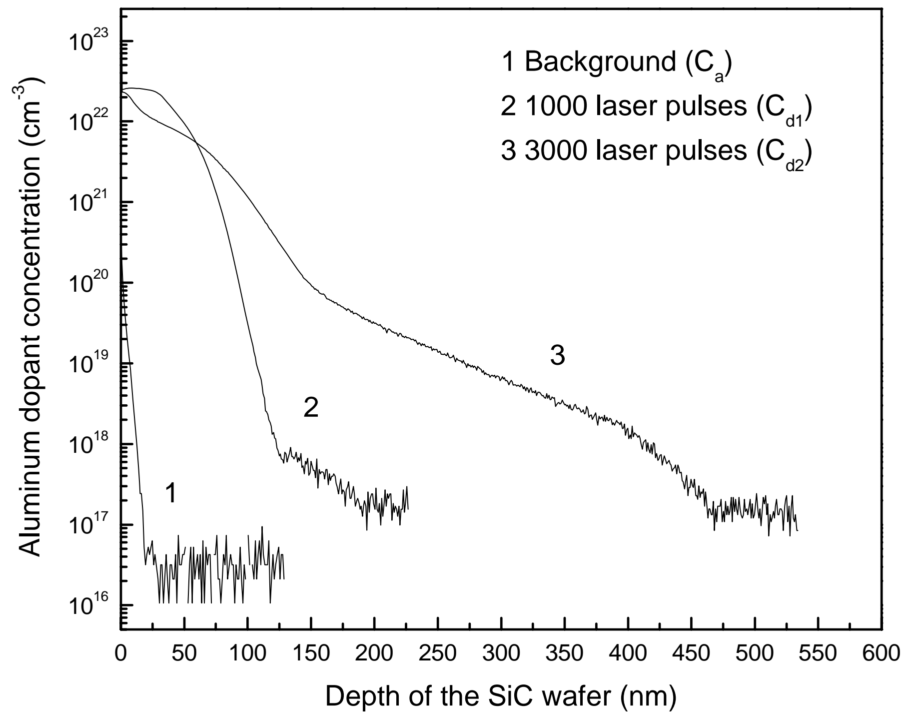

Figure 4.7 Aluminum dopant profiles obtained with an excimer laser. C_a: Concentration of aluminum in the as-received wafer; C_{d1}: Concentration of aluminum in the 1000 laser pulses doped wafer; C_{d2}: Concentration of aluminum in the 3000 laser pulses doped wafer.

4.4 Mechanisms of Laser Doping Process

The dopant atoms pass through a non-uniformly heated region with a maximum temperature at the surface region and decreasing along the substrate thickness. This lowers the thermal energy of the diffusing atoms as they travel along the substrate thickness and therefore their diffusion is controlled by the less energetic processes such as interstitial diffusion. The diffusion coefficient is generally given by

$$D = D_0 \exp\left[-Q/(k_B T)\right] \tag{4.1}$$

where D_0 is the mass diffusivity, Q activation energy, k_B Boltzmann constant and T the absolute temperature of the substrate. $Q/(k_B T)$ represents the ratio of the activation energy of the diffusion process to the thermal energy ($k_B T$) at a given temperature. For symmetric lattice structures, interstitial diffusion has lower activation energy (Q=0.5-1.5 eV) than substitutional diffusion (Q = 3-5 eV) [Pankove (1999)] since no energy is required to form a vacancy in interstitial diffusion. So the dopant atoms possessing higher thermal energy near the wafer surface have the ability to diffuse by more than one mechanism, such as substitutional and interstitial mechanisms, simultaneously. As the diffusion depth increases, the diffusion mechanism changes depending on the specifics of the laser-induced temperature field and the diffusivity is expected to decrease [Salama (2003)].

The diffusion of dopant atoms into the bulk silicon carbide can be explained by considering the laser-enhanced substitutional and interstitial diffusion mechanisms. Laser-induced heating and stresses can generate defects such as vacancies, which are

normally localized near the solid surface. The concentration of vacancies can be very high in semiconductors up to 10^{19} or 10^{20} cm^{-3} near their melting temperature. The vacancy concentration can be much higher than their equilibrium values due to thermal diffusion, stress effects related to thermal expansion, laser-induced shock waves and electronic or vibrational excitations [Bäuerle (2000)]. So in the near-surface region, the dopant atoms can easily diffuse into the bulk by occupying these vacancies as well as interstitial sites because of the low activation energy for interstitial diffusion. The site occupancy can be analyzed by using the following relationships because it has been found that Al preferentially occupies Si vacancy sites [Gadiyak (1998)] and N preferentially occupies C vacancy sites in SiC:

$$N_i + V_C = N_C \quad (4.2)$$

$$Al_i + V_{Si} = Al_{Si} \quad (4.3)$$

where N_i and Al_i represent the nitrogen and aluminum atoms at the interstitial sites respectively, V_C and V_{Si} denote carbon and silicon vacancies respectively, N_C represents nitrogen occupying the lattice site of carbon, and Al_{Si} represents aluminum occupying the lattice site of silicon. The substitutional impurities, however, have a low probability of diffusing substitutionally, while the interstitial impurities have a much higher diffusion coefficient since they are less strongly bound to the lattice. The diffusion process is then dominated by the highly mobile interstitials [Schubert (1993)] in the far-surface region.

4.5 Effective Diffusivity Analysis

Usually the diffusivities of dopants, such as aluminum, in silicon carbide are very low both from vapor source and ion implantation because of the chemical inertness and densely packed atomic structure of silicon carbide. The diffusion coefficient of aluminum in SiC is 2×10^{-15} cm^2/s at a temperature of 1700°C [Usov (1999a)] and 3×10^{-14} - 6×10^{-12} cm^2/s at temperatures higher than 2500°C from typical vapor sources [Schöner (2002)], and 2.7×10^{-14} cm^2/s during 1800°C annealing after ion implantation at room temperature [Tajima (1982)]. It has been reported that the diffusion of aluminum can be enhanced in silicon carbide during ion implantation at high temperatures [Suvorov (1996), Usov (1999a) and Usov (1999b)]. Usov et al [1999a] implanted aluminum into 6H-SiC wafers at 1700°C, showing the widening of the dopant concentration profile in the near-surface region and the anomalous deep penetration tail compared with the Gaussian distribution of the aluminum profiles of the sample implanted at room temperature. They reported diffusivities in the range of 1.5×10^{-12}- 2×10^{-14} cm^2/s and 5×10^{-11}- 2×10^{-12} cm^2/s in the near-surface and far-surface regions respectively, and the diffusivities in both regions decrease with the increase in the implantation time. Their data also shows that the diffusivity is lower in the near-surface region than in the far-surface region.

The driving forces for the diffusion of dopants in silicon carbide differ between the laser doping and high temperature ion implantation methods. During ion implantation, the substrate is kept at a constant temperature and the diffusion of aluminum is enhanced by the vacancies and interstitials generated by the bombarding ions; so the diffusion occurs

under an isothermal condition. During laser doping, however, the substrate experiences both temporal and spatial variation of temperature (Figs. 3-6); so the diffusion occurs under a non-isothermal condition. Therefore, the variation of the diffusion coefficient as a function of temperature, D(T), needs to be considered to understand the laser doping process. The temperature dependence of D(T) can be approximated by

$$D(T) = D_0^* \exp(-\frac{T_A}{T(z,t)}) \ . \tag{4.4}$$

Here D_0^* is the pre-exponential factor, T(z,t) is the absolute temperature of the substrate and T_A is the activation temperature for the diffusion process, which is defined as

$$T_A = Q/k_B \tag{4.5}$$

where Q is the activation energy and k_B is the Boltzmann constant.

For symmetric lattice structures, interstitial diffusion has a lower activation energy (Q=0.5-1.5eV) than substitutional diffusion (Q=3-5eV) [Pankove, (1999)] since no energy is required to form a vacancy in interstitial diffusion. So the dopant atoms possessing higher thermal energy near the wafer surface could be capable of diffusing by more than one mechanism, such as substitutional and interstitial mechanisms, simultaneously. As the diffusion depth increases, the diffusion mechanism changes depending on the specifics of the laser-induced temperature field and the diffusivity is expected to decrease. Based on the available data [Neudeck et al. (2000) and Ruschenschmidt et al. (2001)] for the diffusion coefficients of N_2 and Al in SiC in the temperature range of 1800°C - 2450°C, the values of Q are calculated to be 2.25 eV for

nitrogen and 3.40 eV for aluminum and the values of D_0^* are found to be 5.8×10^{-8} cm^2/s and 5.9×10^{-6} cm^2/s for N_2 and Al respectively by using Eq. (4.4).

Since the peritectic reaction temperature for SiC is ~ 2800 °C, the dopant diffusion temperature T(z, t) will be less than the peritectic temperature for laser doping of SiC without melting the wafer. However the activation temperatures ($T_A = Q/k_B$) are 2.6×10^4 K and 3.9×10^4 K for nitrogen and aluminum, respectively, which are much larger than T(z, t). So the ratio $T_A/T(z,t)$ is very large. This fact will be utilized later in this section to determine the mass diffusion length.

The one-dimensional dopant diffusion process can be represented by [Libenson et al. (1973)]

$$\frac{\partial C(z,t)}{\partial t} = \frac{\partial}{\partial z}\left(D(T(z,t))\frac{\partial C(z,t)}{\partial z}\right) \qquad z \geq 0, \quad t > 0 \tag{4.6}$$

$$C(z,0)=0 \qquad z > 0 \tag{4.7a}$$

$$C(0,t) = C_0 \qquad t > 0 \tag{4.7b}$$

$$C(\infty,0)=0 \qquad t > 0 \tag{4.7c}$$

The thermal diffusivity of 6H-SiC is 2.2 cm^2/s, which is much higher than the mass diffusivity of various dopants in SiC (Table 4.2). Therefore, the thermal diffusion length is expected to be much deeper than the mass diffusion length. So the temperature can be considered to be uniform over the small mass diffusion length and then Eq. (4.6) can be

solved by considering $D(T(z,t))$ to be a function of the substrate surface temperature,

i.e., $D(T(z,t)) = D(T(0,t))$. (4.8)

So Eq. (4.6) can be rewritten as

$$\frac{\partial C(z,t)}{\partial t} = D(T(0,t))\frac{\partial^2 C(z,t)}{\partial z^2} \tag{4.9}$$

To solve Eq. (4.9) a new variable η is defined such that

$$\eta = \int_0^t D(T(0,t'))dt' \tag{4.10}$$

Then we can get

$$C(z,t) \equiv C'(z,\eta) \tag{4.11}$$

or $\frac{\partial c}{\partial z}dz + \frac{\partial c}{\partial t}dt \equiv \frac{\partial c'}{\partial z}dz + \frac{\partial c'}{\partial \eta}d\eta$ (4.12)

This yields

$$\frac{\partial c}{\partial z} = \frac{\partial c'}{\partial z} \tag{4.13}$$

and $\frac{\partial c}{\partial t}dt = \frac{\partial c'}{\partial \eta}d\eta$ (4.14)

or $\frac{\partial c}{\partial t} = \frac{\partial c'}{\partial \eta}\frac{d\eta}{dt} = \frac{\partial c'}{\partial \eta}D(T(0,t))$ (4.15)

Then considering Eq. (4.9), (4.11) and (4.15) together, Eq. (4.16) can be obtained

$$\frac{\partial C'(z,\eta)}{\partial \eta} = \frac{\partial^2 C'(z,\eta)}{\partial z^2} \tag{4.16}$$

The solution to Eq. (4.16) yields the following expression for the dopant concentration distribution:

$$C'(z,\eta) = C_0 erfc(\frac{z}{l_m}), \tag{4.17}$$

satisfying the initial and boundary conditions (4.7a-c). It should be noted that Eq. (4.17) is based on the assumption that the host lattice contains no dopant atoms prior to the onset of the diffusion process and therefore it is suitable only for a single irradiation pass. The mass diffusion length l_m in Eq. (4.17) is given by

$$l_m \approx 2\sqrt{\int_0^t D(T(0,t'))dt'} \tag{4.18}$$

Now $\int_0^t D(T(0,t'))dt' = D_0 \int_0^t e^{-\frac{T_A}{T(0,t')}} dt'$ (4.19)

Generally $T_A >> T(0,t')$. We define

$$\theta = T(0,t') \tag{4.20}$$

then $d\theta = \frac{\partial T(0,t')}{\partial t'} dt'$ (4.21)

or $dt' = \frac{d\theta}{\dot{T}(0,t')}$ (4.22)

So Eq. (4.19) can be rewritten as

$$\int_0^t dt' D(T(0,t')) = D_0 \int_0^{T(0.t)} \frac{e^{-\frac{T_A}{\theta}}}{\dot{T}(0,t')} d\theta \tag{4.23}$$

and this equation can be approximated by

$$\int_0^t dt' D(T(0,t')) \approx \frac{D_0}{\frac{\partial T(0.t)}{\partial t}} \int_0^{T(0,t)} e^{-\frac{T_A}{\theta}} d\theta$$

$$\approx \frac{T^2(0,t)}{T_A \dot{T}(0,t)} D_0 e^{-\frac{T_A}{T(0,t)}}$$

$$= \frac{T^2(0,t)}{T_A \dot{T}(0,t)} D(T(0,t)) \tag{4.24}$$

the surface temperature is

$$T(0,t) = \frac{2I\sqrt{\alpha t}}{k\sqrt{\pi}} \tag{4.25}$$

and $\dot{T}(0,t) = \dfrac{I\sqrt{\alpha}}{k\sqrt{\pi t}}$ (4.26)

then $\dfrac{T^2(0,t)}{\dot{T}(0,t)} = T(0,t)\dfrac{\frac{2I\sqrt{\alpha t}}{k\sqrt{\pi}}}{\frac{I\sqrt{\alpha}}{k\sqrt{\pi t}}}$

$$= 2T(0,t)t \tag{4.27}$$

So the integral in Eq.(4.18) can be approximated as [Libenson et al. (1973)]

$$\int_0^t dt' D(T(0,t')) \approx \frac{2T(0,t)D(T(0,t))t}{T_A} \tag{4.28}$$

Eq. (4.18) and Eq. (4.28) yield

$$l_m = 2\sqrt{\frac{2T(0,t)tD(T(t))}{T_A}} \tag{4.29}$$

or $\quad \mathrm{D(T(0,t))} = \dfrac{l_m^2 \mathrm{T_A}}{\mathrm{8T(0,t)t}}$ (4.30)

or $\quad D(T(0,t)) = \dfrac{l_m^2 T_A}{8 \times \frac{2I\sqrt{\alpha t}}{k\sqrt{\pi}} t}$

$$= \frac{{l_m}^2 T_A}{\frac{16}{\sqrt{\pi}} \times I \times \sqrt{\frac{k}{\rho C_p}} \times t^{\frac{3}{2}}} \tag{4.31}$$

Now C(z, t) can be expressed as

$$C(z,t) = C_0 erfc\left(\frac{z}{2\sqrt{\frac{2T(0,t)tD(T(t))}{Q/k_B}}} \right) \tag{4.32}$$

For the near-surface region the diffusion time t is taken as 20% and 10% of the total laser-wafer interaction time for Nd:YAG and excimer lasers, respectively. These percentages approximately correspond to the high temperature (~3000 K) heating time during which the vacancies are expected to form in high concentrations at the near-surface region [Bäuerle (2000)], leading to high diffusivity. A higher percentage is chosen for Nd:YAG laser doping because the substrate remains at higher temperatures for longer times than in the case of excimer laser doping as discussed in Section 4.2. The total laser-wafer interaction time is given by $P_r t_{irr} t_{on}$, where P_r is the pulse repetition rate, t_{irr} is the total laser irradiation time (pulse-on plus pulse-off times), t_{on} is the pulse length (pulse-on time). t_{irr} is given by $2r_0/v$ in the case of a scanning beam, where r_0 is the radius of the laser beam on the wafer surface and v is the laser scanning speed.

The calculated concentration profile C(z, t) matches with the nitrogen dopant profile (Fig. 4.8a, Nd:YAG laser doping process) at the near-surface region within 160 nm very well for t = 13 μs, T(0,t) ≈ 3000 K and D(T(t)) ≈ 2.4×10^{-5} cm^2/s, validating the approximation D(T(z,t)) ≈ D(T(0,t)). For the case of excimer laser doping, the calculated concentration profiles C(z,t) for both 1000 and 3000 laser pulses also match well with the experimental aluminum dopant profile (Fig. 4.9a) at the near-surface region over a depth

of 120 nm for 1000 pulses and 150 nm for 3000 pulses for t = 2.5 and 7.5 μs for 1000 and 3000 laser pulses, respectively, T(0,t) ≈ 3000 K and D(T(t)) ≈ 1.2×10^{-5} cm^2/s for both pulses.

However, the theoretical dopant profile deviates from the experimental data at the far-surface region because the temperature there is significantly different from the substrate surface temperature, T(0,t) and, therefore, the above approximation is invalid in the far-surface region. Additionally different diffusion mechanisms dominate in the near-surface and far-surface regions. At the near-surface region the dopant atoms can diffuse by occupying vacancies created by laser irradiation, and interstitial sites. The effect of lasers on the creation of vacancies generally diminishes as the distance from the hottest point increases. So the diffusion mechanism gradually changes with distance and ultimately it is dominated by the interstitial mechanism in the far-surface region. So the theoretical dopant profile, Eq. (4.32), can be modified as follows by considering another effective diffusion coefficient, which denotes the diffusion behavior in the far-surface region.

$$C(z,t) = C_0 erfc\left(\frac{z}{2\sqrt{\dfrac{2T(0,t)tD(T(t))}{Q/k_B}}} \right) + C_1 erfc\left(\frac{z}{2\sqrt{D_{fs}t'}} \right) \tag{4.33}$$

Here C_1 is a characteristic concentration representing the diffusion process in the far-surface region, D_{fs} denotes the average diffusion coefficient in the far-surface region and t' is the diffusion time in the far-surface region, which is taken as the total laser-wafer interaction time for the Nd:YAG and excimer lasers respectively. The values of t, t', C_0,

C_1, Q and k_B are listed in Table 4.2 for both Nd:YAG and Excimer laser doping experiments. The modified profile, Eq. (4.33), fits the experimental dopant profile quite well as shown in Fig. 4.8b (Nd:YAG laser doping) for $C_1 = 1.4\times10^{20}$ cm^{-3}, $D_{fs} = 9.2\times10^{-6}$ cm^{-3} and $t' = 65$ µs. For the case of excimer laser doping the modified profiles also fit well with the experimental dopant profiles as shown in Fig. 4.9b for $C_1 = 1\times10^{19}$ cm^{-3}, t' = 25 µs and $D_{fs} = 1.3\times10^{-6}$ cm^{-3} in the case of 1000 laser pulses, and $C_1 = 1.7\times10^{20}$ cm^{-3}, t' = 75 µs and $D_{fs} = 1.3\times10^{-6}$ cm^{-3} in the case of 3000 laser pulses.

Two sets of diffusion coefficients are obtained for each laser doping process and these values are listed in Table 4.3. Similar enhancement in the dopant diffusion coefficient has been reported for laser doping in Si [Kimerling (1980)] as listed in the table. The mass diffusivities of nitrogen are 2.4×10^{-5} cm^2/s for near-surface region and 9.2×10^{-6} cm^2/s for far-surface region. The corresponding results of aluminum are 1.2×10^{-5} cm^2/s for near-surface region and 1.3×10^{-6} cm^2/s for far-surface region. These values are 6 order of magnitude higher than the typical values of 5×10^{-12} cm^2/s for nitrogen and 3×10^{-14} - 6×10^{-12} cm^2/s for aluminum [Schöner (2002)], indicating that lasers enhance the dopant diffusion in silicon carbide significantly.

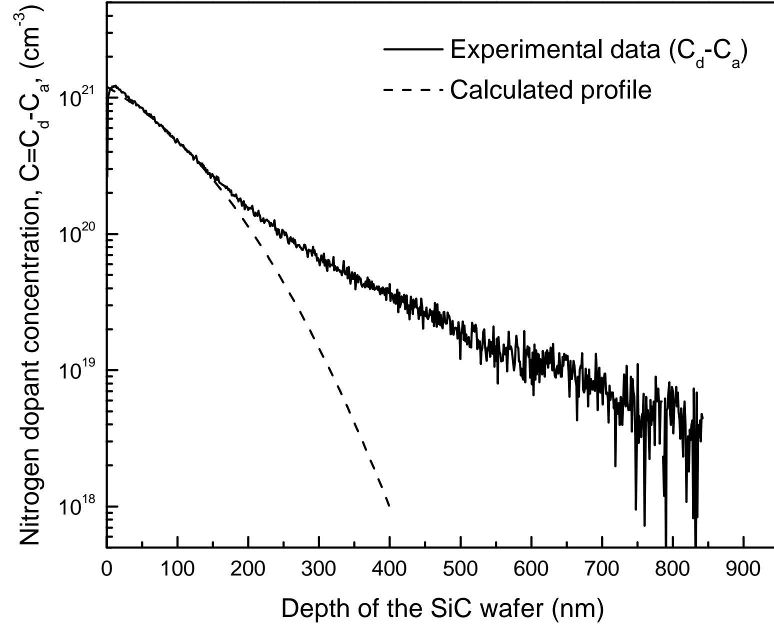

(a)

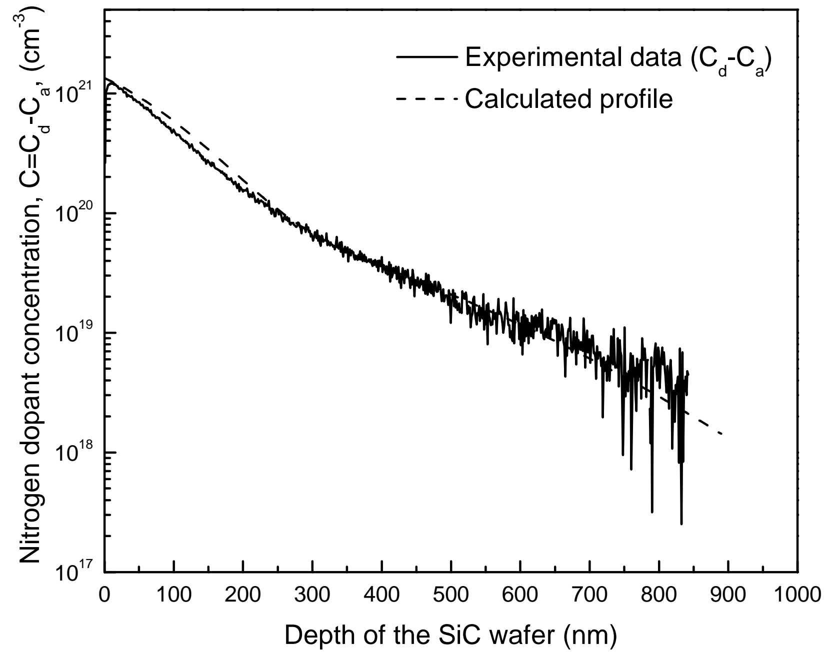

(b)

Figure 4.8 Comparison between the diffusion theory and experimental data for a selected diffusion coefficient in the case of Nd:YAG laser doping of nitrogen in 6H-SiC.

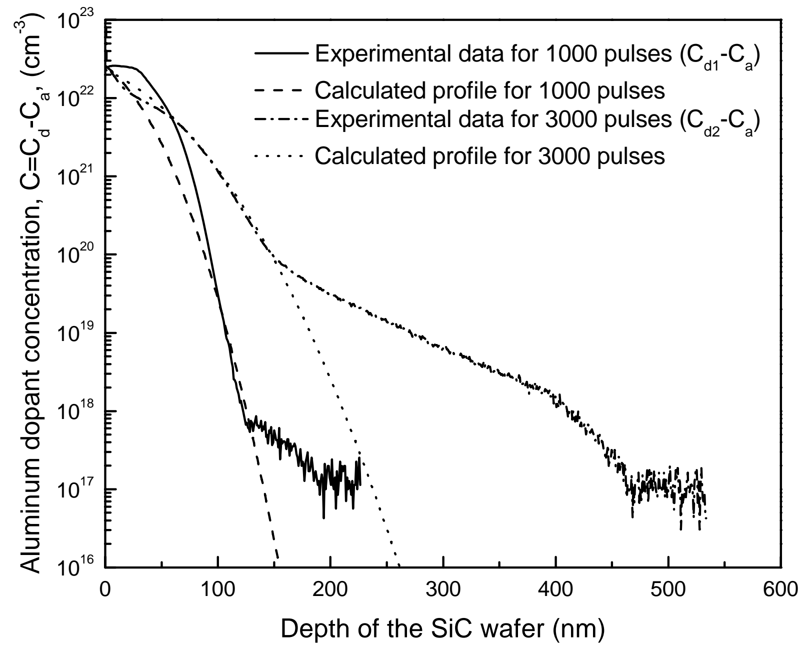

(a)

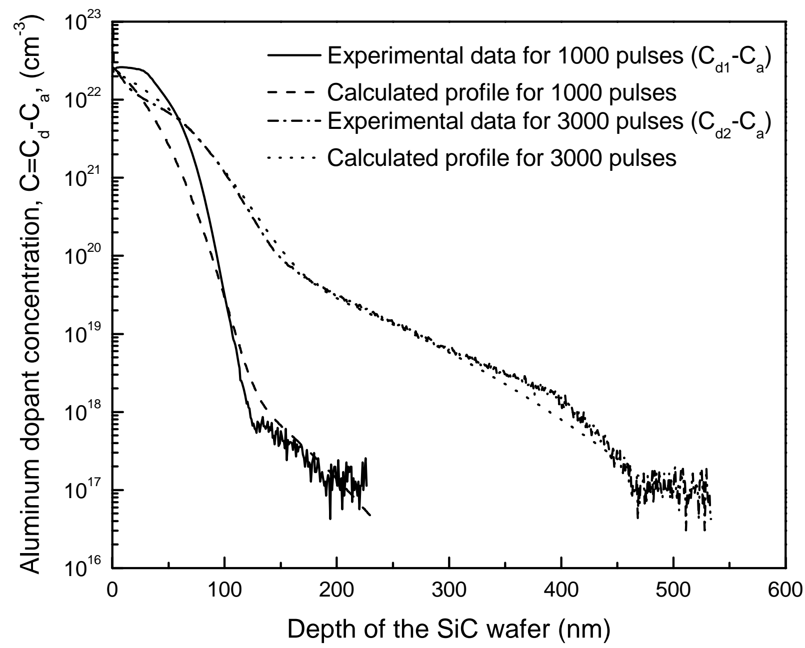

(b)

Figure 4.9 Comparison between the diffusion theory and experimental data for a selected diffusion coefficient in the case of KrF excimer laser doping of aluminum in 4H-SiC.

Table 4.2 Fitting parameters used in Eqs. 4.32 and 4.33 to compare the theory with experimental dopant profiles in Figs. 4.8 and 4.9 for determining the effective diffusivity.

Calculated curve	Fig. 4.8a	Fig. 4.8b	Fig. 4.9a, 1000 pulses	Fig. 4.9b, 1000 pulses	Fig. 4.9a, 3000 pulses	Fig. 4.9b, 3000 pulses
C_0 (cm^{-3})	1.2×10^{21}	1.2×10^{21}	2.5×10^{22}	2.5×10^{22}	2.5×10^{22}	2.5×10^{22}
t (s)	1.3×10^{-5}	1.3×10^{-5}	2.5×10^{-6}	2.5×10^{-6}	7.5×10^{-6}	7.5×10^{-6}
t' (s)	-	6.5×10^{-5}	-	2.5×10^{-5}	-	7.5×10^{-5}
T(0,t) (K)	~3000	~3000	~3000	~3000	~3000	~3000
$D_{near\text{-}surface}$ (cm^2/s)	2.4×10^{-5}	2.4×10^{-5}	1.2×10^{-5}	1.2×10^{-5}	1.2×10^{-5}	1.2×10^{-5}
C_1(cm^{-3})	-	1.4×10^{20}	-	1×10^{19}	-	1.7×10^{20}
$D_{far\text{-}surface}$ (cm^2/s)	-	9.2×10^{-6}	-	1.3×10^{-6}	-	1.3×10^{-6}
Q (eV)	2.3		3.4			
k_B (eV/K)	8.617×10^{-5}					

Table 4.3 Comparison of diffusion coefficients in conventional and laser doping processes for different impurities in SiC and Si.

<table>
<tr><th rowspan="2">Wafer</th><th rowspan="2">Dopant</th><th colspan="2">Conventional doping ([Schöner (2002)])</th><th colspan="3">Laser doping</th></tr>
<tr><th>Diffusion coefficient (cm^2/s)</th><th>Temperature (°C)</th><th>Near-surface Diffusion coefficient (cm^2/s)</th><th>Far-surface Diffusion coefficient (cm^2/s)</th><th>Surface temperature (°C)</th></tr>
<tr><td rowspan="2">SiC</td><td>N</td><td>5×10^{-12}</td><td>>2500</td><td>2.4×10^{-5}</td><td>9.2×10^{-6}</td><td>~3000</td></tr>
<tr><td>Al</td><td>3×10^{-14}-6×10^{-12}</td><td>>2500</td><td>1.2×10^{-5}</td><td>1.3×10^{-6}</td><td>~3000</td></tr>
<tr><td rowspan="2">Si</td><td>P</td><td>1×10^{-14}-6×10^{-11}</td><td>1100-1400</td><td colspan="2" rowspan="2">10^{-6}-10^{-5} ([Kimerling (1980)])</td><td>~ 1400</td></tr>
<tr><td>B</td><td>3×10^{-14}-5×10^{-11}</td><td>1100-1400</td><td>~ 1400</td></tr>
</table>

4.6 Laser Metallization Process of Silicon Carbide

Laser internal heating method, in which Nd:YAG laser with the wavelength of 1064 nm was utilized to dope and metallize the bottom surface of the n-type 6H-SiC substrate. The experiment was designed as a two-step process: in the first step, n-type SiC substrate was heavily laser doped with n-type dopant, nitrogen, to obtain an n^+ region at the near surface region, and then laser was utilized to direct metallize the surface of the n^+ region of the substrate (Sample A). Laser direct metallization of the original surface of SiC substrate without the introduction of n^+ region by laser doping was also conducted for comparison (Sample B). The laser irradiation parameters are listed in Table 4.4.

Fig. 4.10 shows the temperature distribution of SiC substrate during laser direct metallization using the parameters listed in Table 4.4. The peak temperature of the bottom surface, where is the location of highest temperature during the laser irradiation shown in Fig. 2.2, during one pulse, exceeds the decomposition temperature of silicon carbide (Fig. 4.10a). That means the outer layer of the bottom surface will experience the decomposition of silicon carbide and form a conductive carbon rich phase [Salama (2003)], which can serve as a direct metallization layer. The transient temperature distribution along the thickness of the wafer from the bottom surface at the peak temperature (t=48ns) (Fig. 4.10b) shows that the region exceeding the decomposition temperature is within 200 nm.

Table 4.4 Processing parameters for laser direct metallization.

Sample	A		B
Steps	1	2	1
Method	Laser dope	Laser metallization	Laser metallization
Laser source	Nd:YAG	Nd:YAG	Nd:YAG
Wavelength (nm)	1064	1064	1064
Pulse repetition rate (Hz)	3000	3000	3000
Beam area (cm^2)	$\pi(0.03)^2/4$	$\pi(0.03)^2/4$	$\pi(0.03)^2/4$
Pulse energy (mJ)	4	4.33	4.33
Laser fluence (J/cm^2)	5.65	6.1	6.1
Pulse intensity (MW/cm^2)	78.6	85.1	85.1
Scanning speed (mm/s)	1	1	1
Irradiation passes	1	1	1
Ambient gas	N_2 at 30 psi	Ar at 30 psi	Ar at 30 psi

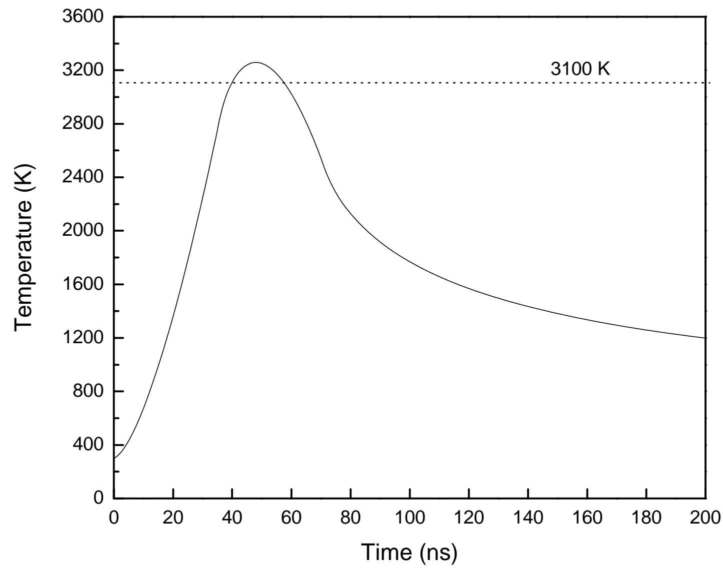

(a)

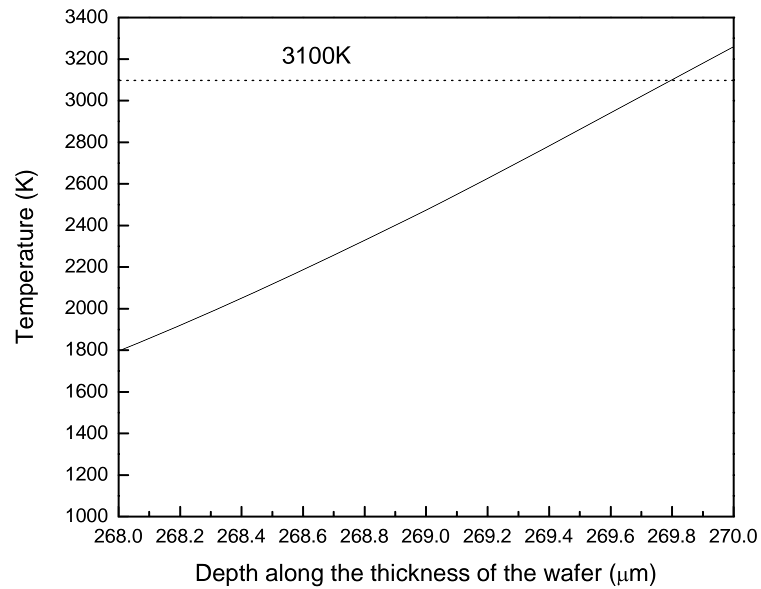

(b)

Figure 4.10 Temperature distribution of 6H-SiC during laser direct metallization using the parameters listed in Table 4.4.(a) Bottom surface temperature distribution with the time; (b) Transient temperature distribution along the thickness of the wafer from the bottom surface at the peak temperature (t=48ns).

4.7 Realization of Laser Direct Metallization on the Surface of Silicon Carbide

Using the processing parameters listed in Table 4.4, two different electrode structures are fabricated in n-type 6H-SiC substrates shown in Fig. 4.11: laser direct metallized contacts fabricated on laser heavily doped n^+ substrate (Fig. 4.11a, specimen A) and laser direct metallized contacts fabricated on original substrate (Fig. 4.11b, specimen B). The doping profile of laser heavily doped n^+ region can be found in Fig. 4.4, where the substrate was doped to the thickness of 800 nm with a very high surface dopant concentration (1×10^{21} cm^{-3}). Ni ohmic contacts were also marked and deposited on original SiC substrate (Fig. 4.11c, specimen C) by DC magnetron sputtering as reference ohmic contacts to judge on the behavior of the laser generated contacts. To assure the ohmic behavior of the Ni-SiC contact, a high temperature annealing (at 1050°C for 5 min.) was conducted in argon [Porter, (1995)] after the Ni contact deposition. The sizes of all the electrodes are 400 μm × 400 μm and the distances between two electrodes are about 300 μm.

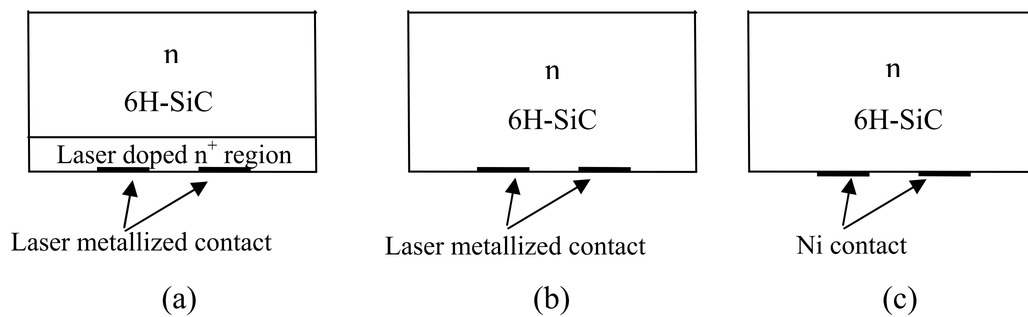

Figure 4.11 Electrode structures in n-type 6H-SiC substrates by different processing: (a) laser direct metallized contacts fabricated on laser heavily doped n^+ substrate (specimen A); (b) laser direct metallized contacts fabricated on original substrate (specimen B); (c) Ni contacts deposited on original substrate (specimen C).

The performance of laser direct metallization of carbon rich contacts in the SiC substrates can be evaluated by comparing the current-voltage (I-V) characteristics of the laser direct metallized electrodes with those of electrodes fabricated by Ni deposition. The I-V measurements were conducted by contacting the microprobes of the I-V measurement instruments directly on the electrodes.

Fig. 4.12 shows that the current-voltage characteristics between the two separated electrodes on the SiC substrate formed by three different methods at room temperature. These results show that all of the contacts between the SiC substrate and the electrodes have ohmic properties, indicating that we have succeeded in the formation of the laser direct metallized ohmic contacts on SiC substrate. However, the ratios of the rise of current to the applied voltage for the electrodes formed by the laser direct metallized methods (specimens A and B) are less than 0.7 of the Ni deposited one, which means the contact resistances of laser direct metallized contacts are higher than that of Ni deposited contacts. This may be due to the degradation of the surface layer, i.e., the surface decomposition layer could perturb the contact performance, such as a voltage drop across the electrode to the substrate [Eryu et al. (1997)]. On the other hand, laser direct metallized electrodes formed on heavily doped n^+ substrate increase the ratio of the rise of current to the applied voltage from 0.49 of that of the Ni deposited electrodes (data for the laser direct metallized electrodes on original substrate) to 0.67 of that of the Ni deposited ones. This means the combination of laser direct metallization and laser doping improve the performance of laser direct metallized contacts dramatically. Defects such as vacancies created during laser doping process may be associated with an enhanced

electron concentration underneath the contacts to promote tunneling in the substrate, and defect-assisted tunneling or recombination by point defects near the surface and well within the band gap may also contribute to the improvement of laser direct metallized ohmic contact on laser doped SiC substrate [Mohammad et al. (2005)].

The current-voltage characteristics between the two separated electrodes on the SiC substrate formed by these three methods at elevated temperatures (150 °C and 250 °C) are shown in Fig. 4.13. The ohmic behaviors of all the three kinds of electrodes improve with the increase of temperature indicating the specific contact resistances for all three cases decrease with the increase of temperature. Compared to the I-V characteristics of all the three cases at room temperature, same conclusion can be drawn, i.e., the performances of laser direct metallized contacts are comparable to that of Ni deposited contacts and combination of laser direct metallization with laser doping improve the performance of laser direct metallized contacts.

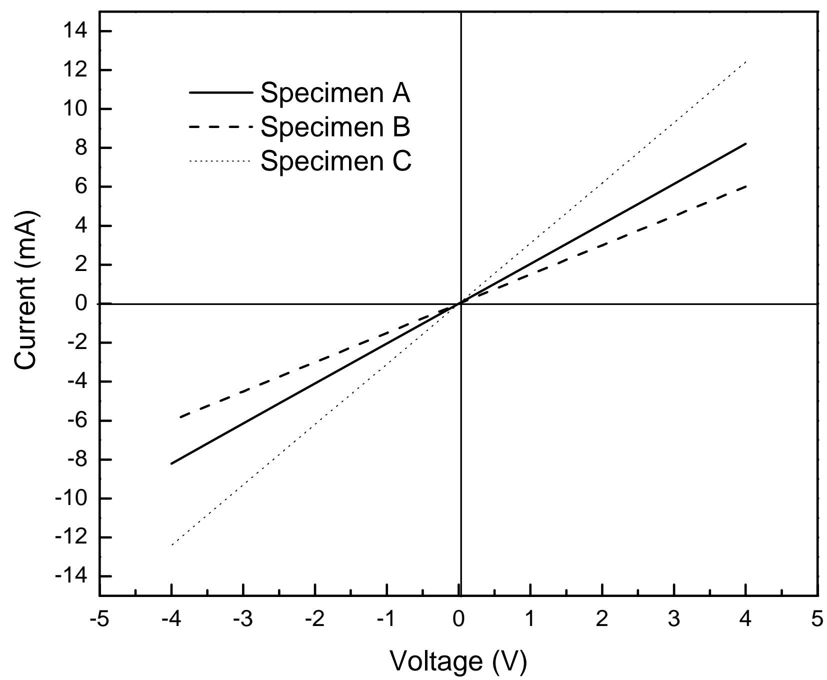

Figure 4.12 Current- voltage characteristics between two electrodes on the SiC substrates formed by different methods at room temperature.

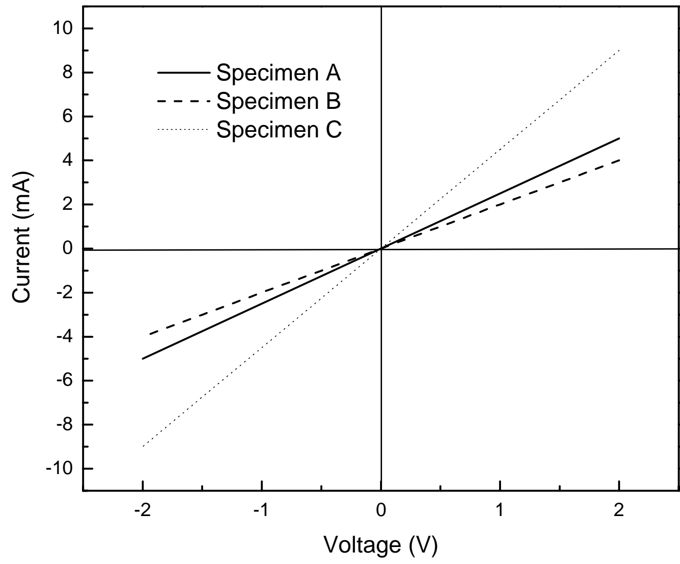

(a)

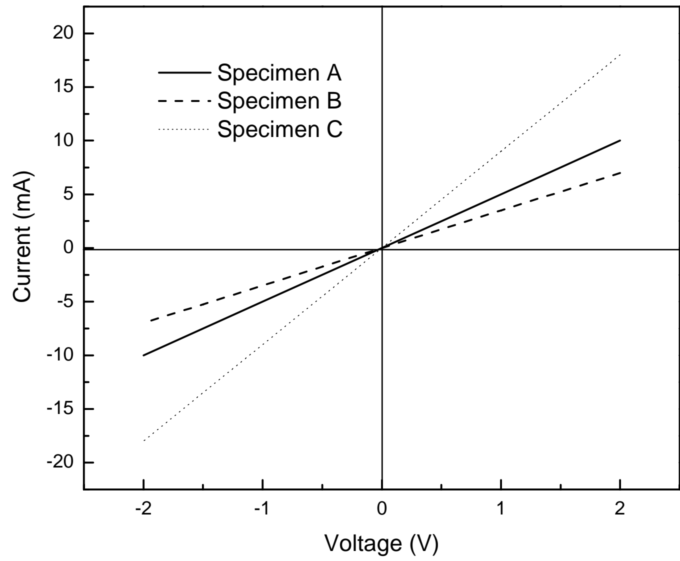

(b)

Figure 4.13 Current- voltage characteristics between two electrodes on the SiC substrates formed by different methods at elevated temperatures: (a) 150 °C; (b) 250 °C.

CHAPTER 5: FABRICATION OF ENDOLAYER AND PIN DIODES OF SILICON CARBIDE

5.1 Introduction

Pulsed laser can be used to produce epilayer by transforming an amorphous or disorder layer on a crystalline substrate into a thin crystalline layer, which is called pulsed laser-induced epitaxy (PLIE). PLIE can be described as a two-step process. Firstly, a target layer with unnecessary high quality crystalline and homogeneity is grown on top of a semiconductor substrate. In a second step a pulsed laser induces melting/solidification cycles to transform the top layer into a thin crystalline layer [Boulmer, et al. (1998)]. This technique has been successfully used to realize SiGeC/Si heterostructures [Boulmer, et al. (1995) and Kramer and Thompson. (1996)] and, GaP homoepitaxy [Solanki, et al. (1988)]. The application of this technique to single crystal silicon carbide, however, has not been reported because silicon carbide does not melt under equilibrium conditions at the normal pressure [Scace and Slack (1959)].

In this chapter an endotaxial layer was created by incorporating carbon into an epilayer-free SiC substrate with a pulsed laser using LISPD method. Carbon atoms are introduced into the top layer of an n-type SiC substrate to form a high resistance endolayer for various applications such as device isolation and high voltage blocking. The wafer is not melted in the LISPD method because this process is based on the solid-state diffusion for

dopant atoms into the wafer. The dopant precursor can be either a dopant film deposited on the wafer surface or a dopant gas (dopant-containing vapor) such as an organometallic compound surrounding the wafer in the processing chamber. The substrate is heated with a laser beam to diffuse the dopant atoms from the film or to cause pyrolytic decomposition of the dopant gas producing the dopant atoms that diffuses into the wafer.

SiC PIN diodes were also fabricated by laser doping different mediums including this endolayer and a parent homoepitaxial SiC layer grown by the conventional chemical vapor deposition (CVD) method. The performances of these diodes were compared with others' PIN diodes fabricated using epilayers and other doping techniques.

5.2 Fabrication of Endolayers in N-Type 6H-SiC Substrates

5.2.1 Experimental Procedures

An n-type 6H-SiC substrate with nitrogen dopant concentration of 5×10^{18} atoms/cm^3 was used to fabricate endolayers by incorporating carbon atoms into the top layer of the substrate using an excimer laser. This process relies on the principle that some of the nitrogen atoms diffuse out of the substrate during laser irradiation and the incorporated carbon atoms occupy the vacant sites left behind by the nitrogen atoms. The carbon atoms can also occupy other vacancies as well as defect sites that might have been present in the parent substrate. The endotaxy process thus allows improvement of the

crystal lattice to an intrinsic semiconductor bond structure. Silicon atoms can also be incorporated into the SiC substrates to balance the deficiency of silicon atoms in the substrate. The incorporation of carbon and silicon atoms, therefore, provides a mechanism of improving the crystalline quality at the substrate surface.

An experimental set-up for laser endolayer fabrication and doping of the substrate is presented in Fig. 3.2. A laser beam irradiates the substrate placed in a vacuum chamber, while an appropriate gas, such as methane (CH_4) for carbon incorporation or trimethylaluminum ($(CH_3)_3Al$) for aluminum doping of SiC, is passed through the chamber. A convex lens of focal length 250 mm is used to create different focused spots on the substrate surface. Various laser processing parameters are listed in Table 5.1. KrF and ArF excimer lasers of wavelengths 248 and 193 nm respectively were used for endolayer fabrication by incorporating carbon using methane as the precursor gas.

5.2.2 Carbon Source

Methane is generally cracked into carbon and hydrogen atoms through pyrolytic decomposition at relatively low temperatures (500 - 800°C) using specific catalysts [Fukada, et al. (2004)]. Although no special catalyst was used in this study, the pyrolysis of methane may occur at the laser-heated substrate surface at high temperatures. The photolysis of methane is also possible due to its interaction with the photons of the laser beam. These two chemical reactions can be written as follows.

Pyrolytic decomposition [Sharma et al. (1999)]:

Table 5.1 Laser processing parameters for endotaxy experiments.

	Endolayer formation	Endolayer formation
Laser source	KrF excimer	ArF excimer
Wavelength (nm)	248	193
Pulse length (ns)	25	20
Pulse energy (mJ)	75	50
Laser fluence (J/cm^2)	1.5	1
Pulse intensity (MW/cm^2)	60	50
Pulse repetition rate (Hz)	1	1
Laser shots	600	600
Beam area (cm^2)	0.2×0.25	0.2×0.25
Ambient gas	Methane at 30 psi	Methane at 30 psi

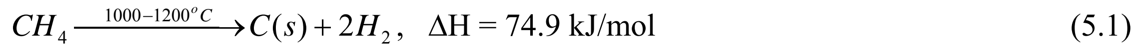

$$CH_4 \xrightarrow{1000-1200^o C} C(s) + 2H_2, \quad \Delta H = 74.9 \text{ kJ/mol} \qquad (5.1)$$

Photolytic decomposition [Mazumder and Kar (1995)]:

$$CH_4\,(g) + h\nu\ \ (4.3\,eV) \rightarrow C\,(s) + 2H_2\,(g) \qquad (5.2)$$

The substrate surface peak temperature can be estimated using the following expression [Tian, et al. (2005)]:

$$T(t) = T_0 + \frac{2I_l A\sqrt{\alpha}}{k\sqrt{\pi}}\sqrt{t} \qquad \text{for } t \le t_p. \qquad (5.3)$$

Here T(t) is the peak temperature at any time t as the laser irradiation progresses, T_0 is the initial temperature of the substrate, I_l is the laser irradiance, A is the absorptivity which is taken as 0.71 and 0.58 at the wavelengths of 248 and 193 nm respectively for 6H-SiC [Levinshtein, et al. (2001)], α is the thermal diffusivity which is 2.2 cm^2s^{-1} for 6H-SiC, k is the thermal conductivity which is 4.9 $Wcm^{-1}°C^{-1}$ for 6H-SiC and t_p is the laser pulse length. For laser irradiances of 60 and 50 MW/cm^2 during KrF and ArF laser endotaxy experiments respectively, the corresponding peak temperatures are estimated to be 2330°C and 1430°C.

Since these temperatures are much higher than the pyrolytic decomposition temperature as given in chemical reaction (5.1), the pyrolysis of methane is expected to occur in the present case. Since the carbon atoms are removed from the reaction product due to their diffusion into the substrate, reaction (5.1) will proceed in the forward direction under nonequilibrium conditions, which generally increases the reaction yield. On the other hand, photolytic reaction (5.2) is also expected to occur in the present case since the energy of a photon of the KrF and ArF excimer lasers are 5 and 6.4 eV respectively,

which are higher than the energy of a carbon-hydrogen bond (413 kJ/mole, i.e., 4.3 eV) in methane [Speight (2003)]. So both the pyrolytic and photolytic reactions will contribute to the formation of carbon atoms from methane for the formation of endolayers.

5.2.3 Hydrogen removal from the endolayer

It should be noted that both carbon and hydrogen atoms are generated in the chemical reaction and both of them can diffuse into the substrate. To produce contamination-free, i.e., hydrogen-free endolayers, the samples were annealed at 1000 °C for 10 min in an Ar ambient after the laser endotaxy experiment in order to diffuse out the hydrogen atoms. Fig 5.1 shows the concentrations of hydrogen in the endolayer, annealed endolayer and parent wafer measured by SIMS. The endolayer samples are prepared by KrF excimer laser irradiation. It indicates that the annealing process reduces the hydrogen concentration to the background level of the parent sample. The data in this figure are normalized by the silicon concentration in the silicon carbide substrate. During carbon incorporation hydrogen atoms also diffuse into the substrate with the peak normalized concentration of 0.45% decreasing to 0.15% at the depth of 300 nm. After annealing the SiC endolayer at 1000 °C for 10 min, almost all of the hydrogen atoms diffuse out of the substrate; the hydrogen concentration decreases to the original–content in the parent substrate.

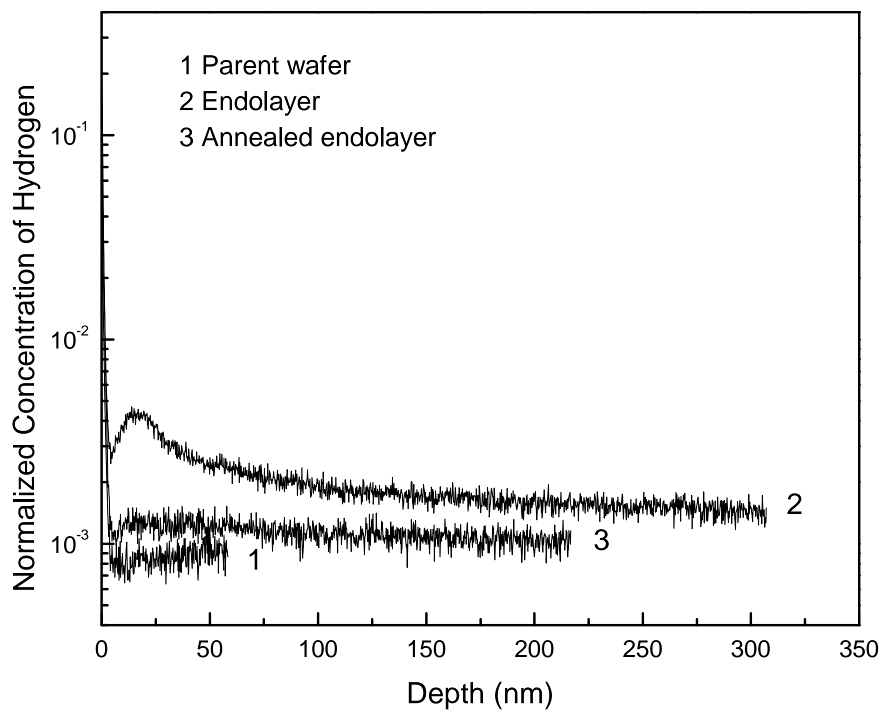

Figure 5.1 Comparison of the hydrogen content in a 6H-SiC sample of three different qualities.

5.2.4 Determination of the Thickness and Crystalline Order of the Endolayer

To examine the effect of laser processing on the crystalline order of the endolayer, TEM images of an annealed endolayer that was prepared by ArF excimer laser irradiation were compared with those of the parent wafer. The samples were sputter-coated with a ~ 40 nm Au layer using an Emitech K550 sputtering equipment. A Focused Ion Beam (FIB) instrument was used to obtain cross-sections of these samples in order to prepare TEM specimens. Platinum film was deposited by Ga^+ ion beam-assisted CVD as a protective layer for subsequent FIB milling operation. The TEM studies were carried out with a FEI Tecnai F30 TEM operating at 200 keV with x-ray energy dispersive spectrometry (XEDS). The thickness of the endolayer was measured by XEDS.

Figures 5.2a and b show two XEDS scanning line with four points a, b, c and d on each line for the endolayer and parent samples respectively. The carbon concentrations along these lines were measured by XEDS equipped with the TEM instrument, and the data are presented in Fig. 5.2c. The XEDS scan starts from the platinum film (point a) and ends at a depth of about 400 nm in the bulk of the SiC substrate (point d) for both samples as shown in Figs. 5.2a and b. Comparing the carbon counts of these two samples in Fig. 5.2c, it can be observed that the carbon concentration is nearly constant in the parent sample whereas the endolayer specimen exhibits a carbon-rich region. This region is bounded between two vertical dashed lines in Fig. 5.2c, at the depths of 65 and 163 nm corresponding to points b and c respectively in Fig. 5.2a. So the endolayer can be

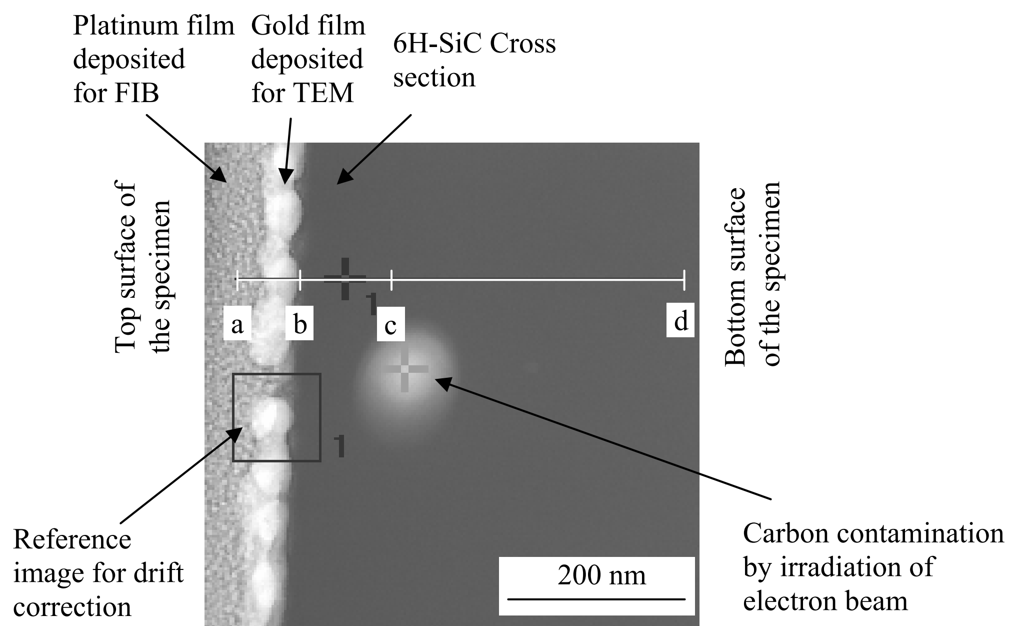

(a)

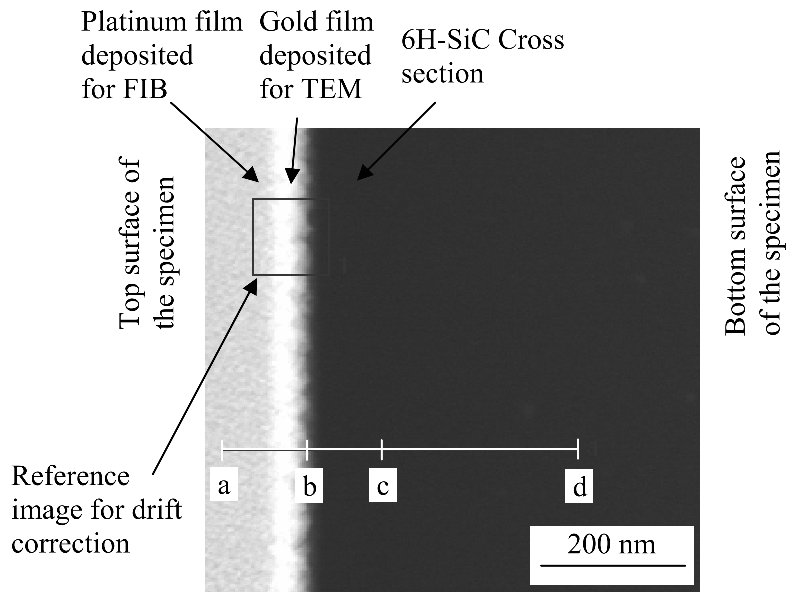

(b)

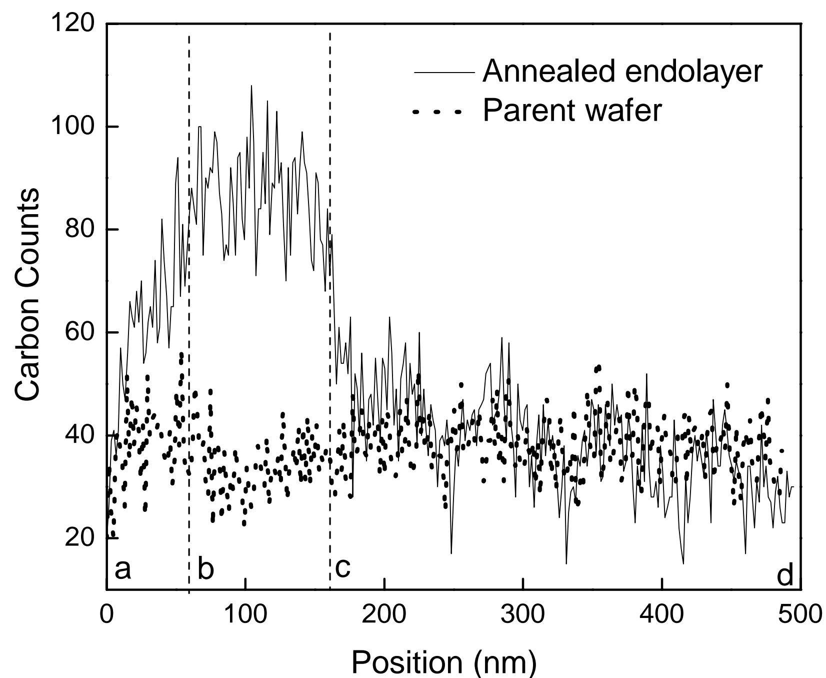

(c) XEDS data for carbon counts along the depth of the specimens.

Figure 5.2 XEDS analysis for the carbon contents along the depth of both annealed endolayer specimen and parent wafer: (a) XEDS scanning line showing four locations a, b, c and d along the depth of the endolayer specimen; (b) XEDS scanning line showing four locations a, b, c and d along the depth of the parent specimen; (c) XEDS data for carbon counts along the depth of the specimens. The four locations a, b, c and d are marked on these data to show higher carbon content in the endolayer than in the parent specimen, indicating carbon incorporation into the wafer during the endotaxy experiment.

considered to be about 100 nm thick, containing a larger amount of carbon than the parent substrate.

TEM images of the cross-sections of an annealed endolayer and a parent substrate are presented in Fig. 5.3 to show that the laser endotaxy process does not generate defects in the substrate. Fig. 5.3a shows an amorphous layer of thickness of ~17 nm at the surface of the annealed endolayer specimen. A similar amorphous layer is also present at the surface of the parent wafer in Fig. 5.3b, indicating that amorphization is not due to the laser processing. The TEM image at a higher magnification in Fig. 5.4a shows the integrity of crystalline lattices beneath the amorphous layer, which is comparable to the crystalline lattices of the parent wafer in Fig. 5.4b.

The amorphous layers in both types of specimen may have formed during the deposition of the platinum film that was used as a protective layer for subsequent FIB milling of the sample to produce TEM specimen. Although a gold film was directly deposited on top of the SiC substrate, the platinum film deposition process is expected to amorphize the specimens as explained below. The platinum film was deposited by Ga^+ ion beam-assisted chemical vapor deposition using an accelerating voltage of 30 kV with 2.2 μA beam current. Lipp et al [Lipp, et al (1996)] and Kempshall et al [Kempshall, et al (2002)] reported amorphous layers of thickness 40-50 nm on silicon substrates due to platinum deposition with a 30 kV Ga^+ ion beam. Even a sputter-deposited 70 nm thick Au-Pd coating on a silicon substrate could not completely prevent the substrate damage during the subsequent 30 kV Ga^+ ion beam-assisted platinum deposition [Kempshall, et

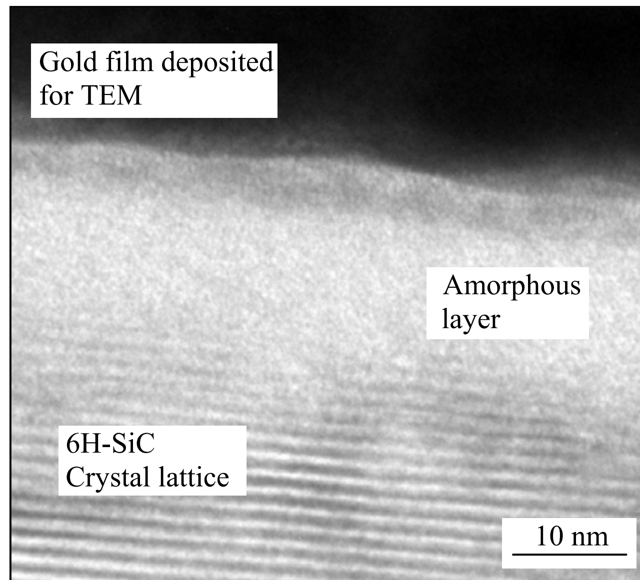

(a)

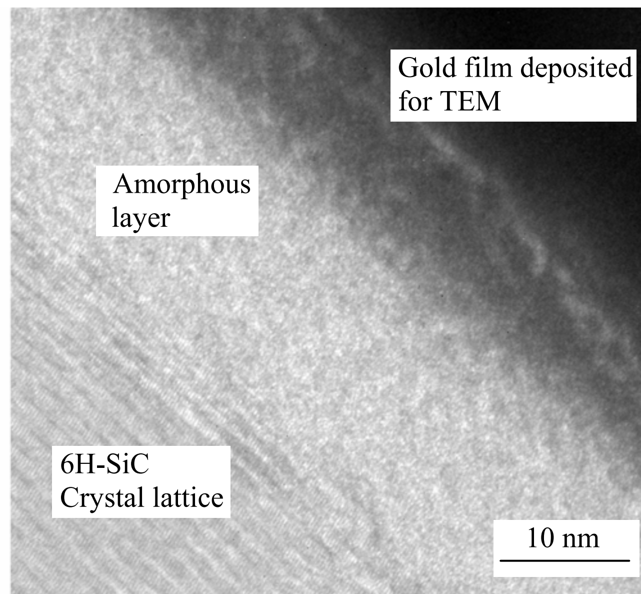

(b)

Figure 5.3 TEM images of cross-sections of an annealed endolayer and parent wafer: (a) Observed amorphous layer in the endolayer specimen; (b) Observed amorphous layer in the parent wafer.

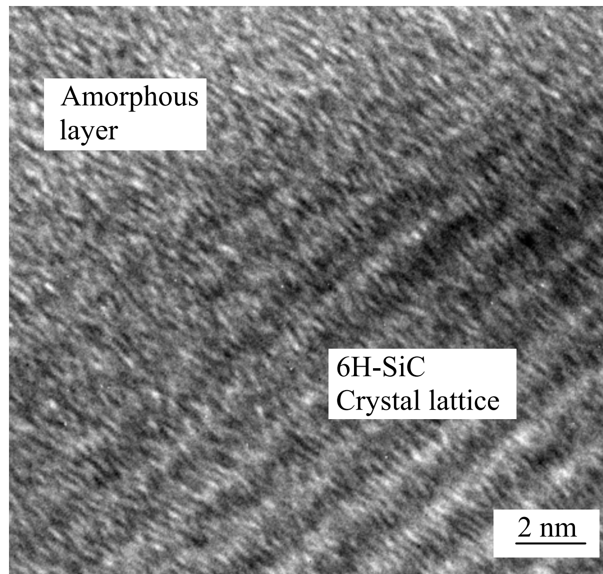

(a)

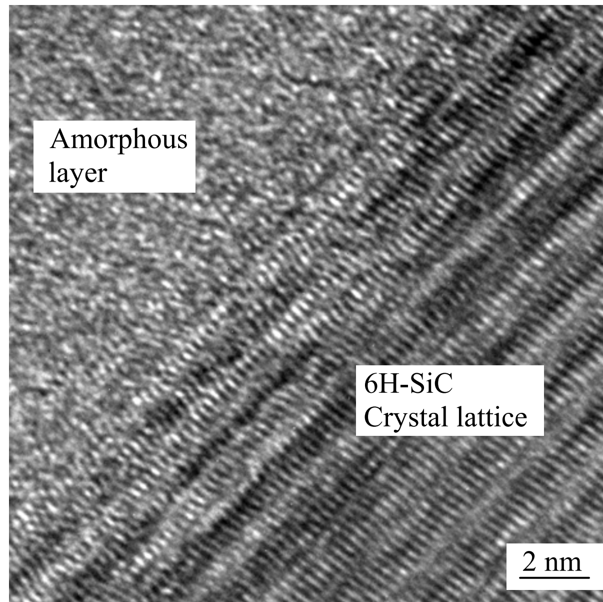

(b)

Figure 5.4 High-resolution TEM images of cross-sections of an annealed endolayer and parent wafer: (a) The interface between damaged amorphous and crystalline SiC of the endolayer specimen; (b) The interface between damaged amorphous and crystalline SiC of the parent wafer.

al (2002)]. In our studies, gold coatings of thicknesses 41 and 44 nm were sputter-deposited on the endolayer (Fig. 5.2a) and parent (Fig. 5.2b) samples respectively to prevent any substrate damage during the subsequent platinum film deposition process, but the gold films were evidently not thick enough to prevent amorphization at the sample surface.

The aligned and random RBS channeling spectra of endolayer and annealed endolayer specimens that are prepared by KrF excimer laser irradiation as well as the parent wafer are also compared to analyze the lattice disorder of this laser-induced solid phase diffusion process, which are shown in Figs. 5.5-5.7, respectively. The aligned spectra for the endolayer specimen and annealed endolayer specimen are very similar to the one for the parent wafer, indicating no evident damage to the lattices occurs during the laser-induced solid phase diffusion process. The RBS data also shows the crystalline integrity of the endotaxy process.

Al, N, He and H ion implantations have been reported to cause amorphization in SiC [Canut, et al. (1997) and Musumeci, et al. (1996)]. RBS channeling spectra [Canut et al. (1997)] showed that aluminum ion implantation in SiC at room temperature (maximum Al concentration of about 5×10^{19} cm^{-3} and implantation depth of 50 nm) induced amorphization in the substrate and a general decrease of the backscattering yield was observed in the channeling region after annealing. The relative disorder remained large (80%) near the sample surface in spite of annealing at high temperatures. Nitrogen ion

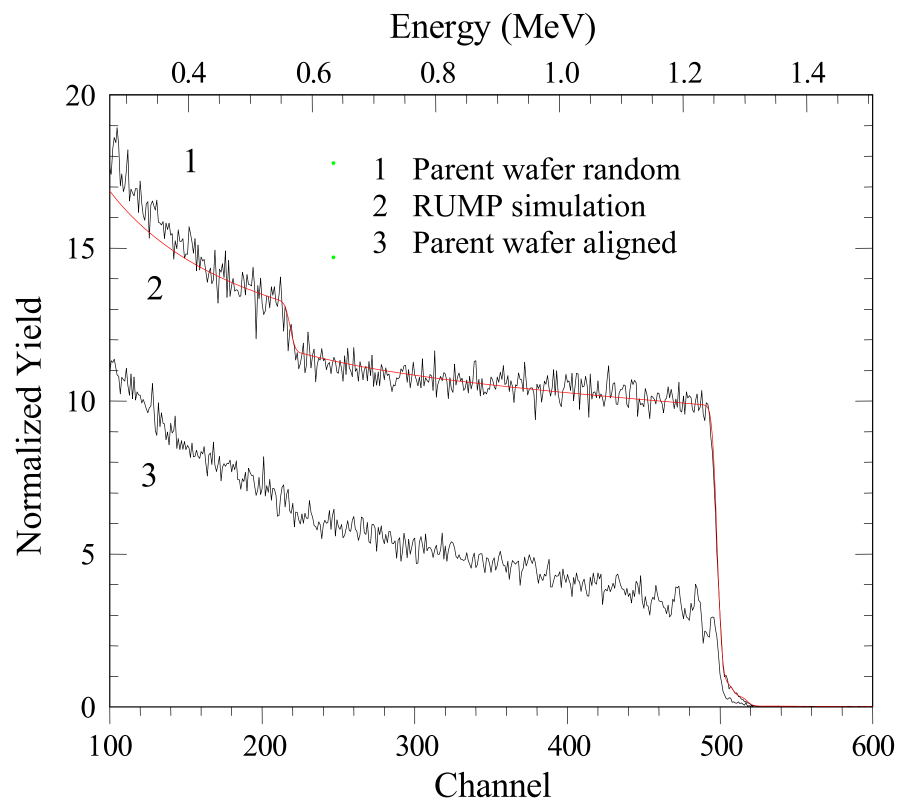

Figure 5.5 The aligned and random RBS channeling spectra of parent 6H-SiC sample.

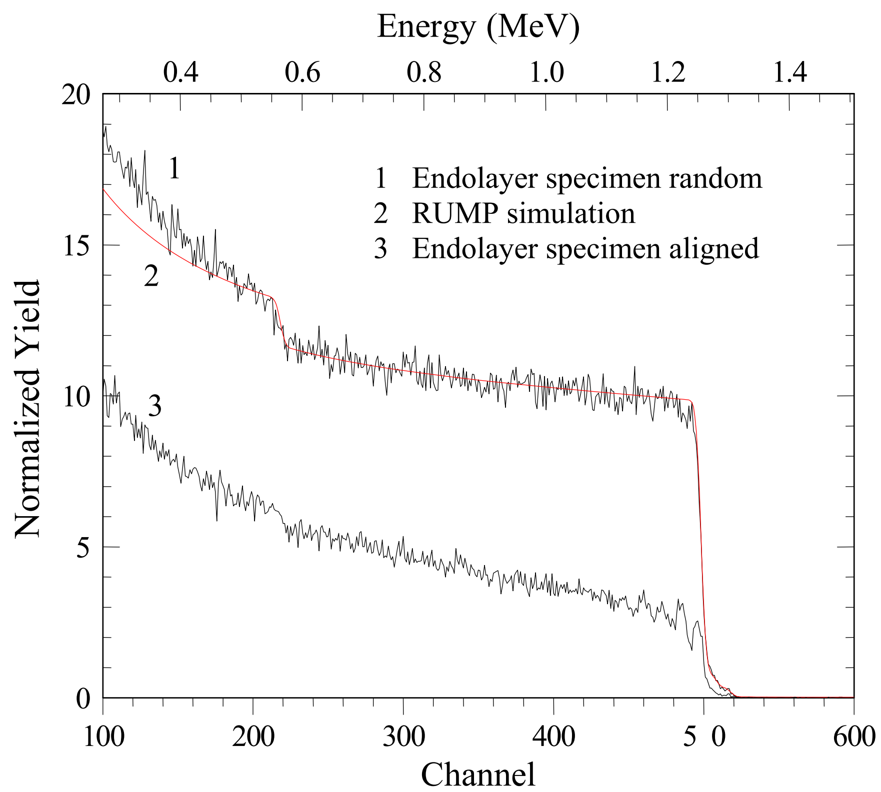

Figure 5.6 The aligned and random RBS channeling spectra of endolayer specimen.

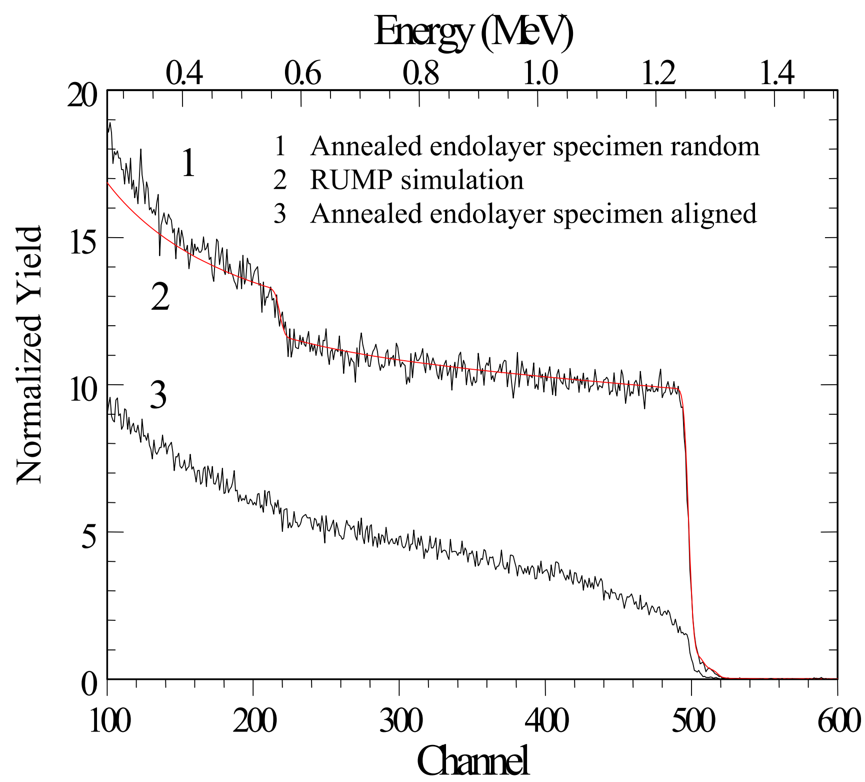

Figure 5.7 The aligned and random RBS channeling spectra of annealed endolayer specimen.

implantation at room temperature (maximum nitrogen concentration of about 5×10^{20} cm^{-3} and implantation depth of 450 nm) also amorphizes SiC [Kimoto, et al. (1997)].

Amorphization is caused by the elastic collisions of dopant atoms with the wafer lattice atoms and the long range order disappears when the threshold ion dose (ϕ_{th}) is exceeded during ion implantation. The amorphization process involves point defect accumulation [Musumeci, et al. (1996)], whereas annealing allows partial recrystallization of the amorphous phase [Canut, et al. (1997)]. Laser induced solid phase diffusion process does not cause amorphization due to different doping mechanism compared to the case of ion-implanted doping. Laser induced solid phase diffusion utilizes laser-heating to incorporate and diffuse impurities in a wafer. It is a diffusion-based process and elastic collisions between the dopant atoms and SiC lattice atoms are not evident.

5.2.5 Determination of the Resistivity of the Endolayer

To examine the resistivity of the endolayer, the I-V characteristics of the parent wafer, endolayer and the annealed endolayer samples that were prepared by ArF excimer laser irradiation were analyzed. For electrical characterization, Ni contacts were formed on both sides of an endolayer sample, an annealed endolayer sample and a parent 6H-SiC wafer using e-beam evaporation. The samples were annealed after Ni deposition at 1000°C for 1 min [Porter and Davis (1995)] for Ohmic contact. The current-voltage (I-V) measurements were performed using a Tektronix 576 curve tracer by contacting the Ni deposits with microprobes.

The samples are treated as a composite structure consisting of the contacts, endolayer and substrate in the case of endolayer samples and only the contacts and substrate in the case of the parent sample. The resistances of the endolayer samples (R_{total}) obtained from I-V measurements are the sums of the resistances of the endolayer (R_e), contacts (R_c) and substrate (R_s) [Nadella and Capano (1997)], i.e.,

$$R_{total} = R_e + R_c + R_s \tag{5.4}$$

Knowing R_{total} and the sum of the contacts and substrate of the parent sample, which yields the value of $R_c + R_s$, the resistances of both types of endolayer samples (R_e) are obtained from Eq. (5.4), and listed in Table 5.2. The resistivities of the endolayers (ρ_e) are estimated using the expression [Edwards, et al. (1997)], $\rho_e = R_e A_{Ni}/d_e$, where A_{Ni} is the area of the top Ni contact and d_e is the thickness of the endolayer. The value of d_e is determined as 100 nm from the XEDS data. The resistivities of the endolayer samples are also listed in Table 5.2 including the resistivities of intrinsic (pure) Germanium and Silicon for comparison. The resistivity of the endolayer is 1.1×10^5 Ω·cm, which is much higher than the resistivity needed for device isolation, 2×10^4 Ω·cm [Nadella and Capano (1997)]. After annealing, the resistivity of the sample decreases slightly to 9.4×10^4 Ω·cm, which may be due to the out-diffusion of hydrogen atoms thus losing any passivation caused by these atoms. Typical range of resistivities for insulators, semiconductors and conductors including silicon carbide is shown in Fig. 5.8 [Sze, (2001)].

Table 5.2 Resistances and resistivities of parent sample, endolayer and annealed endolayer.

Samples	R_c+R_s (Ω)	R_e+R_c+R_s (Ω)	R_e (Ω)	A_{Ni} (cm^2)	d_e (nm)	ρ_e (Ωcm)
Parent sample						1.55
Endolayer	12.5	62.5	50	0.15×0.15	100	1.1×10^5
Annealed endolayer	12.5	54.3	41.8	0.15×0.15	100	9.4×10^4
Intrinsic (pure) Germanium [Sze (1981)]						47
Intrinsic (pure) Silicon [Sze (1981)]						2.3×10^5

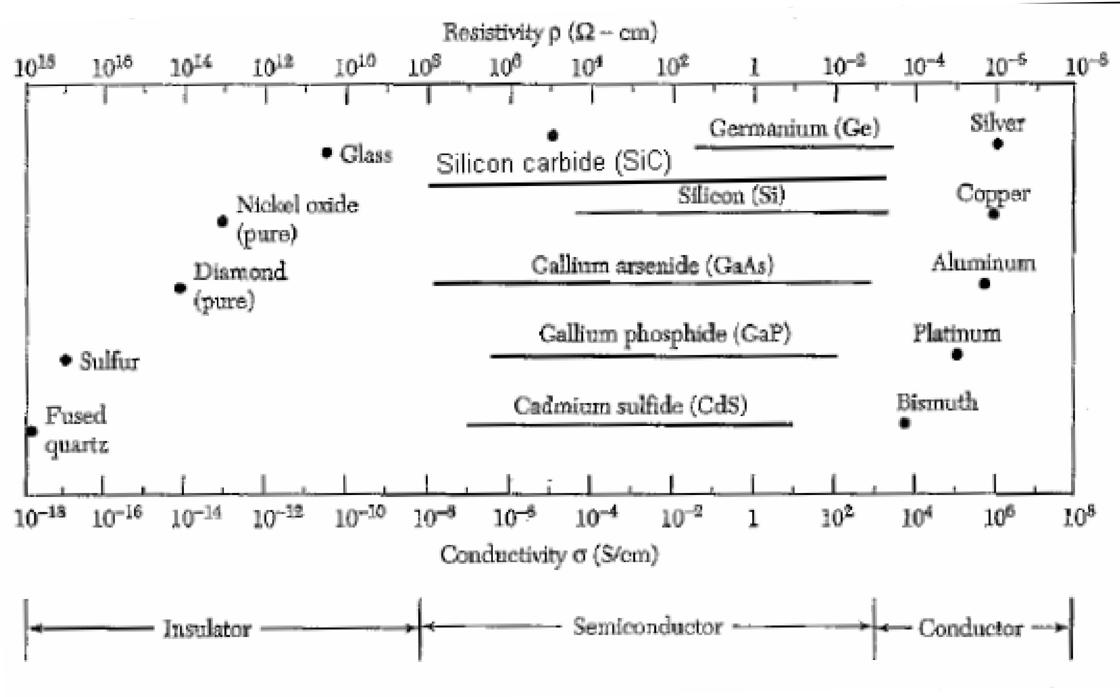

Figure 5.8 Typical range of resistivities for insulators, semiconductors and conductors.

5.3 Fabrication of PIN Diodes on Substrates with an Endolayer

To fabricate PIN diodes, a p-type dopant, aluminum was incorporated into the annealed endolayer using a KrF excimer laser (Fig. 5.9a). Trimethylaluminum was used as the precursor for the aluminum dopant atoms. The laser doping parameters are listed in Table 5.3. To compare the performance of the PIN diode to another device that does not contain the insulator region, a p-n junction was fabricated as a reference sample (Fig. 5.9b) by doping the parent n-type SiC substrate with aluminum using the same laser processing method and parameters as for the PIN diode in Fig. 5.9a. This allows evaluation of the effectiveness of the insulator region in the PIN diode.

Table 5.3 Laser processing parameters for p-type doping on the endolayer and parent substrate.

	P-type doping on endolayer (PIN Diode)	P-type doping on parent substrate (p-n junction)
Laser source	KrF excimer	KrF excimer
Wavelength (nm)	248	248
Pulse length (ns)	25	25
Pulse energy (mJ)	75	75
Laser fluence (J/cm^2)	1.5	1.5
Pulse intensity (MW/cm^2)	60	60
Pulse repetition rate (Hz)	1	1
Laser shots	300	300
Beam area (cm^2)	0.2×0.25	0.2×0.25
Ambient gas	TMA at 30 psi	TMA at 30 psi

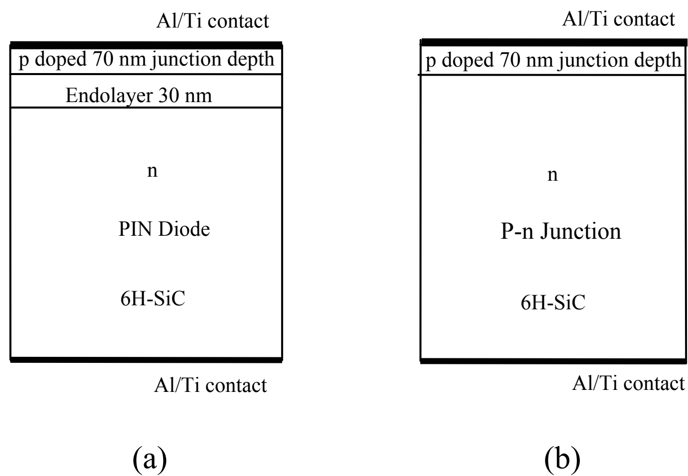

Figure 5.9 Device designs on SiC substrates with and without an endolayer: (a) PIN diode on laser-formed endolayer and (b) reference p-n junction.

Laser doping of aluminum was carried out by focusing the KrF excimer laser beam of wavelength 248 nm on the wafer segment with a beam area 2×2.5 mm^2, laser fluence 1.5 J/cm^2, repetition rate 1 Hz and laser pulses 300. The doped samples were cleaned by immersion in a KOH solution for several minutes to remove the aluminum residue formed on the wafer surface during the laser doping experiment. The laser doped regions were cut into planar diodes with a size of 1.5×1.5 mm^2. Ohmic contacts were formed by depositing Al/Ti on the top and bottom sides of the sample using an Edwards Thermal Evaporator and by annealing at 1000°C for 5 min. The I-V characteristics of the PIN diodes were measured using micromanipulators connected to a Tektronix 576 curve tracer.

Fig. 5.10 shows SIMS data for laser-doped aluminum concentration in the endolayer of a 6H-SiC substrate. The endolayer was doped to a depth of 70 nm with maximum dopant concentration 1×10^{21} atoms/cm^3. Fig. 5.11 shows the I-V characteristics of a laser-fabricated endolayer PIN diode and a reference p-n junction in parent 6H-SiC. The p-n junction exhibits the rectifying property of a typical diode with high forward current and relatively low leakage current. Considering a leakage current density of 10^{-2} A/cm^2 as a threshold, which is generally used for defining blocking voltage in standard commercial Si power devices [Singh, et al. (2002)], the breakdown voltage of the p-n junction is found to be about 13 V. The forward current of the endolayer PIN diode is much lower than that of the p-n junction because of the high resistance of the endolayer. The leakage current of the diode is also reduced compared to that of the p-n junction and the

breakdown voltage of the diode is found to be about 18 V based on the same leakage current density threshold as above.

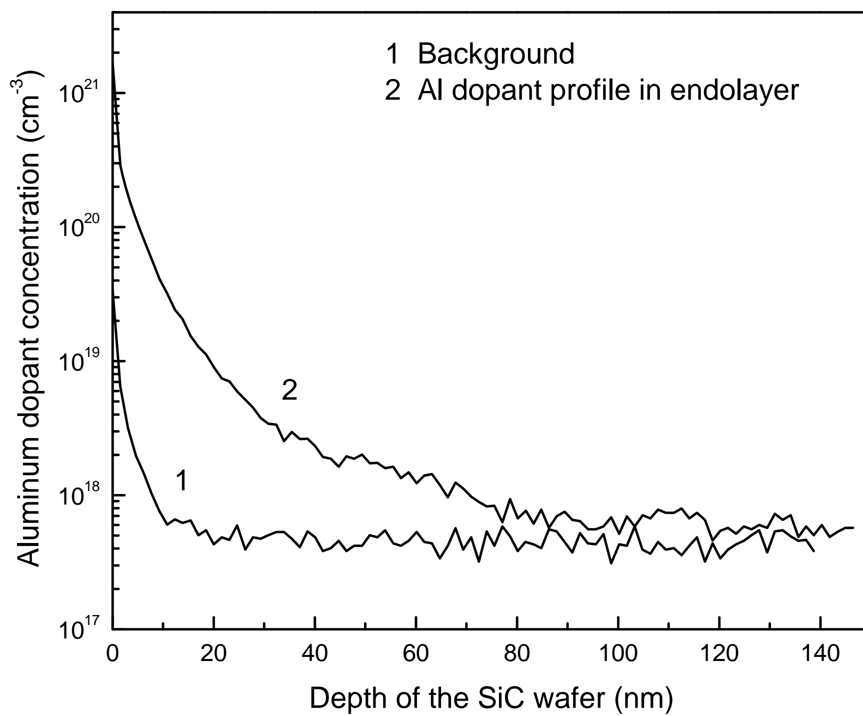

Figure 5.10 Depth profiles of aluminum concentration in the top laser-doped p region in the endolayer measured by SIMS.

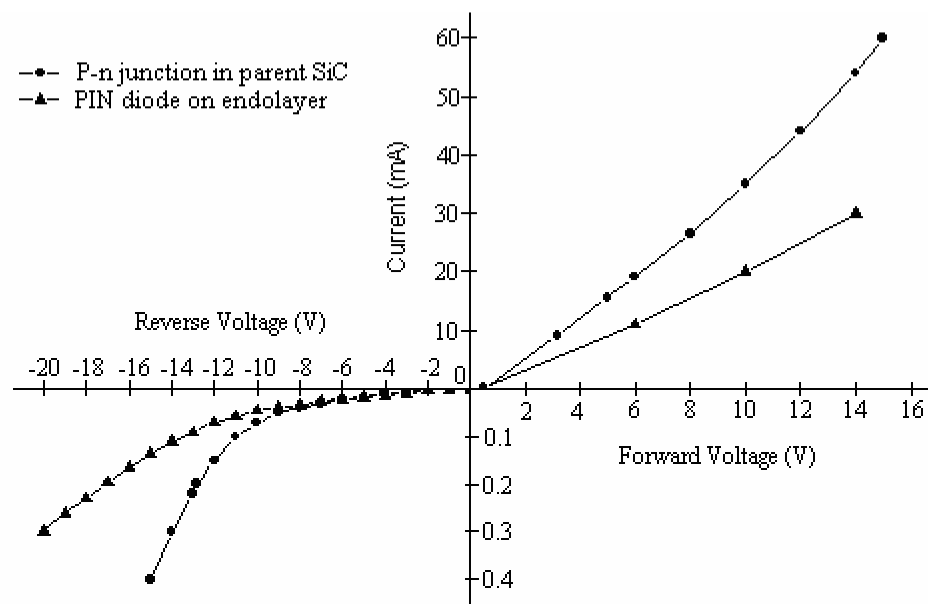

Figure 5.11 I-V characteristics of PIN diodes fabricated on an endolayer and a parent 6H-SiC.

5.4 Fabrication of PIN Diodes on Substrates with Epilayer

Prototype SiC PIN diodes with a size of 0.5×0.5 mm^2 were fabricated on n-type 4H-SiC wafer segments with a 10 μm thick epitaxial layer containing a donor concentration in the range of 8×10^{15} to 1.3×10^{16} cm^{-3}. A reference Schottky diode was also fabricated to evaluate the effect of epilayer laser doping parameters on PIN diode performance. Schematics of the diodes are presented in Fig. 5.12. Two different structures are used for the diode fabrication: (1) a laser aluminum doped top p region on the mentioned substrate (Diode A, Fig. 5.12a); (2) same laser doped top p region on the same substrate with different laser pulses (1000 and 3000 for Diodes B and C respectively) and a laser direct metallized bottom (Diode B in Fig. 5.12b and Diode C in Fig. 5.12c). The top p region was aluminum doped by using surface heating doping method, and the laser direct metallized bottom regions were fabricated using a Nd:YAG laser internal heating method, both of which have been discussed in Chapter 4. Laser processing parameters for p-type doping and laser direct metallization on the Diodes are shown in Table 5.4. Au/Pt was sputtered onto the top laser doped p^+ region of all three diodes (Diodes A, B and C) and bottom of the substrate of Diode A to create a metal thin film ohmic contact; for Diodes B and C the laser direct metallized bottom regions has been created carbon rich ohmic contacts which were contacted directly by the microprobes of the I-V measurement instruments. The reference Schottky diode (Diode D, Fig. 5.12d) was fabricated by sputtering Au/Pt on both low doped epitaxial layer surface and substrate bottom. Au/Pt sputtered on such low doped epilayer surface (8×10^{15} to 1.3×10^{16} cm^{-3}) can not form ohmic contact and only Schottky contact can be formed with the SiC

[Kassamakova 2002]. The current-voltage (I-V) characteristics of the PIN and Schottky diodes were measured by using micromanipulators connected to a Tektronix 576 curve tracer.

Au/Pd contact
p 200 nm junction depth
n^- epitaxial layer 9.8 μm
$8\times10^{15} \sim 1.3\times10^{16}$ cm^{-3}
n
Diode A
Au/Pd contact

Au/Pd contact
p 200 nm junction depth
n^- epitaxial layer 9.8 μm
$8\times10^{15} \sim 1.3\times10^{16}$ cm^{-3}
n
Diode B
Laser direct metallized contact

Au/Pd contact
p 450 nm junction depth
n^- epitaxial layer 9.55 μm
$8\times10^{15} \sim 1.3\times10^{16}$ cm^{-3}
n
Diode C
Laser direct metallized contact

Au/Pd contact
n^- epitaxial layer 10 μm
$8\times10^{15} \sim 1.3\times10^{16}$ cm^{-3}
n
Diode D
Au/Pd contact

(a) (b) (c) (d)

Figure 5.12 Cross-sectional views of the laser fabricated PIN diodes and referenced Schottky diode. (a) Diode A, with just top laser doped p region; (b) Diode B, with both top laser doped p region (200 nm junction depth) and bottom n+ region; (c) Diode C, with both top laser doped p^+/p region (450 nm junction depth) and bottom n^+ region; and (d) Diode D, reference Schottky diode.

Table 5.4 Laser processing parameters for p-type doping and laser direct metallization on the Diodes shown in Fig. 5.12.

Methods	Top p-type doping		Laser direct metallization
Sample	Diodes A and B	Diode C	Diodes B and C
Laser source	KrF excimer	KrF excimer	Nd:YAG
Wavelength (nm)	248	248	1064
Pulse repetition rate (Hz)	1	1	3000
Beam area (cm^2)	0.2×0.4	0.2×0.4	$\pi(0.03)^2/4$
Pulse energy (mJ)	120	120	3.73
Laser fluence (J/cm^2)	1.5	1.5	5.3
Pulse intensity (MW/cm^2)	60	60	73.4
Scanning speed (mm/s)	-	-	1
Irradiation passes	-	-	1
Laser pulses	1000	3000	-
Ambient gas	TMA delivered by Ar at 30 psi	TMA delivered by Ar at 30 psi	N_2 at 30 psi

The doping profiles of top p doped regions in Diodes A-C have been discussed in Section 4.3.2, in which 200 nm and 450 nm junction depths were obtained for 1000 and 3000 laser pulses respectively. The temperature distributions of SiC substrate during laser direct metallization using the parameters listed in Table 5.4 are shown in Fig. 5.13. The peak temperature of the bottom surface (3268 K) exceeds the peritectic temperature of silicon carbide (Fig. 5.13a) so the bottom surface will create a carbon rich phase after the decomposition of silicon carbide and can serve as a direct metallization layer. The transient temperature distribution along the thickness of the wafer from the bottom surface at the peak temperature (t=48ns) (Fig. 5.13b) shows that the region exceeding the decomposition temperature is about 190 nm.

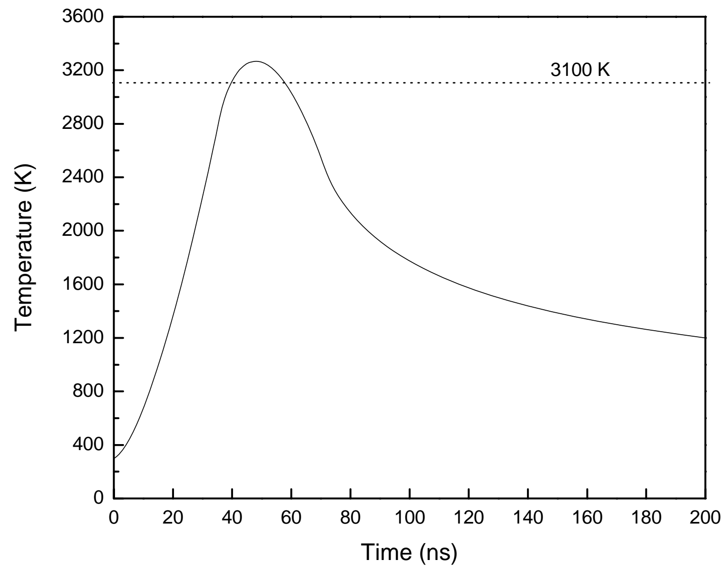

(a)

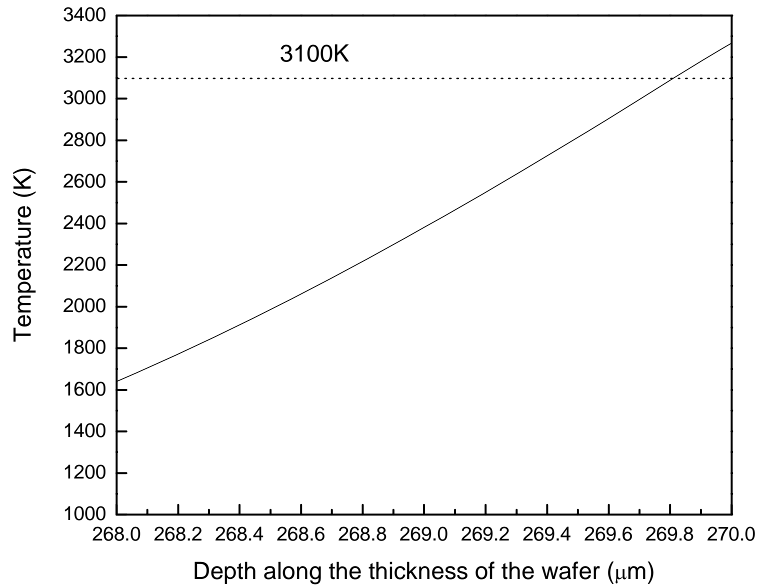

(b)

Figure 5.13 Temperature distribution of 4H-SiC during laser direct metallization using the parameters listed in Table 5.4.(a) Bottom surface temperature distribution with the time; (b) Transient temperature distribution along the thickness of the wafer from the bottom surface at the peak temperature (t=48ns).

Fig. 5.14 shows the I-V characteristics of the reference Schottky diode (Diode D) (Fig. 5.12a) and three laser fabricated diodes (Fig. 5.12b) at room temperature. Under forward current the Schottky diode reaches 100 A/cm^2 at 19 V and shows an abrupt breakdown voltage of 320 V when reverse bias is applied. Diode A exhibits a breakdown voltage of 500 V and reaches V_F of 20 V at 100 A/cm^2. The improved breakdown voltage is attributed to a new reverse leakage current mechanism. The high leakage current of the reference Schottky diode is due to majority carriers that overcome the barrier. The PIN diode suppresses the leakage current resulting from minority carriers diffusing to the depletion layer.

Diode B decreases the V_F at 100 A/cm^2 to about 13 V, and Diode C, having a deeper laser doped p junction depth, exhibits a V_F at 100 A/cm^2 of 12.5 V, indicating the effectiveness of the laser direct metallized contact. Although both possess laser doped p region and laser direct metallized layer, Diode C shows an abrupt breakdown voltage of 460 V while Diode B does not show abrupt avalanche breakdown but rather a soft breakdown, which may be due to the different dopant profiles of the p regions doped in the two diodes or the defects such as micropipes (screw dislocation) and stacking faults in the Diode B cause its soft breakdown. Using a leakage current density of $< 10^{-2}$ A/cm^2 as a threshold, which is considered acceptable for defining blocking voltage in standard commercial Si power devices [Singh, Irvine, et al. (2002)], the breakdown voltage of Diodes B is about 420 V.

The theoretical breakdown voltage of the PIN diode can be estimated by determining the drift region thickness from the basic depletion equation [Singh, et al. (2002)]:

$$W = \frac{\varepsilon_r \cdot \varepsilon_0 \cdot Ec}{q \cdot N_D} - \sqrt{[\frac{\varepsilon_r \cdot \varepsilon_0 \cdot Ec}{q \cdot N_D}]^2 - (\frac{2\varepsilon_r \cdot \varepsilon_0 \cdot V_B}{q \cdot N_D})} \tag{5.5}$$

where V_B is the breakdown voltage, W is the drift layer thickness that is taken as the epilayer thickness, q is the electronic charge, ε_r is the relative dielectric constant of SiC, i.e., $\varepsilon_r = 9.72$ [Singh (1994)], ε_0 is the permittivity of vacuum, and E_C is the critical electric field which was empirically derived by Konstaitinov [Konstantinov, et al. (1997)] relating E_C to the dopant concentration (N_D cm^{-3}) in the epilayer for 4H-SiC wafers, i.e.,

$$E_c = \frac{2.49 \times 10^6}{1 - \frac{1}{4}\log_{10}(\frac{N_D}{10^{16}})} \quad V/cm \tag{5.6}$$

Substituting Eq. (5.6) into Eq. (5.5), the following expression is obtained:

$$V_B = \frac{2.49 \times 10^6 W}{1 - \frac{1}{4}\log_{10}(\frac{N_D}{10^{16}})} - \frac{W^2 \cdot q \cdot N_D}{2\varepsilon_r \cdot \varepsilon_0} \tag{5.7}$$

Considering an average dopant concentration $N_D = 1 \times 10^{16}$ cm^{-3}, an epilayer of thickness W = 9.8 μm, the theoretical breakdown voltage of the PIN diode is 1547 V. The measured breakdown voltages of the PIN diodes are about 500 V which are approximately one third of the theoretical value. This discrepancy may be due to several reasons:

(a) Lack of proper edge termination and passivation - This can produce concentrated electric field at the corners of three-dimensional structures leading to early breakdown at the edges. An effective edge termination is expected to make the electric field distribution uniform at the edges of the device and therefore increase the breakdown voltage of the device. It has been reported that the breakdown voltages of SiC Schottky and PIN diodes

were improved significantly by different edge termination designs compared to those without edge termination [Alok, et al. (1994), Itoh, et al. (1996) and Biserica, et al. (2001)].

(b) Defects such as micropipes (screw dislocation) and stacking faults in the epilayer - The micropipes are generally aligned along the c-axis of the SiC crystal. Since our devices had a vertical structure along the thickness of the substrate, the applied electric field, which could be almost parallel to the c-axis, induces leakage current through the micropipe defects causing electrical breakdown of the PIN diode at a low voltage [Tin, et al. (1996)].

The performances of laser-fabricated PIN diodes and conventionally fabricated PIN diodes are summarized in Table 5.5. The results are comparable to the others' data considering the absence of edge termination in the laser-fabricated PIN diodes. These results indicate the promise of this novel laser direct doping and metallization technique for the fabrication of SiC PIN diodes.

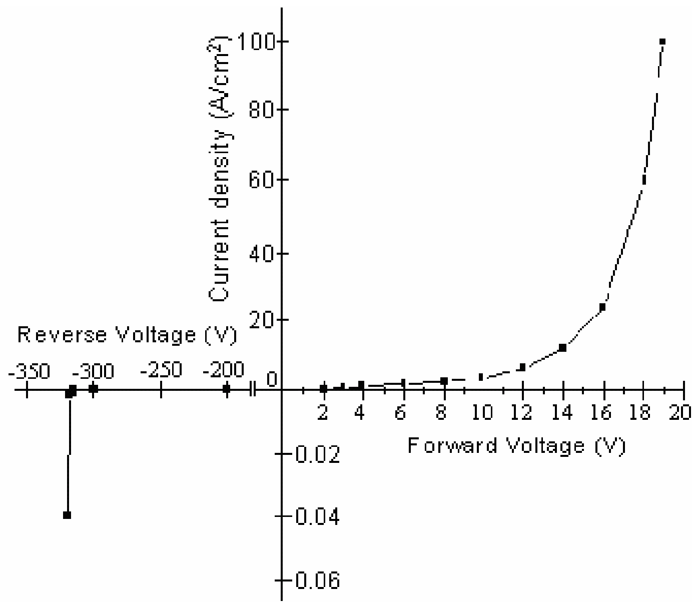

(a)

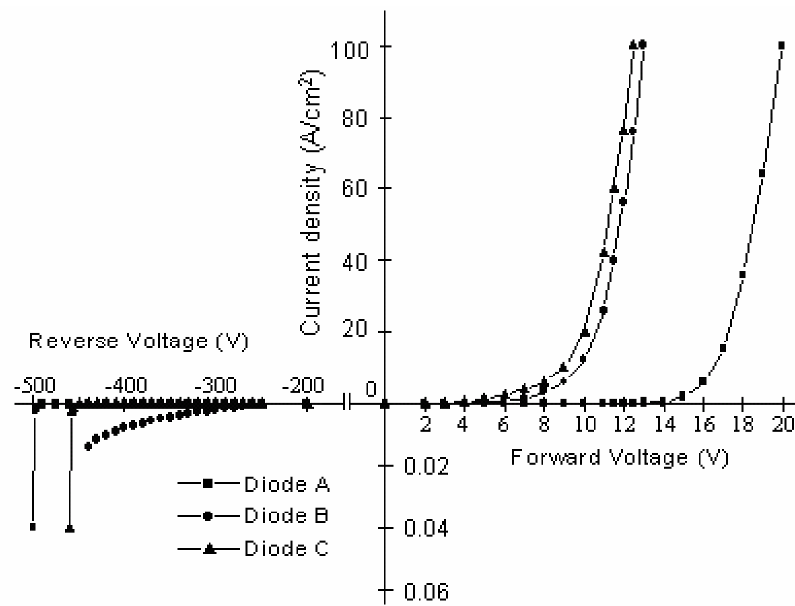

(b)

Figure 5.14 Measured Schottky diode and PIN diodes I-V curves at room temperature. (a) Schottky diode. (b) Laser fabricated PIN diodes.

Table 5.5 Comparison of the performance of the PIN diodes fabricated in the literatures and our group.

	4H-SiC [Sugawara, et al. (2001)]	6H-SiC [Fujihira, et al. (2002)]	4H-SiC [Alexandrov, et al. (2001)]	Laser fabricated PIN diode on 4H-SiC (this work)	Laser fabricated PIN diode on 6H-SiC (this work)
Fabrication method	Epitaxial growth	Epitaxial growth	Ion implantation	Laser doping	Laser doping
Epilayer thickness (μm)	200	31	30	9.55, 9.8	
Endolayer thickness (μm)					0.03
Dopant concentration in the epilayer (cm^{-3})	8×10^{13}	1×10^{15}	1×10^{15}	8×10^{15} ~ 1.3×10^{16}	
Edge termination method	JTE	none	MJTE	none	none
Breakdown Voltage (V)	19500	4200	5000	420 ~ 500	18
Ideal breakdown voltage (V_B) based on Eq. (5.7)	29700	5281	5139	1345 ~ 1668	
Forward Voltage drop at $100A/cm^2$ (V)	6.5	3.75	4.2	12.5 ~ 20	

JTE: Junction termination extension. MJTE: Multistep junction termination extension.

CHAPTER 6: LASER SYNTHESIS OF OPTICAL STRUCTURE IN SILICON CARBIDE

6.1 Introduction

Silicon carbide (SiC) is a promising semiconductor material for optical devices, particularly mirrors and lenses, because of its low thermal coefficient of expansion, hardness (and hence good polish ability), high thermal conductivity (350-490 $Wm^{-1}K^{-1}$) and chemical stability in hostile environments [Goela et al. (1991) and Heft et al. (1995)]. Rohm and Haas Company, Advanced Materials Division, and more recently, Polo Corporation (circa 2004) are developing silicon carbide as a mirror or mirror coating on beryllium. The material can be polished to less than 3 Ångstrom RMS surface finish and is resistant to wet oxygen up to 1650°C; Rohm and Haas CVD SiC has a reflectivity of greater than 41% for wavelengths 120-190 nm and 70-99% for wavelengths ranging form 10500-12000 nm [Goela et al. (1991) and Narushima et al. (1990)). The objectives of this chapter are 1) to present the laser direct write technique for fabrication of optical structures in SiC and 2) to characterize the optical properties of the optical structures created in SiC by this process.

6.2 Laser Synthesis of Embedded Optical Phases

Semi-insulating 6H-SiC with the thickness of 430 μm was used for the synthesis of embedded optical phase. The laser processing parameters are listed in Table 6.1.

Table 6.1 Laser processing parameters for the synthesis of embedded optical phases.

	C-rich phase	C-rich phase containing nitrogen	C-rich phase containing aluminum
Laser source	Nd:YAG	Nd:YAG	Nd:YAG
Wavelength (nm)	1064	1064	1064
Pulse repetition rate (kHz)	3	3	2
Beam area (cm^2)	$\pi(0.03)^2/4$	$\pi(0.03)^2/4$	$\pi(0.03)^2/4$
Pulse energy (mJ)	4.7	4.7	5.5
Laser fluence (J/cm^2)	6.65	6.65	7.75
Pulse intensity (MW/cm^2)	92.3	92.3	118
Scanning speed (mm/s)	1	1	1
Irradiation passes	1	1	1
Ambient gas	Ar at 30 psi	N_2 at 30 psi	TMA delivered by Ar at 30 psi

The incident focused laser beam is transmitted through the top surface of the 6H-SiC wafer and most of the laser energy are absorbed by the unpolished bottom surface, as shown in Fig. 6.1. Since the pulse intensities of all these three cases are higher than the critical pulse intensity for decomposition of SiC shown in Fig. 2.6, carbon rich phase can form from the bottom surface toward the bulk [Salama (2003)]. This is a direct write process. Optical interferometry roughness measurements showed no deterioration in surface roughness of the embedded optical phase (e.g., a reflector) after this mode of laser processing; consequently, no post anneal was required [Salama et al. (2002)]. The fact that the width of the laser written reflector is smaller than the diameter of the incident focused laser beam is surprising and is not anticipated by Snell's Law. A plausible explanation is the activation of nonlinear absorption, which leads to the onset of a self-focusing effect in SiC wafers on the order of 430 μm thick [Salama (2003)]. An optical carbon rich phase embedded in a polished single crystalline 6H-SiC substrate is shown in Fig. 6.2.

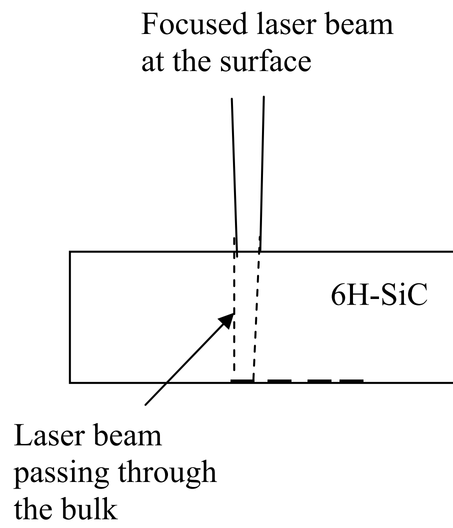

Figure 6.1 Fabrication of an embedded optical structure.

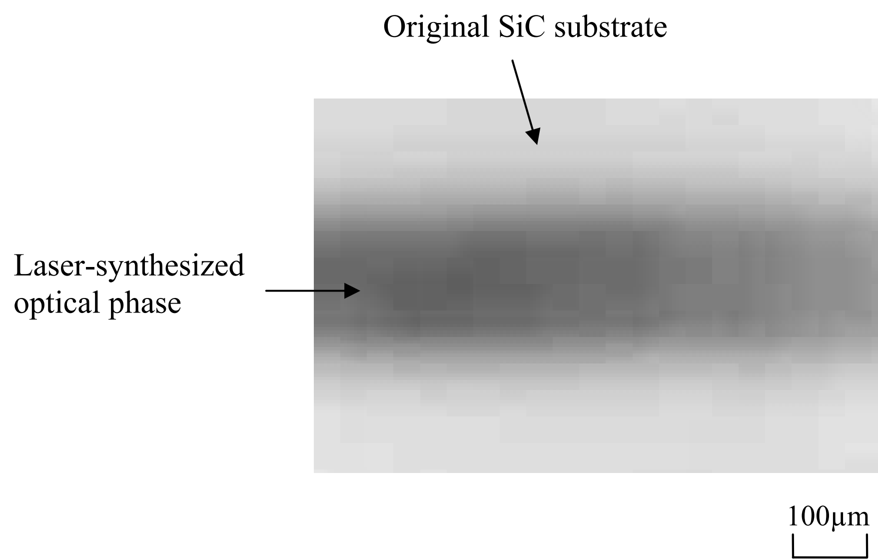

Figure 6.2 Silicon carbide substrate showing an embedded optical structure.

6.3 Optical Property Modification

Such embedded laser-synthesized optical phase was tested for reflectivity using a green laser (wavelength, $\lambda = 532$ nm). The reflectivity of both the laser-synthesized and parent silicon carbide substrate were found to be 16% and 10% respectively. This is a reflectance increase of 60% for 532 nm wavelength irradiation, at room temperature. These promising results led to a literature search on SiC reflectivity. Epitaxial SiC surfaces (epilayers) have been observed [Goela et al. (1991)] to provide sufficient reflectivity for signal processing. Our preliminary laser synthesized optical structures yield comparable results.

In this present study the reflectivity and transmission of the laser synthesized embedded structures were calculated based on the transmitted (P_T) and reflected (P_R) powers measured at a laser wavelength of 1064 nm, whose set-up is illustrated in Fig. 6.3. The transmitted and reflected powers are measured using detector #1 and detector #2 respectively.

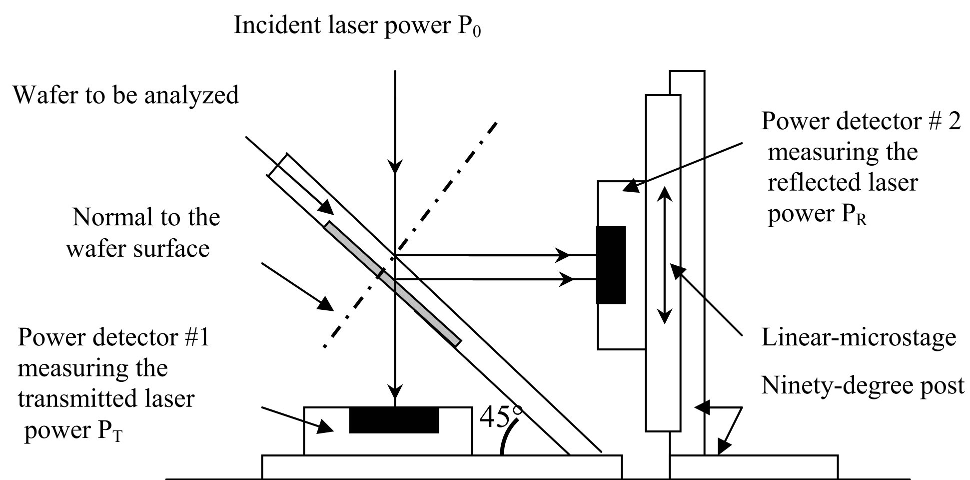

Figure 6.3 Experimental set-up for measuring the reflectivity and transmission of laser synthesized optical structures at particular wavelength.

The absorption coefficient of the original wafer η is first determined from the following equation:

$$P_T = P_0(1-R)e^{-\eta d'} \quad (6.1)$$

where P_0 is the incident laser power, P_R is the reflected laser power, R is the reflectivity of the parent wafer and d is the distance the laser beam travels in the wafer. d' is calculated using Snell's Law.

The reflectivity of the laser synthesized structure R_L is calculated from the following equation:

$$P_0 R + P_0(1-R)R_L e^{-2\eta d^*} = P_R \quad (6.2)$$

where d* is the distance that the laser beam travels from the beam incident side of the wafer to the top of the embedded structure.

The transmission, T_L, of an embedded structure is obtained from the following equation:

$$T_L = P_T / [P_0(1-R)e^{-\eta d^*}] \quad (6.3)$$

where P_T is the transmitted laser power.

The measurement data of P_0, P_R and P_T and the calculated results of R_L and T_L for all the samples are listed in Table 6.2.

Table 6.2 Reflectivity and transmission calculation of laser synthesized optical structure

	Parent wafer	C rich phase	C rich phase containing N_2	C rich phase containing Al
P_0 (mW)	1000	1000	1000	1000
P_R (mW)	368	327	329	332
P_T (mW)	390	53.3	51.0	56.0
η (cm^{-1})	6.07	-	-	-
d (μm)*	430	430	430	430
d' (μm)	450	450	450	450
d^* (μm)	~ 450	~ 450	~ 450	~ 450
R_L (%)	20	27.3	27.7	28.2
T_L (%)	60.5**	8.7	8.4	9.2

* d: Thickness of the original SiC substrate.

** Obtained from double face polished semi-insulating 6H-SiC wafer with the thickness of 430 μm.

The calculated absorption coefficient of parent 6H-SiC, 6.07 cm^{-1} corresponds with the data given in the reference [Goldberg et al (2001)]. The reflectivity of laser synthesized embedded optical structures are increased by 40%; the parent wafer has a reflectivity of 20% and that for the laser synthesized structures are about 28% as shown in Fig. 6.4. Accordingly the transmission of the laser synthesized optical structures decrease to about 9% compares to 60.5% of the parent wafer (Fig. 6.5).

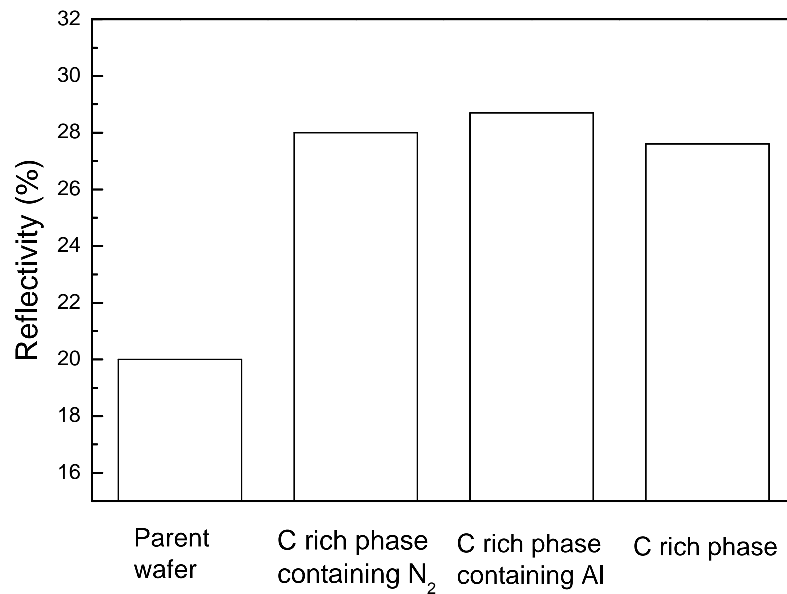

Figure 6.4 Reflectivity of parent wafer, C rich phase, C rich phase containing N_2 and C rich phase containing Al measured at 1064 nm.

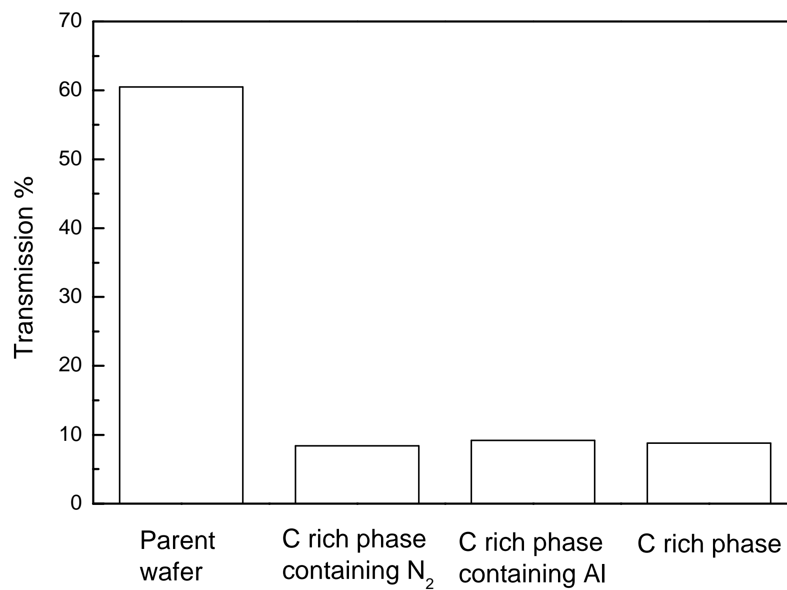

Figure 6.5 Transmission of parent wafer, C rich phase, C rich phase containing N_2 and C rich phase containing Al measured at 1064 nm.

CHAPTER 7: SUMMARY

7.1 Conclusions

A novel laser direct metallization and doping technique is provided to direct metallize the surface of silicon carbide without metal deposition and dope silicon carbide without high temperature annealing in order to overcome some barriers in metallization and doping during the fabrication of silicon carbide devices.

Laser irradiation of silicon carbide in a dopant-containing ambient allows to simultaneously heating the silicon carbide surface and incorporating dopant atoms into the silicon carbide lattice. Nitrogen and Trimethyaluminum (TMA) are used as dopants to produce n-type and p-type doped silicon carbide, respectively. Two laser doping methods are presented in this dissertation. i) Internal heating: Nd:YAG laser beam (λ=1064nm) irradiates on the top polished surface of the silicon carbide wafer, but passing through the bulk wafer, reaching the unpolished bottom surface and dopants are incorporated from the bottom surface; ii): Excimer laser is used to irradiate the top surface of silicon carbide wafer and dope the dopants simultaneously.

Laser internal heating doping method created a 800 nm n-type doped junction with a high surface dopant concentration of 1×10^{21} cm^{-3} decreasing to 1.5×10^{19} cm^{-3} at the junction and a 800 nm p-type doped junction with a surface dopant concentration of 5×10^{20} cm^{-3}

decreasing to 1.5×10^{18} cm^{-3} at the junction based on laser enhanced solid phase diffusion. Laser surface heating method produced p- type dopant depths of 200 nm and 450 nm for different numbers of laser pulses. For both types of lasers two diffusion regions, near-surface region and far-surface region, were identified and two different diffusion mechanisms are dominant in these two regions. The diffusion of dopant atoms into the bulk silicon carbide can be explained by considering the laser-enhanced substitutional and interstitial diffusion mechanisms. In the near-surface region, the dopant atoms can easily diffuse into the bulk by occupying the vacancies created during the laser irradiation process as well as interstitial sites. In the far-surface region the diffusion process is dominated by the highly mobile interstitials. The effective diffusion coefficients of nitrogen are 2.4×10^{-5} cm^2/s for near-surface region and 9.2×10^{-6} cm^2/s for far-surface region; and those of aluminum are 1.2×10^{-5} cm^2/s for near-surface region and 1.3×10^{-6} cm^2/s for far-surface. These values are 6 orders of magnitude higher than the typical values of the diffusivity of nitrogen and aluminum in SiC. This indicates that laser doping process enhances the diffusivity of dopants significantly.

Laser direct metallization can be realized on the surface of silicon carbide by generating metal-like conductive phases due to the decomposition of silicon carbide. The laser metallized contact can act as ohmic contact and it has been successfully used in the fabrication of silicon carbide PIN diodes. Combination of laser direct metallization with laser doping, i.e., fabricating laser direct metallized contacts on laser heavily doped SiC substrate can dramatically improve the performance of such ohmic contact.

A pulsed laser-induced endolayer was fabricated on an n-type 6H-SiC substrate by incorporating carbon based on laser solid-phase diffusion. Carbon atoms can be incorporated into the top layer of silicon carbide substrates by excimer laser irradiation using methane as a precursor. XEDS analysis shows the endolayer thickness to be 100 nm. TEM images show that there is no amorphization during the laser endotaxy process and that the lattice structure of the endolayer remains undistorted compared to that of the parent wafer, indicating the crystalline integrity of the endotaxy process. Rutherford backscattering studies also show no amorphization and evident lattice disorder occur during this laser solid phase diffusion process. In this study, the resistivity of the endolayer is 1.1×10^5 Ω·cm before annealing and 9.4×10^4 Ω·cm after annealing at 1000°C for 10 min, which are high enough for many applications such as device isolation.

Prototype silicon carbide PIN diodes have been fabricated on different silicon carbide mediums, laser fabricated endolayer and parent epilayer on silicon carbide substrate, using this laser doping technique and/or laser direct metallization. Results show that the PIN diode fabricated on a 30 nm thick endolayer can block 18 V. High breakdown voltages (420 ~ 500 V) and forward voltages drop at 100A/cm^2 (12.5 ~ 20 V) have been reached by laser doping and/or direct metallization fabricated PIN diodes on 4H-SiC with a low doped homoepilayer, showing the effectiveness of the laser direct metallized contact and the promise of this laser doping and direct metallization technique for the fabrication of SiC PIN diodes compared to the PIN diodes fabricated by other techniques such as epitaxial growth and ion implantation.

Embedded optical structures were also synthesized based on this laser direct metallization technique. The increase of 40% reflectivity of the laser synthesized optical structures compared to the parent wafer shows potential for the creation of optical, electro-optical, opto-electrical, sensor devices and other integrated structures that are stable in high temperature, high-pressure, corrosive environments and deep space applications.

7.2 Future Work

1) Experimental design for a dopant precursor delivery system that accounts for the pyrophoric, and moisture sensitivity nature of some of the precursors such as trimethylaluminum (TMAl) to control precisely the amount of dopant each fill and allows the addition of more TMAl to the bubbler without exposure to the atmospheric moisture.

2) Transmission electron microscopy (TEM) and high resolution scanning electron microscope (SEM) investigations should be utilized to study: (i) the crystal structure of the laser-fabricated metal-like contacts. (ii)The orientation relationship between the contact layer and the original wafer. (iii) The lattice defects at the interface between the laser generated-track and the original Epilayer. (iv) Structural and compositional analysis at the interfaces between laser doped, laser-metallized regions and the SiC wafer.

3) Investigating the impact of extended high temperature exposure in various ambients on the stability of the laser generated contacts and diodes, endotaxial layers and optical structures.

4) Dynamic characteristic of laser fabricated PIN diodes. More application of laser direct metallization and doping technique on fabrication of silicon carbide devices such as LED and optical filter.

5) Effect of laser induced vacancies on the diffusion coefficient. Mechanisms and Characterization of laser induced vacancies.

REFERENCES

Alexandrov, P., Tone, K., Luo, Y., Zhao, J.H., Burke T., Pan M. and Weiner, M. (2001), Electronics Letters, Vol. 37, pp. 531.

Alok, D., Baliga, B. J. and McLarty, P. K. (1994), A simple edge termination for silicon carbide devices with nearly ideal breakdown voltage, IEEE Electron Device Letters, 15, pp. 394-395.

Bäuerle, D. (2000), Laser Processing and Chemistry, 3rd. Edition, Springer-Verlag, Berlin. pp. 103-107, 117-135.

Biserica, O., Godignon, P., Brezeanu, G., Badila M. and Rebollo, J. (2001), Design of a reliable planar edge termination for SiC power devices, 2001 International Semiconductor Conference. CAS 2001 Proceedings, Vol 2, pp. 353-356.

Bonchik, A. Yu., Kijak, S. G., Gotra, Z. and Proszak, W. (2001), Laser technology for submicron-doped layers formation in semiconductors, Optics & Laser Technology, Vol. 33, pp. 589-591.

Boulmer, J., Dragnea, B., Guedj, C., Debarre, D., Bosseboeuf, A., Finkman, E. and Bourguignon, B. (1998), Laser-induced structural or compositional modifications of Si or IV-IV surface: planarization, pulsed laser induced epitaxy, carbon incorporation, and chemical etching Proceedings of the SPIE - The International Society for Optical Engineering, V. 3404, pp. 149-158.

Boulmer, J. ; Boucaud, P.; Guedj, C.; Debarre, D.; Bouchier, D.; Finkman, E.; Prawer, S.; Nugent, K.; Desmur-Larre, A.; Godet, C. and Cabarrocas, P. R. (1995),

Realization of $Si_{1-x-y}Ge_xC_y/Si$ heterostructures by pulsed laser induced epitaxy of C implanted pseudomorphic SiGe films and of a-SiGeC:H films deposited on Si(100), Journal of Crystal Growth, V. 157, pp. 436-441.

Bourdelle, K. K., Chechenin, N. G., Akhmanov, A. S.. Poroikov, A. Y. and Suvorov, A. V. (1990), Melting and damage production in silicon carbide under pulse laser irradiation, Physica Status Solidi A, Vol. 121, pp. 399-406.

Brown, W. L. (1983), Laser processing of semiconductors, in Laser Materials Processing, edited by Bass M., North-Holland Publishing Company, Amsterdam, pp. 337-406.

Canut, B., Ramos, S., Roger, J. –A., Chante, J. –P., Locatelli, M. –L. and Planson, D. (1997), Mater. Sci. Eng. B 46, 267

Carey, P. G., Weiner K. H. and Sigmon, T. W. (1988), A shallow junction submicrometer PMOS process without high-temperature anneals, IEEE Electron Device Letters,. Vol. 9, No. 10, pp. 542-544.

Casady, J. B. and Johnson, R. W. (1996), Status of silicon carbide (SiC) as a wide-bandgap semiconductor for high-temperature applications: a review, Solid-State Electronics, Vol. 39, pp. 1409-1422.

Chelnokov, V. E., Strel'chuk, A. M., Ivanov, P. A., Lentz G. and Parniere C. (1994), in Proceedings of the 6th International Symposium on Power Semiconductor Devices and ICs, pp.253 - 256

Chen, I. and Lee S. (1983), Transient temperature profiles in solids heated with a scanning laser, Journal of Applied Physics, Vol. 54, pp.1062-1066.

Chou, S. Y., Chang, Y., Weiner, K. H., Sigmon, T. W. and Parsons, J. D. (1990), Annealing of implantation damage and redistribution of impurities in SiC using a pulsed excimer laser, Applied Physics Letter, Vol. 56(6), pp. 530-532.

Cline, H. E. and Anthony, T. R. (1977), Heat treating and melting material with a scanning laser or electron beam, Journal of Applied Physics, Vol. 48, pp. 3895,-3900.

Conde, J. C., Lusquiňos, F., González, P., León, B. and Pérez-Amor, M. (2002), Temperature distribution in a material heated by laser radiation: modeling and application, Vacuum, Vol. 64, pp. 359-366.

Constantinidis, G. (1997), Processing technologies for SiC, CAS '97 Proceedings., 1997 International Semiconductor Conference, Vol.1, pp. 161-170.

Dutto, C., Fogarassy, E., Mathiot, D., Muller, D., Kern, P. and Ballutaud, D. (2003), Long-pulse duration excimer laser annealing of Al^+ ion implanted 4H-SiC for pn junction formation, Applied Surface Science, Vol. 208-209, pp. 292-297.

Dutto, C., Fogarassy, E. and Mathiot, D (2001), Numerical and experimental analysis of pulsed excimer laser processing of silicon carbide, Applied Surface Science, Vol. 184, pp. 362-366.

Edwards, A., Dwight, D. N., Rao, M. V., Ridgway, M.C., Kelner, G., and Papanicolaou, N. (1997), Compensation implants in 6H-SiC, Journal of Applied Physcis, Vol 82 (9), pp. 4223-4227.

Emorhokpor, E., Kerr, T., Zwieback, I., Elkington, W., Dudley, M., Anderson, T. and Chen, J. (2004), Materials Research Society Symposium Proceedings, Vol.815, pp.J5.19.1.

Eryu, O., Aoyama, K., Abe, K. and Nakashima, K. (2001), Impurity activation in N^+ ion-implanted 6H-SiC with pulsed laser annealing method, Materials Research Society Symposium Proceedings, Vol. 640, pp. H5.31.1-H5.31.6.

Eryu, O., Kume, T., Nakashima, K., Nakata, T. and Inoue, M. (1997), Formation of an ohmic electrode in SiC using a pulsed laser irradiation method, Nuclear Instruments and Methods in Physics Research B, Vol 121, pp. 419-421.

Eryu, O., Okuyama, Y., Nakashima, K., Nakata, T. and Watanabe, M. (1995), Formation of a p-n junction in silicon carbide by aluminum doping at room temperature using a pulsed laser doping method, Applied Physics Letter, Vol 67 (14), pp. 2052-2053.

Fissel, A., Kaiser, U., Ducke, E., Schröter, B. and Richter, W. (1995), Epitaxial growth of SiC thin films on Si-stabilized α-SiC (0001) at low temperatures by solid-source molecular beam epitaxy, Journal of Crystal Growth, Vol. 154, pp. 72-80.

Fujihira, K., Tamura, S., Kimoto T. and Matsunami, H. (2002), Low-loss, high-voltage 6H-SiC epitaxial p-i-n diode, IEEE Transactions on electron device, Vol.49, No.1, pp.150-154.

Fukada, S., Nakamura N., Monden, J. and Nishikawa, M. (2004), Experimental study of cracking methane by Ni/SiO_2 catalyst**,** Journal of Nuclear Materials, 329-333, 1365-1369.

Gadiyak, G. V. (1998), Theoretical model and computer simulation results of enhanced diffusion of high-temperature implanted aluminum in silicon carbide, Nuclear Instruments and Methods in Physics Research B, Vol.142, pp. 313-318.

Gamo, K., Murakami, K., Kawabe, M., Namba, S., and Aoyagi, Y. (1981), in Laser and Electron Beam Solid Interactions and Materials Processing, eds,, Gibbons J.F., Hess, L.D. and Sigmon, T. W. (North-Holland, Amsterdam), pp. 97.

Giust, G. K. and Sigmon, T.W. (1997), Self-aligned aluminum top-gate polysilicon thin-film transistors fabricated using laser recrystallization and gas-immersion laser doping, IEEE Electron Device Letters, Vol.18 No. 8, pp. 394-396.

Goela, J. S., Pickering, M. A., Taylor, R. L. , Murray B. W. and Lompado, A. (1991) Applied Optics, **30,** 3166.

Goldberg Y, Levinshtein M, and Rumyantsev S (2001), Silicon Carbide (SiC), in: Levinshtein ME, Rumayantsev SL and Shur MS, editors. Properties of Advanced Semiconductor Materials, 1st Edition, New York: John Wiley & Sons, pp. 93-147.

Handy, E. M., Row, M. V., Holland, O. W., Chi, P. H., Jones, K. A., Derenge, M. A., Vispute, R. D. and Venkatesen, T. (2000), Al, B, and Ga ion-implantation doping of SiC, Journal of Electronic Materials, Vol. 29, No. 11, p. 1340-1345

Harris, G. H. (1995), Properties of Silicon Carbide, Emis DATAREVIEW series No.13, inspect publication, Exeter, England.

Heft, E. Wendler, T. Bachmann, Glaser, E.and Wesch, W. (1995), Defect production and annealing in ion implanted silicon carbide, Materials Science and Engineering, B 29, pp. 142-146.

Itoh, A., Kimoto T. and Matsunami, H. (1996), Excellent reverse blocking characteristics of high-voltage 4H-SiC Schottky rectifiers with boron-implanted edge termination, IEEE Electron Device Letters, 17, 139-141.

Jones, E. C. and Ishida, E. (1998), Shallow junction doping technologies for ULSI, Materials Science and Engineering R, Vol. 24, pp. 1-80.

Kaneda, S., Sakamoto, Y., Mihara, T., and Tanaka, T. (1987), Journal of Crystal Growth, Vol. 81, pp. 536.

Kar, A., Scott, J. E. and Latham, W. P. (1996), Effects of mode structure on three-dimensional laser heating due to single or multiple rectangular laser beams, Journal of Applied Physics, Vol. 80, pp. 667-674.

Karmann, S., Suttrop, W., Schöner, A., Schadt, M., Haberstroh, C., Engelbrecht, F., Helbig, R., Pensl, G., Stein, R. A.and Leibenzeder, S. (1992),Chemical vapor deposition and characterization of undoped and nitrogen-doped single crystalline 6H-SiC, Journal of Applied Physics, Vol. 72, pp. 5437-5442.

Kempshall, B. W., Giannuzzi, L. A., Prenitzer, B. I., Stevie F. A. and Da, S. X. (2002), Comparative evaluation of protective coatings and focused ion beam chemical vapor deposition processes, X. Journal of Vacuum Science Technology. B20, pp. 286-290.

Kern, R. S., Jarrendahl, K., Tanaka, S. and Davis, R. F. (1997), Homoepitaxial SiC growth by molecular beam epitaxy, Physica Status Solidi (b), Vol. 202, pp. 379-404.

Kerrien, G., Hernandez, M., Laviron, C., Sarnet, T., Debarre, D., Noguchi, T., Zahorski, D., Venturini, J., Semeria, M. N. and Boulmer, J. (2003), Optical characterization of laser processed ultra-shallow junctions, Applied Surface Science, Vol. 208-209, pp. 277-284.

Kerrien, G., Sarnet, T., Debarre, D., Boulmer, J., Hernandez, M., Laviron, C., Semeria, M. N. (2004), Gas immersion laser doping (GILD) for ultra-shallow junction formation, Thin Solid Films, Vol. 453-454, pp. 106-109.

Kimerling, L. C. and Benton J. L. (1980), Defects in Laser-Processed Semiconductors. In: White CW, Peercy PS, editors. Laser and Electron Beam Processing of Materials, Academic, London, pp.385.

Kimto, T., Itoh, A. and Matsunami, H. (1997), Step-controlled epitaxial growth of high-quality SiC layers, Physica Status Solidi, Vol. 202, pp. 247-260.

Konstantinov, A. O., Wahab, Q., Nordell N. and Lindefelt, U. (1997), Ionization rates and critical fields in 4H silicon carbide, Applied Physics Letter, 71, pp. 90-92.

Kramer, K.M. and Thompson, M.O. (1996), Pulsed laser induced epitaxial crystallization of carbon-silicon alloys, Journal of Applied Physics, V. 79, pp. 4118-4123.

Lipp, S., Frey, L., Lehrer, C., Frank, B., Demm E. and Ryssel, H. (1996), Investigations on the topology of structures milled and etched by focused ion beams, Journal of Vacuum Science Technology B14, pp. 3996-3999.

Levinshtein, M. E., Rumayantsev S. L. and Shur M. S. (2001), Properties of Advanced Semiconductor materials, 1st Edition, John Wiley & Sons, New York, pp. 93.

Mahajan, S. and Sree Harsha, K. S. (1999), Principles of growth and processing of semiconductors, McGraw-Hill Series in Materials Science and Engineering, Boston, pp. 223-224.

Mazhukin, V. I., Smurov, I. and Flamant, G. (1995), Overheated metastable states in pulsed laser action on ceramics, Journal of Applied Physics, Vol. 78, pp. 1259-1270.

Mazumder J. and Kar, A. (1995), Theory and Application of Laser Chemical Vapor Deposition, Plenum Press, New York. pp158.

Mohammad, F. A., Cao, Y. and Porter, L. M. (2005), Ohmic contacts to silicon carbide determined by changes in the surface, Applied Physics Letters, Vol. 87, pp. 161908-1-161908-3.

Musumeci, P., Calcagno, L., Grimaldi, M.G. and Foti, G. (1996), Nuclear Instruments and Methods. in Physics. Res. B Vol. 116, pp. 327.

Nadella, R.K and Capano, M.A. (1997), High-resistance layers in n-type 4H-silicon carbide by hydrogen ion implantation, Applied Physics Letter, V. 70(7), pp. 886-888.

Narushima, T.et al (1990), High-Temperature Oxidation of Chemical Vapor-Deposited Silicon Carbide in Wet Oxygen at 1823-1923 K, Journal of American Ceramic Society, Vol 73, pp. 3580-3584.

Neudeck, P. G. (2000), SiC Technology, VLSI Handbook, The Electrical Engineering Hand Book Series, W. K. Chen, Ed. CRC press and IEEE press, Florida. pp. 6.1-6.24.

Nordell, N. (2002), Bulk and epitaxial growth of SiC, in Process Technology for Silicon Carbide Devices, edited by Carl-Mikael Zetterling, INSPEC, the Institution of Electrical Engineers, London, pp.13-50.

Obreja, V. and Nuttall, K. (2002), Semiconductor Conference, 2002. CAS 2002 Proceedings. International , V2 , pp. 253.

Obreja, V. (2002), IEEE Transactions on Electron Device. 49 (1), pp. 155.

Pankove, J. I. (1999), GaN: from fundamental to applications, Materials Science and Engineering B, Vol. 61-62, pp. 305-309.

Pantano, C. G. (1986), ASM Handbook Vol 10: Materials Characterization, ASM International, USA, pp. 610.

Pearton, S. J. (2000), Processing of Wide Band Gap Semiconductors, 1 st. Edition William Andrew publishing, New York.

Pensel, G., and Choyke, A. D. (1993), Electrical and optical characterization of silicon carbide, Physica B: Condensed Matter, Vol. 185, pp.264-183.

Pokhmurska, A., Bonchik, O., Kiyak, S., Savitski G.and Gloskovsky A. (2000), Laser doping in Si, InP and GaAs, Applied Surface Science, Vol. 154-155, pp. 712-715.

Porter, L., Davis, R. (1995), A critical review of ohmic and rectifying contacts for silicon carbide. Materials Science & Engineering, B: Solid-State Materials for Advanced Technology Vol. 34, No.(2-3), pp. 83-105

Quirk, M. and Serda, J. (2001), Semiconductor manufacturing technology, Prentice Hall.

Roccaforte, F., Via, F.L., Raineri, V., Pierobon, R.and Zanon E. (2003), Richardson's constant in inhomogeneous silicon carbide schottky contacts, Journal of Applied Physics, Vol. 93, pp. 9137-9144.

Rupp, R., Lanig, P., Völkl, J. and Stephani, D. (1995) First results on silicon carbide vapour phase epitaxy growth in a new type of vertical low pressure chemical vapour deposition reactor, Journal of Crystal Growth, Vol. 146, 37-41.

Salama, I. A. (2003), Laser doping and metallization of wide bandgap materials: SiC, GaN and AlN, Ph.D. Dissertation, University of Central Florida, Spring 2003.

Salama, I. A., Quick, N. R., Kar, A. (2002), Laser-fabricated metal-semiconductor junctions on silicon carbide substrates, Proceedings of 21st International Congress on Application of Lasers & Electro-Optics. pp.

Salama, I. A., Quick, N. R., Kar, A. (2003), Laser direct-metallization of silicon carbide without metal deposition, Materials Research Society Symposium Proceedings, Vol764, 75.

Salama, I. A., Middleton, C. F., Quick, N. R., Boreman, G. D. and Kar, A. (2003), Symp. Nitride and Wide Bandgap Semiconductors for Sensors, Photonics and Electronics IV, 204th meeting of the Electrochemical Society, Orlando, Florida, October 12-16.

Salama, I. A., Quick, N. R., Kar, A. (2004), Laser direct writing and doping of diamond-like carbon, polycrystalline diamond, and single crystal silicon carbide, Journal of Laser Applications, Vol. 16, No. 2, pp. 92-99.

Scace, R. I. and Slack, G. A.(1959), Journal of physical Chemistry, Vol 30, pp.1551.

Schneider H. G. and Ruth V. (1976), Advances in Epitaxy and Endotaxy: Selected chemical problems, Elsevier Scientific Publishing Company, New York, pp. 23-78.

Schöner, A. (2002), Ion implantation and diffusion in SiC, in Process Technology for Silicon Carbide Devices, edited by Carl-Mikael Zetterling, INSPEC, the Institution of Electrical Engineers, London, pp. 51-84.

Schubert, E. F, (1993), Doping in III-V Semiconductors, Cambridge University Press, Great British, pp. 354-391.

Sengupta, D. K., Quick, N. R. and Kar, A. (2001), Laser conversion of electrical properties for silicon carbide device applications, Journal of Laser Applications, Vol.13, No. 1, pp. 26-31.

Shalish, I. and Shapira, Y. (2000), Stability of schottky contacts with Ta-Si-N amorphous diffusion barriers and overlayers on 6H-SiC, Journal of Vacuum Science and Technology B, Vol.18, No.5, pp. 2477-2481.

Sharma, P. K., Rapp D. and Rahotgi N. K., (1999), Methane pyrolysis and disposing off resulting carbon, (presented at In Situ Resource Utilization (ISRU III) Technical Interchange Meeting, Denver, CO, 11-12 February 1999).

Singh, J. (2001), Semiconductor devices: basic principles, John Wiley & Sons Inc., New York. pp. 146-149.

Singh, J. (1994), Semiconductor devices: an introduction, McGraw-Hill, New York, pp. 1.

Singh, R., Cooper, J. A., Melloch, M.R., Chow T. P. and Palmour, J.W. (2002), SiC power schottky and PIN diodes, IEEE Transactions on electron device, Vol.49, No.4, pp. 665-672.

Singh, R., Irvine, K. G., Capell, D. C., Richmond, J. T., Berning, D., Hefner A. R. and Palmour J. W. (2002), IEEE Transactions on electron device, Vol. 49 p. 2308.

Solanki, R., Sudarsan, U. and Johnson, J. C. (1988), Laser-induced homoepitaxy of GaP, Applied physics letter, V. 52 (11), pp. 919-921.

Speight, J. G. (2003), Perry's Standard Tables and Formulas for Chemical Engineers, McGRAW-HILL, New York. pp33.

Stringfellow, G. B. (1999), Organametallic Vapor-Phase Epitaxy: Theory and Practice, Academic Press, San Diego, pp. 1-16.

Sugawara, Y., Takayama, D., Asano, K., Singh, R., Palmour, J. and Hayashi, T. (2001), 12-19 kV 4H-SiC pin diodes with low power loss, Procedings of 2001 International Sysposium on Power Semiconductor Devices & ICs, Osaka, pp. 27-30.

Sze, S.M. (1981), Physics of Semiconductor Devices, John Wiley & Sons, New York, pp.850.

Sze, S. M. (2001), Semiconductor devices, physics and technology, John Wiley & Sons, New York, pp. 18.

Tajima, Y., Kijima, K., and Kingery, W. D. (1982), Diffusion of ion implanted aluminum in silicon carbide, Journal of Chemical Physics, Vol 77, pp. 2592-2598.

Tanaka, Y., Tanoue, H. and Arai, K. (2003), Electrical activation of the ion-implanted phosphorus in 4H-SiC by excimer laser annealing, Journal of Applied Physics, Vol. 93, pp. 5934-5936.

Tian, Z., Quick, N. R., Kar, A. (2005), Effect of different laser sources and doping methods used to dope silicon carbide, Acta Materialia, Vol. 53, pp. 2835- 2844.

Tian, Z., Quick, N. R., Kar, A. (2004), Laser direct write and gas immersion laser doping fabrication of SiC diodes, Materials Research Society Symposium Proceedings, Vol. 815, pp. J3.4-J3.9.

Tin, C. C, Madangarli, V., Luckowski, E., Casady, J., Isaacs-Smith, T., Williams, J.R., Johnson, R.W., Gradinaru G. and Sudarshan, T. S. (1996), Semiconductor

Electronics, 1996. ICSE '96. Proceedings, 1996 IEEE International Conference on, pp. 55.

Tokarev, V. N. and Kaplan, A. F. (1999), An analytical modeling of time dependent pulsed laser melting, Journal of Applied Physics, Vol. 86, pp. 2836-2846.

Troffer, T., Schadt, M., Frank, T. Itoh, H., Pensel, G., Heindi, J., Strunk, H, P. and Maier, M. (1997), Doping of SiC by implantation of boron and aluminum. Physica Status Solidi A: Applied Research, Vol. 162, No.1, pp.277-298.

Usov, I. O., Suvorova, A. A., Sokolov, V. V., Kudryavtsev, Y. A. and Suvorov, A. V. (1999a), Transient enhanced diffusion of aluminum in SiC during high temperature ion implantation, Journal of Applied Physics, Vol 86, pp. 6039-6042.

Usov, I. O., Suvorova, A. A., Sokolov, V. V., Kudryavtsev, Y. A. and Suvorov, A. V. (1999b), Mechanism of enhanced diffusion of aluminum in 6H-SiC in the process of high-temperature ion implantation**,** Materials Research Society Symposium Proceeding 504, pp. 141-146.

Weiner, K. H., Carey, P. G., McCarthy A. M. and Sigmon, T. W. (1993), Microelectronic Engineering, Vol. 20, pp.107-130.

Yoshida, S., Sakuma, E., Okumura, H., Misawa, S. and Endo, K. (1987), Heteroepitaxial growth of SiC polytypes, Journal of Applied Physics, Vol. 62, pp. 303-305.

Zetterling, C. M. and östling, M. (2002), Advangtages of SiC, in Process Technology for Silicon Carbide Devices, edited by Carl-Mikael Zetterling, INSPEC, the Institution of Electrical Engineers, London, pp. 1-12.